

Electronic Thesis and Dissertation Repository

8-23-2013 12:00 AM

The Impact of Lateral Electron Disequilibrium on Stereotactic Body Radiation Therapy of Lung Cancer

Brandon Disher
The University of Western Ontario

Supervisor

Dr. Jerry J. Battista
The University of Western Ontario Joint Supervisor

Dr. Stewart Gaede
The University of Western Ontario

Graduate Program in Medical Biophysics

A thesis submitted in partial fulfillment of the requirements for the degree in Doctor of Philosophy

© Brandon Disher 2013

Follow this and additional works at: <https://ir.lib.uwo.ca/etd>

 Part of the [Medical Biophysics Commons](#), [Oncology Commons](#), [Other Physics Commons](#), and the [Radiology Commons](#)

Recommended Citation

Disher, Brandon, "The Impact of Lateral Electron Disequilibrium on Stereotactic Body Radiation Therapy of Lung Cancer" (2013). *Electronic Thesis and Dissertation Repository*. 1517.
<https://ir.lib.uwo.ca/etd/1517>

This Dissertation/Thesis is brought to you for free and open access by Scholarship@Western. It has been accepted for inclusion in Electronic Thesis and Dissertation Repository by an authorized administrator of Scholarship@Western. For more information, please contact wlsadmin@uwo.ca.

THE IMPACT OF LATERAL ELECTRON DISEQUILIBRIUM ON STEREOTACTIC
BODY RADIATION THERAPY OF LUNG CANCER

(Thesis format: Integrated Article)

by

Brandon Disher

Graduate Program in Medical Biophysics

A thesis submitted in partial fulfillment
of the requirements for the degree of
Doctor of Philosophy

The School of Graduate and Postdoctoral Studies
The University of Western Ontario
London, Ontario, Canada

© Brandon Disher 2013

Abstract

Stereotactic Body Radiation Therapy (SBRT) is an effective treatment option for patients with inoperable early-stage lung cancer. SBRT uses online image-guidance technology [e.g. cone-beam CT (CBCT)] to focus small-fields of high energy x-rays onto a tumour to deliver ablative levels of radiation dose (e.g. 54 Gy) in a few treatment fractions (e.g. 3). For the combination of these treatment parameters and a low density lung, lateral electron disequilibrium (LED) can potentially occur, reducing lung and tumour doses. The goal of this thesis was to determine the impact of LED on stereotactic body radiation therapy for lung cancer.

The effect of LED on lung dose distribution was studied using Monte Carlo simulations of a lung slab phantom. The magnitude of lung dose reduction due to LED, and the specific conditions (beam energy, field size, and lung density) that cause the phenomenon, were quantified and could be predicted using a relative depth dose factor (RDDF).

The RDDF concept was then used to develop a novel SBRT technique, called LED-optimized SBRT (LED-SBRT), which creates steep dose gradients, caused by intentional LED, to elevate tumour dose, while reducing/maintaining dose levels in healthy lung. Further, the RDDF aided in assessing the accuracy required in CBCT-derived lung density, when applied to adaptive SBRT dose calculations. In this regard, we determined that CBCT image artefacts produced erroneously low lung density, artificially triggering LED, and incorrectly predicting lower lung/tumour dose levels. As a result, CBCT number corrective techniques were developed in order to improve dose calculation accuracy.

The results of this thesis provide physicians and physicists with a much better prediction of the radiation dosimetry under disequilibrium conditions, and allow exploration of irradiation conditions that can cause LED. With this knowledge in-mind, competent decisions can be made regarding the choice of dose calculation algorithm, and aid in the design and interpretation of SBRT clinical trials. Furthermore, the outcomes of this work can help launch a new generation of SBRT techniques that exploit LED effects that may offer dosimetric benefits for selected patients.

Keywords

cone-beam CT (CBCT), image-guided radiation therapy (IGRT), CT numbers, dose computation, stereotactic body radiation therapy (SBRT), stereotactic ablative radiotherapy (SABR), intensity modulated radiation therapy (IMRT), lung cancer, lateral electron disequilibrium (LED), Monte Carlo (MC)

Co-Authorship

The following thesis contains material from manuscripts previously published in *Physics in Medicine and Biology*. The copyright(s) agreement from this journal is provided in Appendix A.

Chapter 2, "An in-depth Monte Carlo study of lateral electron disequilibrium for small fields in ultra-low density lung: implications for modern radiation therapy" was published in *Physics in Medicine and Biology*, 2012, March 21;57(6):1543-59 by Disher B, Hajdok G, Gaede S, Battista JJ. Drs. George Hajdok, Stewart Gaede, and Jerry Battista contributed to the design and interpretation of the experiments, results, and manuscript. I collected ion chamber readouts, set-up and ran Monte Carlo simulations, carried out main experiments, interpreted the results, and wrote the manuscript.

Chapter 3, "Forcing Lateral Electron Disequilibrium to Spare Lung Tissue: A novel technique for stereotactic body radiation therapy of lung cancer", was accepted pending revisions, *Physics in Medicine and Biology*, 2013, submitted April 16, by Disher B, Hajdok G, Gaede S, Mulligan M, and Battista JJ. Drs. George Hajdok, Stewart Gaede, and Jerry Battista contributed to the design and interpretation of the experiments, results, and manuscript. Mr. Mathew Mulligan and I, set-up and ran the Monte Carlo simulations. I also carried out main experiments, interpreted the results, and wrote the manuscript.

Chapter 4, "Correction for "artificial" electron disequilibrium due to cone-beam CT density errors: Implications for on-line adaptive stereotactic body radiation therapy of lung" was published in *Physics in Medicine and Biology*, 2013 Jun 21;58(12):4157-74 by Disher B, Hajdok G, Wang A, Craig J, Gaede S, and Battista JJ. Dr. George Hajdok, Dr. Stewart Gaede, Dr. Jerry Battista, and Mr. Jeff Craig contributed to the design and interpretation of the experiments, results, and manuscript. Dr. An (Kevin) Wang provided a registration algorithm used to warped images in this work. I carried out main experiments, interpreted the results, and wrote the manuscript.

Dedication

*To my mother Sandra, who taught me to work hard
and persevere through life's many challenges.*

Acknowledgments

Conducting research at the Ph.D. level can be an unpredictable and challenging venture. There may be times when you doubt your own work, and the course of your current path. In these moments of uncertainty, the quality of one's supervisor becomes apparent. To Drs. Jerry Battista, Stewart Gaede, and George Hajdok, I could always rely on you for expert advice, fair opinions, and many encouraging and kind words. I never felt alone in the pursuit of my Ph.D., and cannot thank you enough for your support. I can only hope to live up to the example you have set for me over the past six years.

I would also like to extend my gratitude to my advisory committee: Drs. Jeff Chen, David Holdsworth, David Palma, and (unofficially) Professor Jake Van Dyk and Dr. David Turnbull. Your objective opinions and positive approach to my research projects only improved the quality of my work. Further, my Ph.D. was greatly benefited through collaborative efforts with individuals at the LRCP (Matt Mulligan, Jeff Craig, Jeff Kempe, Carol Johnson, Dr. Steve Babic, Dr. Mike Oliver, Cory Gallagher, Ilma Xhaferllari, Timothy Yeung, Michael Jensen, and Anthony Lausch) and Robarts Imaging facility (Dr. Terry Peters, and Kevin Wang). I would also like to thank Barb Barons and Wendy Hough, administrative staff for the LRCP and MBP departments, you've always been welcoming and extremely helpful.

To my friends Sean Nestor, Chris d'Esterre, Pete Seslija, Shawn Kisch, Tumelo Moleko, Mich Beausoleil, Matt Sodomsky, Omar El-Sherif, Phil Medeiros, Grant Van Dyke, and Matt Sodomsky, you guys made the last six years a blast! Thank you for reminding me there's more to life than work.

Lastly, but certainly not least, I would like to thank my family: Mom, Dad, Helen, and Jessica. Your love and unwavering support has been, and always will be, the most important part of my life.

Table of Contents

Abstract.....	ii
Co-Authorship.....	iv
Dedication.....	v
Acknowledgments.....	vi
Table of Contents.....	vii
List of Tables.....	xii
List of Figures.....	xiii
List of Appendices.....	xvi
List of Abbreviations.....	xvii
Chapter 1.....	1
1 Introduction.....	1
1.1 A Clinical Case.....	1
1.2 Surgery <i>versus</i> Conventional Radiation Therapy.....	2
1.3 Stereotactic Body Radiation Therapy (SBRT).....	3
1.3.1 Development of SBRT.....	3
1.3.2 Improved imaging techniques facilitate SBRT in lung.....	4
1.3.3 CT image-guided SBRT.....	5
1.4 SBRT in Lung and Dose Escalation.....	8
1.5 Radiation Physics of Lung Dosimetry.....	9
1.5.1 KERMA, and KERMA _c	9
1.5.2 Charged Particle Interactions, Equilibrium, and Dose.....	10
1.5.3 Dose Calculation Algorithms.....	13
1.6 Research Problems, Questions, and Hypothesis.....	15
1.7 Research Plan and Objectives.....	16

1.8 Thesis Outline	18
1.8.1 A Monte Carlo study of the impacts of LED on Stereotactic Body Radiation Therapy (Chapter 2)	18
1.8.2 LED-SBRT: a novel SBRT technique used to spare lung tissue from radiation exposure (Chapter 3).....	19
1.8.3 Assessing the suitability of cone-beam CT thorax images for SBRT and dose adaptive radiation therapy (Chapter 4)	19
1.8.4 Conclusions (Chapter 5)	20
1.9 References	20
Chapter 2	29
2 An in-depth Monte Carlo study of lateral electron disequilibrium for small fields in ultra-low density lung: implications for modern radiation therapy	29
2.1 Introduction.....	29
2.2 Methods.....	33
2.2.1 Monte Carlo codes and parameters.....	33
2.2.2 Experimental validation of Monte Carlo simulation in low density material.....	33
2.2.3 Monte Carlo simulations of slab phantoms	36
2.3 Results.....	36
2.3.1 Monte Carlo simulations of slab phantoms; no tumour insert.....	36
2.3.2 Quantifying electron disequilibrium: relative depth-dose factors	41
2.3.3 Monte Carlo simulations of slab phantoms; with small tumour insert	44
2.4 Discussion	47
2.4.1 Dose calculations within lung tissue: quantifying electron disequilibrium	47
2.4.2 Effect of electron disequilibrium on lung tumour dose	48
2.4.3 Implications for SBRT clinical protocols and lung cancer patients with emphysema	49
2.4.4 Electron disequilibrium creates a hyper-sensitive density dependent dose distribution	50

2.5	Conclusions.....	51
2.6	Acknowledgements.....	51
2.7	Reference	51
Chapter 3.....		60
3	Forcing Lateral Electron Disequilibrium to Spare Lung Tissue: A novel technique for stereotactic body radiation therapy of lung cancer	60
3.1	Introduction.....	60
3.2	Methods.....	62
3.2.1	Monte Carlo codes and parameters.....	62
3.2.2	Cylindrical lung phantom simulations.....	63
3.2.3	Lung patient simulations.....	65
3.2.4	Lateral electron disequilibrium maps.....	67
3.3	Results.....	68
3.3.1	Cylindrical Lung Phantom Simulations.....	68
3.3.2	Lung patient simulations.....	72
3.3.3	Lateral electron disequilibrium maps.....	80
3.4	Discussion.....	84
3.4.1	LED-SBRT: potential benefits and controversy.....	84
3.4.2	LED-SBRT and tumour size.....	85
3.4.3	Dose calculation algorithms for use with LED-SBRT	86
3.4.4	Clinical implementation of LED-SBRT	87
3.5	Conclusion	88
3.6	Acknowledgements:.....	88
3.7	References:.....	88
Chapter 4.....		98
4	Correction for “artificial” electron disequilibrium due to cone-beam CT density errors: Implications for on-line adaptive stereotactic body radiation therapy of lung	98

4.1	Introduction.....	98
4.2	Materials and Methods.....	102
4.2.1	CT phantoms.....	102
4.2.2	CT scanners.....	103
4.2.3	Deformed CBCT (dCBCT) images	104
4.2.4	CT number corrective techniques	105
4.2.5	Dose calculations with treatment planning system (TPS)	108
4.3	Results.....	111
4.3.1	RANDO phantom and lung patient CT image data	111
4.3.2	Dose comparison using CBCT corrective techniques	114
4.4	Discussion.....	118
4.4.1	Disequilibrium maps.....	118
4.4.2	Recommendations.....	120
4.5	Conclusion	122
4.6	Acknowledgements.....	123
4.7	References.....	123
	Chapter 5.....	131
5	Conclusion and Future Work.....	131
5.1	Summary and Conclusions	131
5.1.1	Radiation parameters that cause lateral electron disequilibrium (LED). 131	
5.1.2	Development of a novel SBRT technique to exploit LED	132
5.1.3	Cone-beam CT image-based lung dose calculations	133
5.1.4	Conclusions.....	135
5.2	Future Work	136
5.2.1	Generalize the relative depth dose factor (RDDF) to other forms of modern radiation therapy	136

5.2.2	SBRT for lung cancer patients with emphysema.....	137
5.2.3	LED-optimized SBRT: clinical implementation	137
5.2.4	Cone-beam CT image-guided Adaptive SBRT	139
5.2.5	Assessing the prevalence of LED susceptibility in a population of lung cancer patients treated by SBRT.....	139
5.3	References.....	140
	Appendices.....	144
	Curriculum Vitae	146

List of Tables

Table 3-1 PTV dose metrics resulting from standard SBRT and LED-SBRT	73
Table 3-2 lung dose metrics resulting from standard SBRT and LED-SBRT	78
Table 4-1 A summary of abbreviations, image data sets, and RED conversion techniques referred to in Chapter 4 of the Thesis.	110

List of Figures

Figure 1-1 4-dimensional computed tomography (4D-CT) study of the sample patient.	1
Figure 1-2 dose distribution due to radiotherapy within a patient's thorax	2
Figure 1-3 3D-CT versus 4D-CT images of a lung cancer patient	5
Figure 1-4 Varian On-board Imaging cone-beam CT (CBCT) system	6
Figure 1-5 flow-chart describing image-guided adaptive radiation therapy (IGART).....	7
Figure 1-6 cone-beam CT (CBCT) image of the sample patient.....	8
Figure 1-7 transient charged particle equilibrium (TCPE) and lateral electron disequilibrium (LED) concepts	12
Figure 1-8 A schematic introducing the major topics to be addressed within this thesis.	17
Figure 2-1 Schematic diagrams of slab phantoms	34
Figure 2-2 Monte Carlo dose calculation versus A1SL ion chamber measurement.....	35
Figure 2-3 Monte Carlo calculated dose profiles for a slab phantom (no tumour).....	39
Figure 2-4 Monte Carlo calculated depth-dose profiles for a slab phantom (no tumour)	40
Figure 2-5 Relative depth dose factor iso-contour lines	43
Figure 2-6 95% electron equilibrium curves	44
Figure 2-7 Monte Carlo calculated depth-dose profiles for the lung slab phantom (3x3x3 cm ³ tumour).....	45
Figure 2-8 Monte Carlo calculated depth-dose profiles for the lung slab phantom (1x1x1 cm ³ tumour)	46

Figure 3-1 schematic diagram of the cylindrical phantom, and a transverse view of the lung patient.....	65
Figure 3-2 transverse view of the cylindrical phantom and relevant dose distributions	70
Figure 3-3 transverse view of the cylindrical phantom and relevant dose distributions.	72
Figure 3-4 transverse view of the lung patient and arc depth-dose profiles	74
Figure 3-5 coronal view of the lung patient and arc depth-dose profiles	76
Figure 3-6 dose volume histograms comparing arc dose for the planning target volume (PTV)	77
Figure 3-7 dose volume histograms comparing arc dose for the healthy lung volume	79
Figure 3-8 transverse view of the lung patient, comparing KERMA and DOSE.....	81
Figure 3-9 displays dose to KERMA ratios.....	83
Figure 4-1 the process of dose adaptive radiation therapy (DART).	100
Figure 4-2 relative depth dose factor (RDDF).....	107
Figure 4-3 CT number histograms acquired from the lung tissue within PCT and dCBCT image sets.....	107
Figure 4-4 planning CT (PCT) and cone-beam CT (CBCT) image of the RANDO phantom	111
Figure 4-5 planning CT (PCT) and deformed cone-beam CT (dCBCT) image of the lung patient.....	112
Figure 4-6 CT number profiles extracted from the PCT and CBCT images of the RANDO phantom.....	113
Figure 4-7 CT number profiles extracted from the PCT, LCT, dCBCT, and BCT images of the lung patient.....	114

Figure 4-8 PCT, dCBCT, BCT, or LCT VMAT dose distributions overlaid on the PCT image..... 116

Figure 4-9 dose volume histograms comparing calculated VMAT using either the PCT, LCT, dCBCT (RED_{PCT}), dCBCT (RED_{CBCT}), or BCT image-based plans..... 117

Figure 10 the Relative Depth Dose Factor (RDDF) maps acquired from the PCT, dCBCT, BCT, and LCT image sets..... 118

List of Appendices

Appendix A: Transfer of Copy write from Physics in Medicine and Biology	144
---	-----

List of Abbreviations

CT	computed tomography
4D-CT	4-dimensional computed tomography
3D-CT	3-dimensional computed tomography
TCP	tumour control probability
NSCLC	non-small cell lung cancer
3D-CRT	3-dimensional conventional radiation therapy
MLD	mean lung dose
V20	the percent volume of lung tissue receiving an absolute dose ≥ 20 Gy
V5	percent of the healthy lung volume receiving 5 Gy or more
CBCT	cone-beam CT
IGRT	image-guided radiation therapy
IGRT	image-guided adaptive radiation therapy
DART	dose adaptive radiation therapy
SBRT	stereotactic body radiation therapy
SABR	stereotactic ablative radiotherapy
SRS	stereotactic radiosurgery
LINAC	linear accelerator
LED	lateral electron disequilibrium
TERMA	total energy released per unit mass
KERMA	kinetic energy released <i>only</i> to charged particles per unit mass

KERMA _c	kinetic energy released to charged particles per unit mass and subsequently absorbed locally along charged particle tracks
CPE	charged particle equilibrium
TCPE	transient charged particle equilibrium
TPS	treatment planning system
MC	Monte Carlo
Co-60	Cobalt-60
RDDF	relative depth dose factor
LED-SBRT	LED-optimized SBRT
PCT	planning CT
MV	Megavoltage
IMRT	intensity-modulated radiation therapy
VMAT	volume modulated arc therapy
CCC	Collapsed Cone Convolution
AAA	Analytic Anisotropic Algorithm
RTOG	Radiation Therapy Oncology Group
GTV	gross tumour volume
IGTV	internal gross tumour volume
PTV	planning target volume
CPU	central processing unit
ECUT	electron cut-off energy

PCUT	photon cut-off energy
E	energy
FS	field size
PDD	percent depth dose
d_{\max} or D_{\max}	dose at maximum depth
RT	radiation therapy
DVH	dose volume histogram
LVH	lateral electron disequilibrium volume histogram
DIBH	deep inhale breath hold
HU-to-RED	HU-to-relative electron density conversion curve
RED_{PCT}	HU-to-RED conversion curve derived from PCT image
RED_{CBCT}	HU-to-RED conversion curve derived from CBCT image
DM_{PCT}	dose matrix calculated using PCT image data
DM_{CBCT}	dose matrix calculated using CBCT image data
OBI	on-board imaging
FOV	field-of-view
HF	half-fan
dCBCT	deformed CBCT image
LCT	LED-sensitive substitution image
BCT	Bulk CT image

ANIMAL	automated non-linear image matching and anatomical labeling
DIR	deformable image registration
MU	monitor unit
ESFS	equivalent square field size
D ₉₅ or D95	95% or more of the PTV receives at least 54 Gy of dose
LED-VMAT	LED-optimized VMAT
μ	linear attenuation coefficient
Z _{eff}	effective atomic number
ρ	density
Ψ	photon energy fluence
$\frac{S_{col}}{\rho}$	mass stopping power

Chapter 1

1 Introduction

1.1 A Clinical Case

Figure 1-1 depicts a CT scan of a middle-aged patient who presents with a small lung lesion (~ 1 cm in diameter) located within the middle lobe of the right lung. No evidence of mediastinal nodal or distant metastases is reported by the radiologist. This patient represents a typical lung cancer patient with stage T1 N0 M0 (early-stage tumour without nodal involvement or metastases). In Canada, this type of patient represents 1 of 25,600 individuals diagnosed with lung cancer in 2012 [1]. Treatment of lung cancer remains very challenging, where the mortality rate is approximately 40%, highest among all forms of cancers. Currently, patients such as the example reported in Figure 1-1 have two major options for treatment: (1) surgery or (2) radiation therapy. Each has its advantages and disadvantages in terms of tumour control and risk of treatment complications.

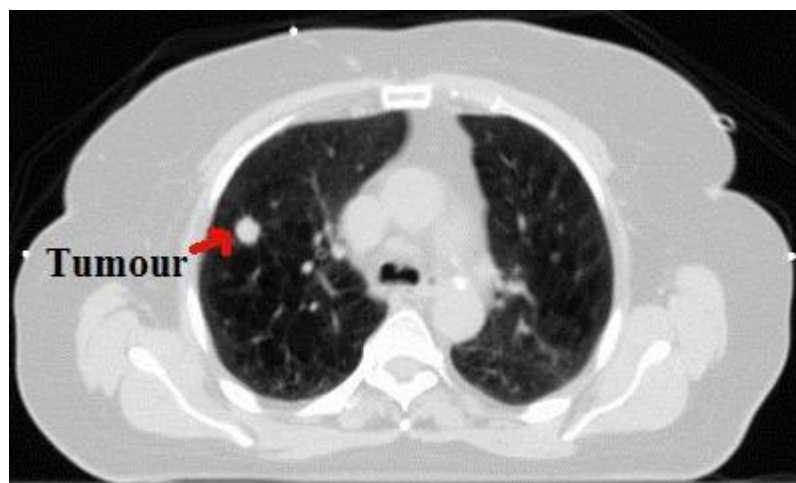


Figure 1-1 displays an axial slice from a 4-dimensional computed tomography (4D-CT) study of the sample patient. A small lung tumour is apparent in the right lung (left side of the image).

1.2 Surgery *versus* Conventional Radiation Therapy

Surgery is regarded as a very good option for patients presenting with early-staged lung cancer. In this case, the tumour is physically resected from the lung, resulting in excellent tumour control (tumour control probability (TCP) > 90% [2]). However, if the patient is a long-term cigarette smoker, and presents with other co-morbidities such as chronic obstructive pulmonary disease (e.g. emphysema and bronchitis), heart disease, frailty, and overall poor health, the patient may not be healthy enough to tolerate the invasive nature of open chest surgery [3]. In fact, only 10% of all lung cancer patients diagnosed with non-small cell lung cancer (NSCLC) are eligible for such surgery [4], despite the development of less invasive endoscopic procedures like video-assisted thorascopic surgery [5]. If the patient depicted above is unfit for surgery, 3-dimensional conventional radiation therapy (3D-CRT) is a potential treatment option.

3D-CRT involves multiple beams of x-ray radiation overlapped onto a tumour volume in order to deliver a high dose of radiation (e.g. 60 Gy), over many treatment sessions (e.g. 2 Gy per day x 30 days). See Figure 1-2 for example.

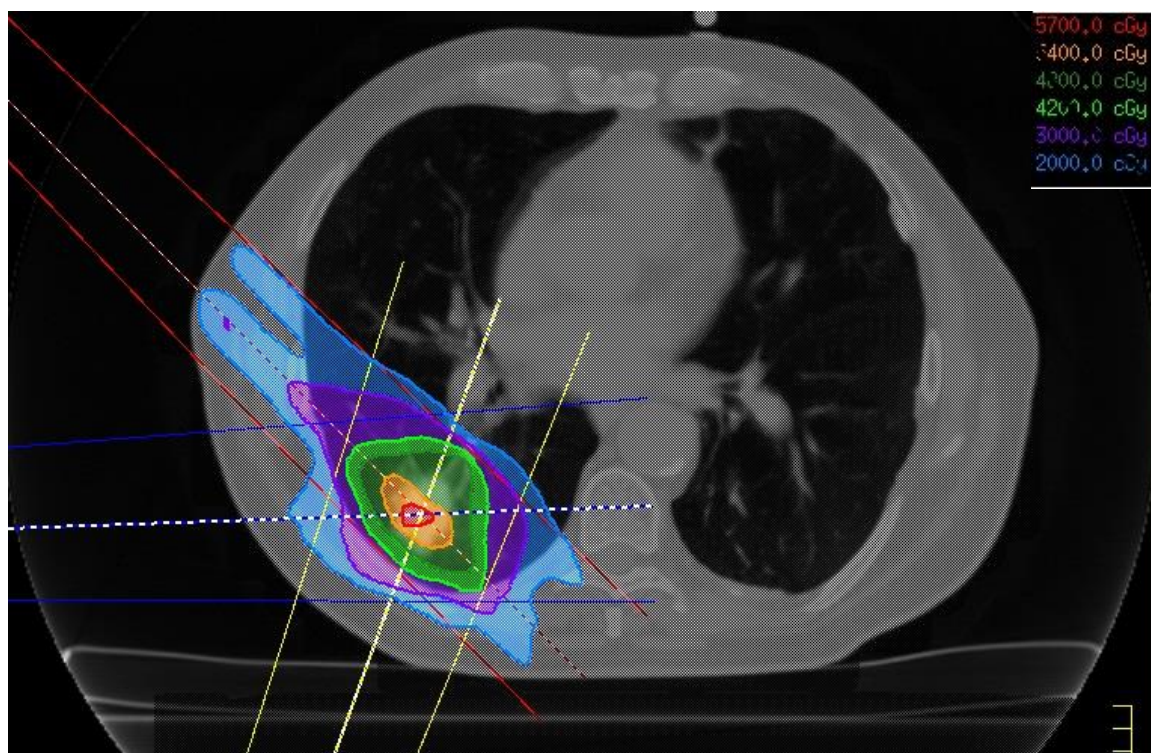


Figure 1-2: displays the additive dose from three overlapping fields of radiation focused onto a thoracic tumour. The coloured straight lines indicate the individual beams of radiation. The ‘colour wash’ (also shown with brighter iso-dose lines) indicates the dose distribution with drop-off outside the tumour region.

For patients with early-staged lung cancer who receive 3D-CRT, typical prescription doses range between 55-70 Gy extended over a 4 to 7 week period [6]. Unfortunately, this dosage schedule produces poor TCP levels of only 30% to 40% [7], and 5 year survival rates of only 20% [8]. Martel et. al. demonstrated that by escalating the tumour dose to 84.5 Gy (delivered in once-daily 2 Gy fractions) the TCP could be improved to 50% [9]. Other studies have attempted to escalate tumour dose in hopes of improving TCP, overall survival rates, and reducing local tumour recurrence rates [10, 11, 12]. However, endeavors to increase dose levels within the thorax must be weighed against the possibility of producing associated lung toxicity. In particular, the percent volume of lung tissue receiving an absolute dose ≥ 20 Gy (i.e. the V20), and the average absolute dose within healthy lung tissue [i.e. mean lung dose (MLD)] are of utmost importance for avoiding toxicity in lung radiotherapy [13, 14]. When these lung dose metrics are exceeded, complications such as radiation pneumonitis, fibrosis, and even death can occur [15]. Thus, in the absence of a highly effective treatment alternative, the sample patient shown in Fig. 1-1 may choose to forego treatment altogether; a decision that is associated with extremely poor prognosis [16]. As such, oncologists and medical physicists began to seek out better “high dose” radiation treatment alternatives for patients afflicted by early-staged lung cancer.

1.3 Stereotactic Body Radiation Therapy (SBRT)

1.3.1 Development of SBRT

Stereotactic radiosurgery (SRS) was developed during the time period spanning the 1940 - 1960s, and was solely used to treat cancerous malignancies of the central nervous system (e.g. brain) [17]. Radiosurgery is a non-invasive technique that uses single, high dose fractions of radiation (e.g. 24 Gy in one exposure) to ablate intracranial tumours. With SRS, high doses of radiation could be used to effectively control malignant disease while sparing surrounding healthy brain tissue [18]. However, great beam precision was required to target the tumour, which was facilitated through the use of auxiliary imaging modalities, fiducial markers, and a stereotactic frame to immobilize the skull [19] during

radiation exposure. Extracranial stereotactic radioablation techniques were later developed to treat cancerous sites in other regions of the body (e.g. abdomen) [20].

It appears that SRS could be adapted to treat patients with early-staged lung cancers who are not candidates for surgery. However, the translation of the SRS treatment technique from the brain to lung is not simple for two major reasons: 1) tumour mobility, and 2) more complex radiation dosimetry in low-density heterogeneous lung tissue. The process of human respiration causes the expansion and contraction of the thoracic cavity creating geometric as well as densitometric changes. Lung tumours can move centimeters in various directions, and these displacements may push the tumour beyond the field edges of the radiation beams. This is highly undesirable since portions of the tumour will be under irradiated, while surrounding lung tissue will be over irradiated. How then do we target a small, mobile tumour with a focused ablative dose of radiation? The answer to this question came through advancements in four-dimensional diagnostic computed tomography (4D-CT).

1.3.2 Improved imaging techniques facilitate SBRT in lung

A typical 3-dimensional CT (3D-CT) system can be used to create volumetric images of patient anatomy. However, 3D-CT may be insufficient to scan the human thorax due to artefacts caused by respiratory motion during the scan. The motion of the tumour and diaphragm can cause image artifacts within 3D-CT reconstructions that greatly complicate tumour volume definition as well as subsequent treatment delivery [21]. One way to overcome this challenge is to acquire a 4D-CT image of the lung patient's thorax [22, 23]. A 4D-CT is essentially a 3D movie that can be used to determine the *in vivo* trajectory of a lung tumour over the course of respiration (see Figure 1-3).

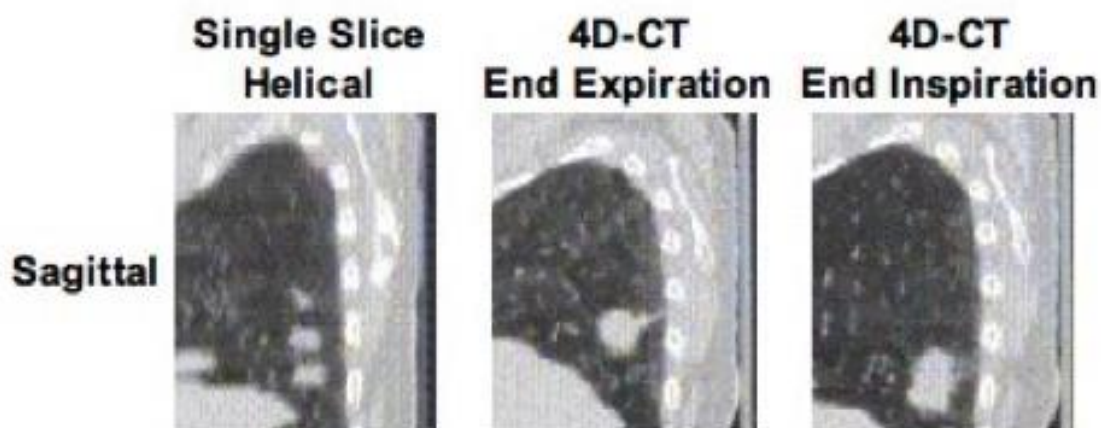


Figure 1-3: on the left, a single slice 3D-CT sagittal image of a lung cancer patient. Tumour motion produces an image artifact where three artificial small tumour volumes appear to be present in the lung. On the right, two 4D-CT images (sampled at maximum exhale and inhale) show there is actually one tumour volume moving along the superior-inferior axis of the lung.

With 4D-CT scanning, the entire patient breathing cycle is broken into a sequence of breathing phases; for each phase, a 3D-CT image is created that portrays the tumour and the thoracic cavity's position over a small time range. Using this information, it is conceivable to design a radiation treatment plan that accounts for lung tumour motion. However, additional imaging technology is required to align the radiation fields' isocentre with the tumour's center of mass at the time of treatment. This process can be performed accurately using image-guided radiation therapy (IGRT).

1.3.3 CT image-guided SBRT

IGRT combines the radiation treatment capabilities of a linear accelerator (LINAC) with some form of imaging modality into a single amalgamated design. Commonly, this is done in a radiotherapy setting by mounting a cone-beam CT (CBCT) scanner onto a LINAC (see Figure 1-4). With CBCT technology, a time-averaged CT volume of the patient's thorax can be acquired, which can be used to portray the tumour motion envelope, and patient anatomy just before delivering the next session of radiation treatment [24]. Further, 4D-CT and gating technology allow for the treatment planning

and delivery of radiation to occur during a single or multiple phases of patient respiration [25]. Currently, CBCT technology allows SRS treatment fields to be accurately focused onto a lung tumour (i.e. patient set-up), reducing misalignment between patient tissues and radiation beam to within 2 mm of static tissues [24].

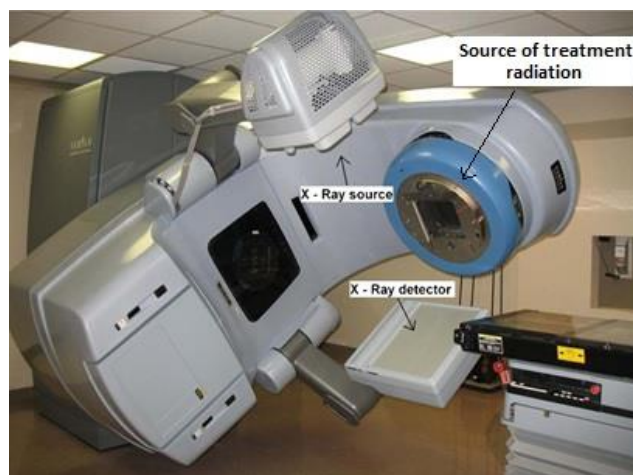


Figure 1-4 displays a Varian On-board Imaging cone-beam CT (CBCT) unit mounted onto a linear accelerator (LINAC). The auxiliary x-ray source and detector are used to form CBCT images. Adapted from Ding et al., 2007 [63]

In addition to facilitating patient set-up, IGRT hypothetically could be used to adapt radiation treatment planning and delivery in accordance with previous deformations within patient tissues, which otherwise cannot be resolved by simply re-aligning the patient or moving the treatment couch. This process of continually refining the delivered dose distribution in accordance with patient tissue deformation is called image-guided adaptive radiation therapy (IGART; see Figure 1-5 below). With IGART it is possible to adaptively modify the tumour target margins and dose distribution to best accommodate changes in patient anatomy. Also, any deviations in the accumulating delivered dose from intended dose can be accounted for by modifying treatment delivery in future fractions. However, adaptive modification of the dose distribution requires accurate dose calculation methods and high-fidelity tissue electron density information derived from image-guidance technology, which brings to question the suitability of cone-beam CT for on-line IGART.

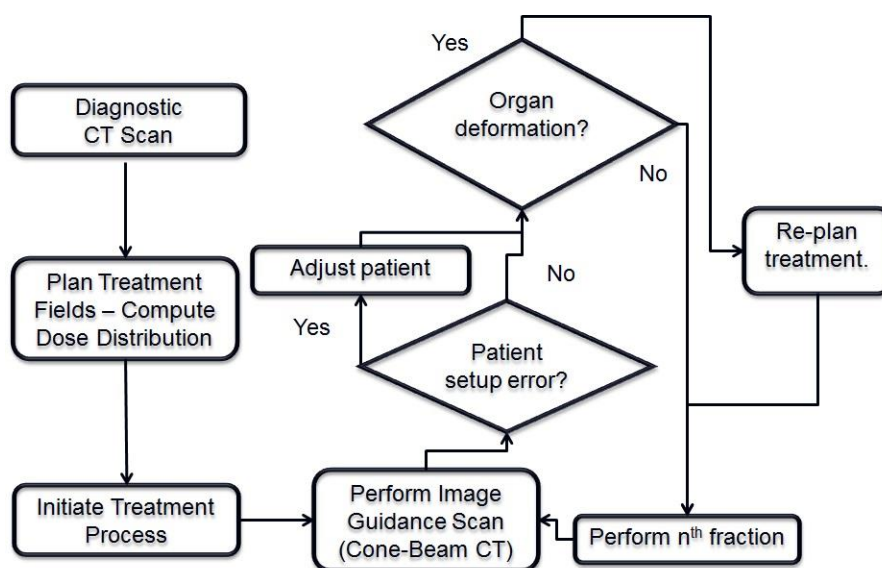


Figure 1-5: the future of image-guided radiation therapy is image-guided adaptive radiation therapy (IGART). In this paradigm, online CBCT information is used in a closed feedback loop to adaptively re-plan the radiation treatment fields in accordance with daily organ deformations and tumour changes. Patient set-up errors can also be avoided through couch shifts.

CBCT images are composed of voxels (or volume elements) that are assigned a specific CBCT number in accordance with tissue attenuation (in Hounsfield Units or HU). CBCT thorax images are subject to artifacts (or apparent flaws in CT numbers) such as cupping (dark artificially hypo-dense image regions) and streaking (lines of hyper/hypo-dense image regions), which are due to the broad-beam scanning geometry [26], and patient respiration during slow scan times (some of these artefacts can be seen in Figure 1-6, which shows the corresponding CBCT image of the patient displayed in Figure 1-1) [27, 28]. Thus, CBCT number data within patient lung tissue can be misleading, and electron density information derived from CBCT numbers used directly for dose calculations can be inaccurate. The extent to which these resultant density inaccuracies impact adaptive SBRT dose calculations is not known. This is a major topic of interest in this thesis.



Figure 1-6 displays the cone-beam CT (CBCT) image of the patient depicted in Fig. 1-1. Note the apparent cupping and streak artifacts, which are the visual results of inaccurate underlying CBCT number data.

1.4 SBRT in Lung and Dose Escalation

With advances in imaging and radiation treatment technologies, it became plausible to treat extracranial tumours using the SRS technique [29]. In particular, for target sites within the thorax, the radiotherapy community has coined a new term entitled stereotactic body radiation therapy (SBRT), or stereotactic ablative radiotherapy (SABR). SBRT has prompted a significant change in radiation therapy for early-staged lung cancer patients. Dose escalation is now possible with prescription radiation doses of 48-60 Gy delivered in only 3 to 8 fractions [this corresponds to biologically effective doses (BED) ≥ 100 Gy, which is ablative (i.e. comparable to surgical removal)]. Total treatment time can now be reduced to within a 2.5 week timeframe. This hypofractionated treatment paradigm has many postulated advantages: 1) short treatment times counter potential tumour cell repopulation, and 2) large doses per fraction may overcome ineffective tumour cell kill rates due to hypoxic (oxygen deficient) tumours, if re-oxygenation between fractions occurs [30]. Clinically, the advantages of SBRT are now evident in better outcomes for patients. Where dose is localized and sufficiently large, many trials have shown that TCP can be on the order of 90% with low levels of related toxicities [31, 32, 33, 34, 35].

With modern-day SBRT, there is an opportunity to further escalate the tumour dose in order to boost TCP beyond the 90% level. However, increased tumour dose must

not come at the expense of over-irradiating surrounding healthy lung tissue. Novel SBRT techniques should be developed in order to increase tumour dose levels, while at least maintaining the lung dose to currently well-tolerated levels. Unfortunately, one major road block impeding this development is a lack of knowledge concerning the complex radiation dosimetry of SBRT fields within heterogeneous lung tissue. SBRT of early-staged lung cancer uses high energy, small radiation fields to irradiate tumours embedded within low density lung. For these treatment conditions, a physical phenomenon called lateral electron disequilibrium (LED) may occur, which *reduces* the energy absorbed by lung and tumour tissues exposed to a small-field of radiation. This effect can also occur at the beam edge and media interfaces. To exacerbate this issue further, modern day treatment planning systems (TPS) may not adequately account for these unusual physical effects. These issues are better explained after briefly reviewing the radiation physics relevant to SBRT of early-staged lung cancer.

1.5 Radiation Physics of Lung Dosimetry

1.5.1 KERMA, and KERMA_c

This topic has been described in detail by The American Association of Physicists in Medicine (AAPM) Report Number 85 [36]. We begin with a distribution of photon *fluence* impinging on the surface of a patient. As photons traverse through the tissues of the body, their probability of attenuation (or interaction) per unit distance is given by the linear attenuation coefficient, μ ($\mu = [\text{cm}^{-1}]$). μ depends on the effective atomic number (Z_{eff}) and density ($\rho = [\text{g}/\text{cm}^3]$) of the tissue, as well as the incident photon energy (MeV).

In a radiotherapy beam, each photon has an associated energy (MeV), and the collection of photons reaching a point within a patient determines an energy fluence, Ψ (MeV/cm^2). Thus, at a particular location within the patient, the total energy released per unit mass (i.e. TERMA), is given as the product of the mass attenuation coefficient (μ/ρ) and the energy fluence at that point:

$$TERMA = \left(\frac{\mu}{\rho}\right) \Psi \quad (1.1)$$

The kinetic energy released *only* to charged particles (e.g. electrons) per unit mass is defined as KERMA (KERMA < TERMA). From KERMA we define another subset entity known as KERMA_c, or the collisional KERMA (KERMA_c < KERMA). KERMA_c is the kinetic energy released to charged particles per unit mass and subsequently absorbed locally along these charged particle tracks.

1.5.2 Charged Particle Interactions, Equilibrium, and Dose

1.5.2.1 Photon and Electron Interactions with Tissue

In the radiotherapeutic energy range (0.1 MeV – 18 MeV), there are three primary photon-tissue interactions that contribute to KERMA_c: the photoelectric effect, Compton interaction, and pair production. The predominance of each interaction depends on both the photon energy and absorber Z_{eff} . For instance, in water-like tissues ($Z_{\text{eff}} \sim 7.5$) the Compton interaction dominates over the energy range from 0.05 MeV to 10MeV.

The photon-tissue interactions impart kinetic energy to recoil charged particles, such as Compton electrons. Once launched, electrons experience Coulombic collisions along their path length, which converts kinetic energy into ionization and excitation events within the medium. The mass collisional stopping power, S_{col} , [37] can be used to describe the rate of local energy deposition by an electron along its path length:

$$\frac{S_{\text{col}}}{\rho} = \frac{d\bar{E}}{\rho dl}; \left(\frac{\text{MeV}\cdot\text{cm}^2}{\text{g}} \right) \quad (1.2)$$

Where an average rate of energy ($d\bar{E}$) is lost locally per unit path length (dl) and per density of medium (ρ). The range or path length, R , of an electron can be estimated from $\frac{S_{\text{col}}}{\rho}$ by integrating it over the slowed-down electron energies.

1.5.2.2 Charge Particle Equilibrium (CPE) and Lateral Electron Disequilibrium (LED)

The concept of charged particle equilibrium or CPE is central to this thesis. CPE occurs when the energy of electrons upon entering and leaving a small dosimetric volume are

equal [36]. Under CPE, partial electron tracks are complementary and can be summed to form a complete range (R). The situation is as if the energy actually deposited along a complete track is instead entirely absorbed ‘on the spot’. When CPE holds, the details concerning electron transport can be ignored in dose calculations, and the dose (D) becomes simply equal to the $KERMA_c$:

$$D = KERMA_c \quad (1.3)$$

Pure CPE can only occur when the photon and electron fluence is uniform across the sampling volume. In practice, these conditions are never met because of beam divergence and photon attenuation [38].

Transient charged particle equilibrium (TCPE) on the other hand is achievable, and the dose becomes proportional rather than equal to the collision KERMA. TCPE is a 3D concept, and can occur along the central-axis of a photon field if electron equilibrium is maintained in both the longitudinal and lateral directions (the longitudinal direction being parallel the central-axis of the radiation beam). For example, at shallow beam depths (below the maximum longitudinal electron range), longitudinal electron disequilibrium exists, which produces the characteristic ‘dose build-up’ region in depth dose profiles. Similarly, for depths beyond the maximum longitudinal electron range, lateral electron disequilibrium (LED) occurs when the lateral range of electrons becomes equal or greater than the radius of the field. Under this circumstance, electrons liberated from the radiation beam’s central-axis will scatter beyond the field edge, and they are not replaced, which reduces the dose along the beam’s central axis (see Figure 1-7). LED clearly depends on the radiation field size, beam energy, and medium density [39]. As a general rule, the lateral range of electrons is approximately 1/3 the longitudinal range in water. However, the lateral electron range can expand for higher beam energies incident upon lower density mediums (e.g. lung), as is the case for radiosurgery beams. With small fields incident on lung densities (0.1 g/cm^3 up to 0.4 g/cm^3 [40, 41]), we have the “perfect storm” for LED, and simplified dose calculation techniques are inadequate with regard to SBRT of early-staged lung cancer.

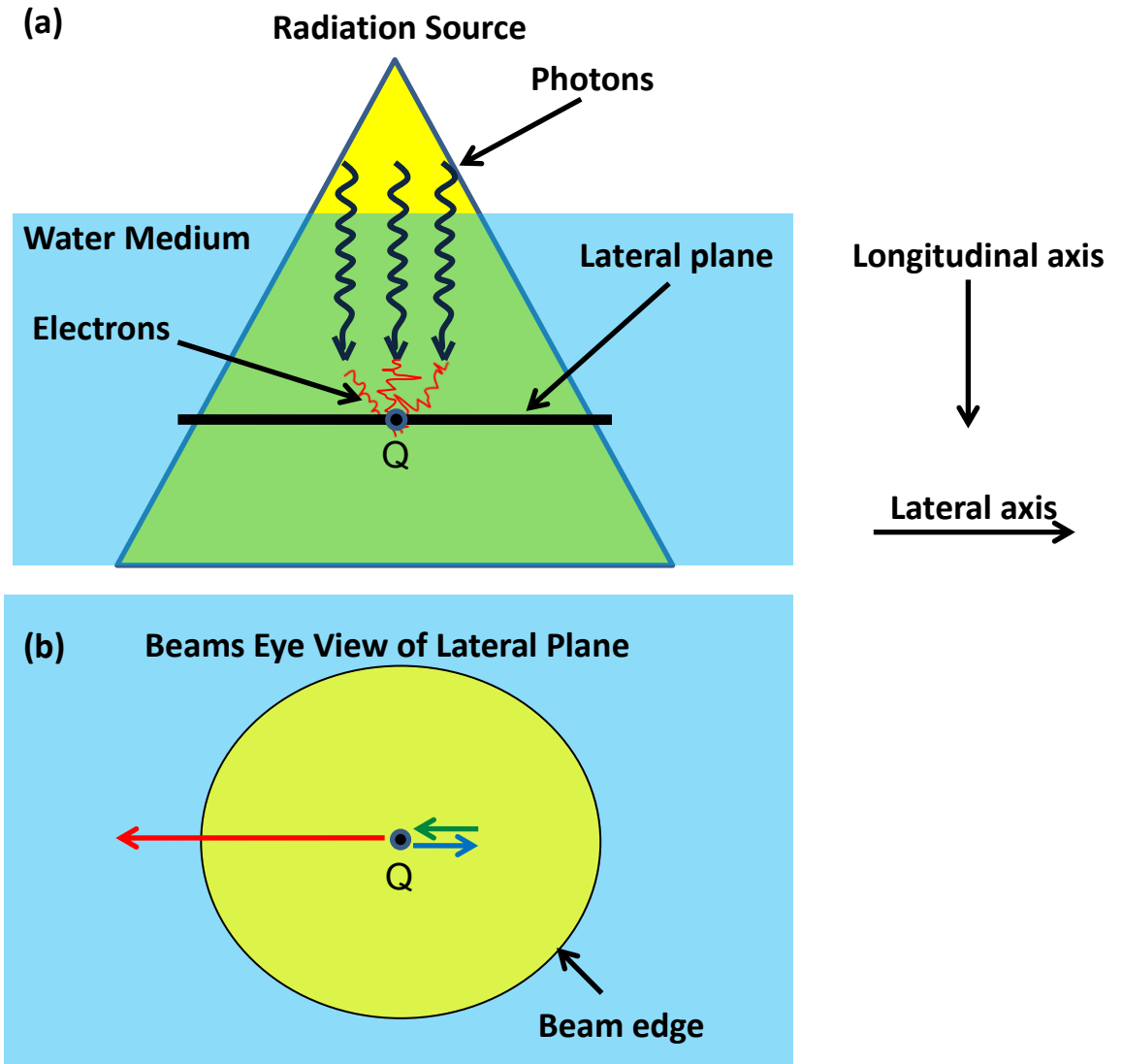


Figure 1-7 (a) depicts a photon source impinging on a water medium. Photons traverse through water until attenuated, where they liberate electrons. The electron trajectory is tortuous (shown as a curvy red line), but can eventually pass through point Q depositing dose there. Electron range can be viewed to have longitudinal and lateral components. The lateral component is observed in Fig. 1-7 (b), where a slice through the water is used to depict the LED concepts. For TCPE conditions, outwardly scattered electrons (blue arrow) are replaced by inwardly scattered electrons (green arrow), maintaining the energy equilibrium at Q. For LED conditions, outwardly scattered electrons (red arrow) travel beyond the field radius and cannot be replaced (as no photon fluence exists beyond the field edge), resulting in an energy imbalance, which reduces dose along the central-axis of the beam (at Q).

1.5.3 Dose Calculation Algorithms

Dose calculation algorithms can be classified in accordance with their ability to treat TERMA and electron scatter separately. Two general designations will be described below: 1) local energy deposition and 2) non-local energy deposition.

1.5.3.1 Local energy deposition algorithms

Dose calculation algorithms in this category intrinsically assume CPE, i.e., energy is absorbed ‘on the spot’, as opposed to along the entire electron range. As a result, these algorithms do not account for the dosimetric effects of LED, and can overestimate the lung/tumour dose distribution by as much as 30% for SBRT treatment conditions [42]. These techniques are generally no longer used in commercial software for treatment planning.

1.5.3.2 Non-local energy deposition algorithms

Models have been developed that focus on the transport of secondary electrons away from photon interaction sites. These typically involve convolution and/or superposition algorithms [43, 44, 45], or the Monte Carlo (MC) method [46, 47], which explicitly scores energy deposition along each electron track set in motion by numerous photon collisions. In the context of convolution or superposition algorithms, the initial sites of primary photon interaction are viewed as ‘sources’ of energy, and point kernels map the ‘spreading’ of energy away from the interaction site. For a radiotherapeutic photon beam, a downstream shower of secondary radiation (scattered photons and electrons) originates from every site of primary photon interaction within patient tissues and the convolution process sums their overall effect. In the presence of inhomogeneities, the attenuation of the primary photon fluence and the scope of dose kernel ‘spread’ are altered. For example, within lung tissue ($\rho \sim 0.25 \text{ g/cm}^3$), the local primary photon fluence is generally enhanced due to reduced tissue attenuation, but conversely the dose kernel expands in size due to extended particle ranges.

For SBRT treatment conditions in lung, where charged particle equilibrium is mildly disrupted (e.g. 6 MV beams), convolution algorithms can produce sufficiently accurate dose results within a range of 1-4% [48, 49, 50, 51, 52, 53]. However, for radiotherapeutic conditions involving more severe charged particle disequilibrium – high beam energies (18 MV), small field sizes ($< 5 \times 5 \text{cm}^2$), and low densities ($< 0.4 \text{g/cm}^3$) [51]– dose discrepancies as high as 8% have been reported [54]. More accurate calculations can then be obtained with the MC method.

Monte Carlo is a stochastic algorithm, which can be used to simulate the behavior of physical processes where analytical solutions fail and measurements are too difficult. The MC technique exploits well-known probability distributions that govern fundamental radiation interactions. For example, in order to simulate the transport of an x-ray through patient tissues, three sampling steps are required: 1) distance to interaction, 2) type of interaction (photoelectric, Compton, pair production), and 3) determination of the angular and energy distribution of secondary particles (scattered x-rays and electrons). Secondary particles are also followed through tissues until their energy is exhausted, or escapes the patient altogether. One possible combination of multiple events (stemming from steps 1-3) is called a ‘history’. For each history, the energy absorbed locally within patient tissues can be ‘scored’ within voxels. When a sufficient number of histories is simulated, MC generated dose distributions are extremely accurate. As such, MC results have been used to bench mark many different dose calculation techniques for circumstances involving charged particle disequilibrium [39, 49, 50, 51, 55, 56, 57, 58]. Unfortunately, the computational requirements of typical MC codes (e.g. DOSXYZnrc [National Research Council of Canada, Ottawa, ON]) are extensive, and calculation times have traditionally been too long for use in a clinical setting. However, recent innovations in computer processing power (e.g. graphics processing units) and parallel computation techniques have produced accurate MC dose calculations within seconds [59], and MC based TPSs are now becoming commercially available [e.g. Cyberknife stereotactic radiosurgery system (Accuray Inc., Sunnyvale, CA) [60]].

1.6 Research Problems, Questions, and Hypothesis

SBRT of early-staged lung cancer involves delivering ablative levels of radiation dose in only a few treatment sessions. With advancements in imaging and radiation treatment technologies, there is an opportunity to develop novel SBRT techniques to further increase lung tumour dose levels, which may improve tumour control and overall survival rates. Unfortunately, SBRT treatment conditions in lung (MV x-rays, small fields, and low density) are more apt to disrupt CPE, which perturbs the delivered dose distribution in the tumour and lung tissues. Modern day CBCT densitometry and dose calculation algorithms do not address extreme LED conditions appropriately. Previous authors focused on the inability of dose calculation algorithms to predict the dosimetric effects of LED, but failed to explore the full range of radiotherapeutic (RT) conditions [50, 51, 52, 53, 54, 55, 56, 58, 48]. A study on this topic may help to elucidate these RT conditions, which is useful for clinicians looking to avoid LED or select appropriate dose calculation algorithms for SBRT clinical trials. In addition, this information would be useful in the development of novel SBRT techniques that can exploit correctly-predicted LED, focused on increasing tumour dose, while at least maintaining and/or reducing normal lung dose to safe levels. In order to address these issues, we have therefore formulated the following research questions:

1. What combination of radiation field size, energy, and lung density will cause the LED phenomenon to occur?
2. How sensitive is the dose distribution in LED regions to CT-derived lung density?
3. How do we design a new SBRT technique that forces LED to occur in order to produce “spikes” of highly localized dose in small tumours, relative to surrounding lung?

In addition to the issues described above, the implementation of adaptive SBRT currently faces many practical challenges. Online image-guidance technology (e.g. cone-beam CT) undoubtedly allows for accurate alignment of the radiation treatment fields with the tumour’s location. Furthermore, CBCT images could also be used for online dose calculations in order to adapt radiation treatment parameters in accordance with observed

organ deformations. However, today's CBCT images of the thorax contain erroneous CT number information, which contribute to dosimetric errors in the adaptive SBRT process [61, 62]. However, no explanation has been provided to date that expands on relevant physics behind these density-driven errors, or their magnitude. These research problems lead to the next set of questions for the thesis:

4. How does CBCT-derived lung density affect the lung and tumour dose distribution?
5. Are lung cone-beam CT numbers correctable for the purpose of accurate dose calculation?

The answers to these questions are highly inter-related, and depend upon core consideration of the LED phenomenon. The thesis **hypothesis** is thus stated as follows:

The accurate delivery of image-guided adaptive stereotactic body radiation therapy for lung cancer requires due consideration of the potential effects of charged particle disequilibrium (CPE and LED).

1.7 Research Plan and Objectives

The work presented in this thesis is focused on three main topics and their interdependency: 1) stereotactic body radiation therapy (SBRT) of early-staged lung cancer, 2) the radiation physics of photon energy deposition within lung tissue [specifically, concepts involving charged particle equilibrium (CPE) and lateral electron disequilibrium (LED)], and finally, 3) image-guided radiation therapy (IGRT) using online cone-beam CT (CBCT) for adaptive SBRT of lung cancer. These topics are displayed in Figure **1-8** with regions labeled by the letters **A** (SBRT and physics in lung; coloured red), **B** (SBRT and IGRT; coloured blue), **C** (physics and IGRT; coloured green), and **D** (union of all three topics; coloured purple). Three primary research objectives were developed in order to study these main topics and their co-dependency:

1. Using a Monte Carlo simulation of a lung slab phantom, determine the combination of radiation beam energy, field size, and lung density that causes a sudden drop in lung dose, indicating loss of CPE (**region A in Figure 1-8**).
2. To develop a new SBRT technique, denoted as LED-optimized SBRT, which utilizes radiation therapy parameters designed specifically to cause LED in order to greatly reduce normal lung dose, while increasing dose levels within the tumour volume (**region A in Figure 1-8**).
3. To assess the magnitude of densitometric errors in CBCT images of the thorax due to CBCT geometry, slow scan times, and patient respiratory motion [region **B** in Figure 1-8].
4. To determine the extent of dosimetric error due to erroneous CBCT number data for adaptive SBRT of early-staged lung cancer (**region C in Figure 1-8**).

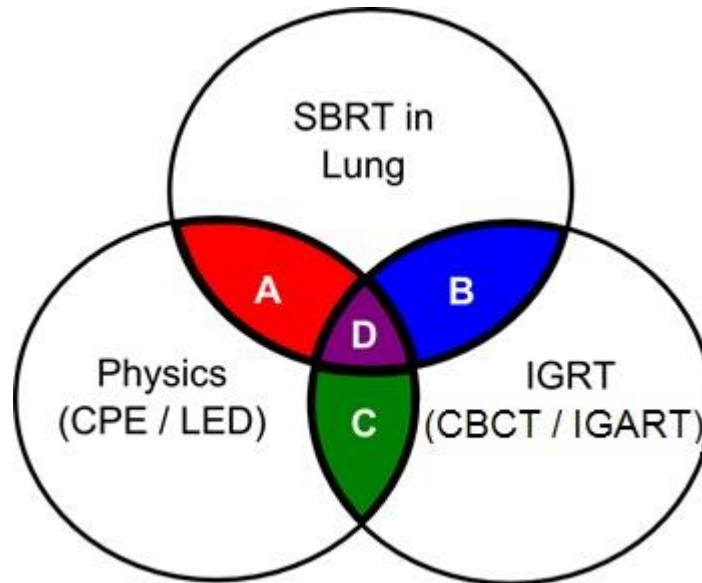


Figure 1-8 A schematic introducing the major topics to be addressed within this thesis. Correlations between these topics are demarked by the letter A ($SBRT \cup Physics$; red region), B ($SBRT \cup IGRT$; blue region), C ($Physics \cup IGRT$; green region), and D ($SBRT \cup Physics \cup IGRT$; purple region).

1.8 Thesis Outline

1.8.1 A Monte Carlo study of the impacts of LED on Stereotactic Body Radiation Therapy (Chapter 2)

This chapter is adapted from the research article, "An in-depth Monte Carlo study of lateral electron disequilibrium for small fields in ultra-low density lung: implications for modern radiation therapy" published in *Physics in Medicine and Biology*, 2012, March 21;57(6):1543-59 by Disher B, Hajdok G, Gaede S, Battista JJ. This chapter uses Monte Carlo simulations of multiple virtual lung phantoms to determine the radiotherapeutic parameters necessary to disrupt CPE, creating LED (**Region A; see Figure 1-8**). Over 1000 dose calculations were performed by varying different combinations of beam energy (Co-60 up to 18 MV), field size ($1 \times 1 \text{ cm}^2$ up to $15 \times 15 \text{ cm}^2$), and lung density (0.001 g/cm^3 up to 1 g/cm^3). From this analysis, a new clinical tool was developed as a predictor of LED, referred to as the Relative Depth Dose Factor (RDDF). The RDDF can be used to indicate the extent of LED ($\text{RDDF} < 1$) or electronic equilibrium ($\text{RDDF} \geq 1$). For example, when $\text{RDDF} < 0.7$, LED was severe and caused reductions of both the lung and tumour dose distribution. In general, dose reductions were the worst when small tumours were irradiated with high beam energies, small field sizes, and low lung density (as is the case for SBRT of early-staged lung cancer). This study contains new knowledge that is useful for radiation oncologists who wish to avoid the negative dosimetric effects of LED, which is crucial for the design and interpretation of SBRT clinical trials. Further, chapter 2 explains the physical effects of lung density on radiotherapy dose calculations. This information is valuable for interpreting how erroneous CBCT-derived lung density influences adaptive SBRT dose calculations (Chapter 4). Also, this data aided in the development of new a SBRT technique that uses LED to advantage (Chapter 3).

1.8.2 LED-SBRT: a novel SBRT technique used to spare lung tissue from radiation exposure (Chapter 3)

This chapter is adapted from the research article, "Forcing Lateral Electron Disequilibrium to Spare Lung Tissue: A novel technique for stereotactic body radiation therapy of lung cancer", accepted pending revisions, *Physics in Medicine and Biology*, 2013, submitted April 16, by Disher B, Hajdok G, Gaede S, Mulligan M, and Battista JJ. In this chapter, Monte Carlo simulations of both a phantom and lung patient are used to demonstrate a new SBRT technique, LED-optimized SBRT (LED-SBRT), which utilizes tailored radiation therapy parameters (determined from Chapter 2) to cause LED to advantage (**Region A; see Figure 1-8**). LED-SBRT creates extremely steep dose gradients at the lung/tumour boundary. This highly heterogeneous dose distribution can be used to reduce normal lung dose, while increasing dose levels within a tumour volume. For example, LED-SBRT was used to increase the patient's maximal, mean, and minimal tumour dose by as much as 80Gy, 11Gy, and 3Gy, when compared to a more conventional SBRT plan. Despite elevated tumour dose levels, LED-SBRT was also able to provide sufficient tumour dose coverage, while maintaining or lowering commonly used lung dose metrics (e.g. mean lung dose, V5, and V20). These results are important as increased tumour dose may improve tumour control probability, while lower lung dose metrics may reduce the chances of radiation lung injury (e.g. pneumonitis and fibrosis).

1.8.3 Assessing the suitability of cone-beam CT thorax images for SBRT and dose adaptive radiation therapy (Chapter 4)

This chapter is adapted from the research article, "Correction for "artificial" electron disequilibrium due to cone-beam CT density errors: Implications for on-line adaptive stereotactic body radiation therapy of lung" published in *Physics in Medicine and Biology*, 2013 Jun 21;58(12):4157-74 by Disher B, Hajdok G, Wang A, Craig J, Gaede S, and Battista JJ. In this chapter, we assess the suitability of CBCT thorax images for SBRT of three typical early-staged lung cancer patients (**region B; see Figure 1-8**). The accuracy of CBCT number data, and resultant dose distributions, were compared to

planning CT (PCT) based information. For example, it was determined that CBCT lung image artifacts (cupping, streaking, and blurring) erroneously reduced CBCT derived lung density compared to PCT data. The dosimetric effect of erroneously low CBCT lung density was to *artificially* create LED, which incorrectly reduced the lung and tumour dose compared to PCT results (**region C**; see **Figure 1-8**). These findings were interpreted by applying the RDDF, and knowledge of LED physics derived from Chapter 2. Further, using this knowledge, we proposed appropriate CT number corrective techniques to improve CBCT image-based dose calculation accuracy for dose adaptive SBRT of early-staged lung cancer patients (**region D**; see **Figure 1-8**).

1.8.4 Conclusions (Chapter 5)

In the last chapter, the main findings from chapters 2-4 are summarized. Also, a separate section is dedicated to potential future projects that could stem from this thesis.

1.9 References

- [1] "Canadian Cancer Society's Steering Committee: Canadian Cancer Statistics 2012," Canadian Cancer Society, Toronto.
- [2] N. Nguyen, L. Garland, J. Welsh, R. Hamilton, D. Cohen and V. Vinh-Hung, "Can stereotactic fractionated radiation therapy become the standard of care for early stage non-small cell lung carcinoma.," *Cancer Treat Rev*, vol. 34, no. 8, pp. 719-727--, Dec 2008.
- [3] R. Timmerman, R. Paulus, J. Galvin, J. Michalski, W. Straube, J. Bradley, A. Fakiris, A. Bezjak, G. Videtic, D. Johnstone, J. Fowler, E. Gore and H. Choy, "Stereotactic body radiation therapy for inoperable early stage lung cancer.," *JAMA*, vol. 303, no. 11, pp. 1070-1076, Mar 2010.
- [4] S. Falk and W. C, Lung Cancer Third Edition, Oxford University Press, 2010.

- [5] C. F. Mountain and K. E. Hermes, "Surgical treatment of lung cancer. Past and present.," *Methods Mol Med*, vol. 75, pp. 453-487, 2003.
- [6] N. P. Rowell and C. J. Williams, "Radical radiotherapy for stage I/II non-small cell lung cancer in patients not sufficiently fit for or declining surgery (medically inoperable): a systematic review.," *Thorax*, vol. 56, no. 8, pp. 628-638, Aug 2001.
- [7] R. Timmerman and L. Xing, *Image-Guided and Adaptive Radiation Therapy*, Philadelphia: Lippincott Williams & Wilkins, 2010.
- [8] J. P. Wisnivesky, M. Bonomi, C. Henschke, M. Iannuzzi and T. McGinn, "Radiation therapy for the treatment of unresected stage I-II non-small cell lung cancer.," *Chest*, vol. 128, no. 3, pp. 1461-1467, Sep 2005.
- [9] M. K. Martel, R. K. Ten Haken, M. B. Hazuka, M. L. Kessler, M. Strawderman, A. T. Turrisi, T. S. Lawrence, B. A. Fraass and A. S. Lichter, "Estimation of tumor control probability model parameters from 3-D dose distributions of non-small cell lung cancer patients.," *Lung Cancer*, vol. 24, no. 1, pp. 31-37, Apr 1999.
- [10] J. A. Hayman, M. K. Martel, R. K. Ten Haken, D. P. Normolle, S. R. Todd, J. F. Littles, M. A. Sullivan, P. W. Possert, A. T. Turrisi and A. S. Lichter, "Dose escalation in non-small-cell lung cancer using three-dimensional conformal radiation therapy: update of a phase I trial.," *J Clin Oncol*, vol. 19, no. 1, pp. 127-136, Jan 2001.
- [11] X. Qiao, O. Tullgren, I. Lax, F. Sirzén and R. Lewensohn, "The role of radiotherapy in treatment of stage I non-small cell lung cancer.," *Lung Cancer*, vol. 41, no. 1, pp. 1-11, Jul 2003.
- [12] N. Ohri, M. Werner-Wasik, I. Grills, J. Belderbos, A. Hope, D. Yan, L. Kestin, M. Guckenberger, J. Sonke, J. Bissonnette and others, "Modeling Local Control After Hypofractionated Stereotactic Body Radiation Therapy for Stage I Non-Small Cell

- Lung Cancer: A Report From the Elekta Collaborative Lung Research Group," *International Journal of Radiation Oncology* Biology* Physics*, vol. 84, no. 3, pp. e379--e384, 2012.
- [13] R. B. Barriger, J. A. Forquer, J. G. Brabham, D. L. Andolino, R. H. Shapiro, M. A. Henderson, P. A. S. Johnstone and A. J. Fakiris, "A dose-volume analysis of radiation pneumonitis in non-small cell lung cancer patients treated with stereotactic body radiation therapy.," *Int J Radiat Oncol Biol Phys*, vol. 82, no. 1, pp. 457-462, Jan 2012.
- [14] U. Ricardi, A. R. Filippi, A. Guarneri, F. R. Giglioli, C. Mantovani, C. Fiandra, S. Anglesio and R. Ragona, "Dosimetric predictors of radiation-induced lung injury in stereotactic body radiation therapy.," *Acta Oncol*, vol. 48, no. 4, pp. 571-577, 2009.
- [15] J. Bradley, M. V. Graham, K. Winter, J. A. Purdy, R. Komaki, W. H. Roa, J. K. Ryu, W. Bosch and B. Emami, "Toxicity and outcome results of RTOG 9311: a phase I-II dose-escalation study using three-dimensional conformal radiotherapy in patients with inoperable non-small-cell lung carcinoma.," *Int J Radiat Oncol Biol Phys*, vol. 61, no. 2, pp. 318-328, Feb 2005.
- [16] F. C. Detterbeck and C. J. Gibson, "Turning gray: the natural history of lung cancer over time.," *J Thorac Oncol*, vol. 3, no. 7, pp. 781-792, Jul 2008.
- [17] L. L., "The stereotactic method and radiosurgery of the brain," *Acta Chir Scand*, vol. 102, pp. 316-319, 1951.
- [18] A. Sahgal, L. Ma, E. Chang, A. Shiu, D. A. Larson, N. Laperriere, F.-F. Yin, M. Tsao, C. Menard, P. S. Basran, D. Létourneau, M. Heydarian, D. Beachey, V. Shukla, M. Cusimano, M. Hodaie, G. Zadeh, M. Bernstein and M. Schwartz, "Advances in technology for intracranial stereotactic radiosurgery.," *Technol Cancer Res Treat*, vol. 8, no. 4, pp. 271-280, Aug 2009.
- [19] P. Iyengar and R. D. Timmerman, "Stereotactic ablative radiotherapy for non-small

- cell lung cancer: rationale and outcomes.," *J Natl Compr Canc Netw*, vol. 10, no. 12, pp. 1514-1520, Dec 2012.
- [20] H. Blomgren, I. Lax, I. Näslund and R. Svanström, "Stereotactic high dose fraction radiation therapy of extracranial tumors using an accelerator. Clinical experience of the first thirty-one patients.," *Acta Oncol*, vol. 34, no. 6, pp. 861-870, 1995.
- [21] H. Pass, *Principles and Practice of Lung Cancer*, Lippincott Williams & Williams, 2010.
- [22] P. J. Keall, G. Starkschall, H. Shukla, K. M. Forster, V. Ortiz, C. W. Stevens, S. S. Vedam, R. George, T. Guerrero and R. Mohan, "Acquiring 4D thoracic CT scans using a multislice helical method.," *Phys Med Biol*, vol. 49, no. 10, pp. 2053-2067, May 2004.
- [23] S. S. Vedam, P. J. Keall, V. R. Kini, H. Mostafavi, H. P. Shukla and R. Mohan, "Acquiring a four-dimensional computed tomography dataset using an external respiratory signal.," *Phys Med Biol*, vol. 48, no. 1, pp. 45-62, Jan 2003.
- [24] J.P. Bissonnette, T. G. Purdie, J. A. Higgins, W. Li and A. Bezjak, "Cone-beam computed tomographic image guidance for lung cancer radiation therapy.," *Int J Radiat Oncol Biol Phys*, vol. 73, no. 3, pp. 927-934, Mar 2009.
- [25] H. Wu, Q. Zhao, R. I. Berbeco, S. Nishioka, H. Shirato and S. B. Jiang, "Gating based on internal/external signals with dynamic correlation updates.," *Phys Med Biol*, vol. 53, no. 24, pp. 7137-7150, Dec 2008.
- [26] J. H. Siewerdsen and D. A. Jaffray, "Cone-beam computed tomography with a flat-panel imager: magnitude and effects of x-ray scatter.," *Med Phys*, vol. 28, no. 2, pp. 220-231, Feb 2001.
- [27] S. Leng, J. Zambelli, R. Tolakanahalli, B. Nett, P. Munro, J. Star-Lack, B. Paliwal and G.-H. Chen, "Streaking artifacts reduction in four-dimensional cone-beam

- computed tomography.," *Med Phys*, vol. 35, no. 10, pp. 4649-4659, Oct 2008.
- [28] T. Li, E. Schreibmann, Y. Yang and L. Xing, "Motion correction for improved target localization with on-board cone-beam computed tomography.," *Phys Med Biol*, vol. 51, no. 2, pp. 253-267, Jan 2006.
- [29] C. J. A. Haasbeek, B. J. Slotman and S. Senan, "Radiotherapy for lung cancer: clinical impact of recent technical advances.," *Lung Cancer*, vol. 64, no. 1, pp. 1-8, Apr 2009.
- [30] A. Chi, W. A. Tomé, J. Fowler, R. Komaki, N. P. Nguyen, M. P. Mehta and J. S. Welsh, "Stereotactic body radiation therapy in non-small-cell lung cancer: linking radiobiological modeling and clinical outcome.," *Am J Clin Oncol*, vol. 34, no. 4, pp. 432-441, Aug 2011.
- [31] J. D. Bradley, I. El Naqa, R. E. Drzymala, M. Trovo, G. Jones and M. D. Denning, "Stereotactic body radiation therapy for early-stage non-small-cell lung cancer: the pattern of failure is distant.," *Int J Radiat Oncol Biol Phys*, vol. 77, no. 4, pp. 1146-1150, Jul 2010.
- [32] I. S. Grills, V. S. Mangona, R. Welsh, G. Chmielewski, E. McInerney, S. Martin, J. Wloch, H. Ye and L. L. Kestin, "Outcomes after stereotactic lung radiotherapy or wedge resection for stage I non-small-cell lung cancer.," *J Clin Oncol*, vol. 28, no. 6, pp. 928-935, Feb 2010.
- [33] F. J. Lagerwaard, C. J. A. Haasbeek, E. F. Smit, B. J. Slotman and S. Senan, "Outcomes of risk-adapted fractionated stereotactic radiotherapy for stage I non-small-cell lung cancer.," *Int J Radiat Oncol Biol Phys*, vol. 70, no. 3, pp. 685-692, Mar 2008.
- [34] H. Onishi, H. Shirato, Y. Nagata, M. Hiraoka, M. Fujino, K. Gomi, Y. Niibe, K. Karasawa, K. Hayakawa, Y. Takai, T. Kimura, A. Takeda, A. Ouchi, M. Hareyama, M. Kokubo, R. Hara, J. Itami, K. Yamada and T. Araki, "Hypofractionated

- stereotactic radiotherapy (HypoFXSRT) for stage I non-small cell lung cancer: updated results of 257 patients in a Japanese multi-institutional study.," *J Thorac Oncol*, vol. 2, no. 7 Suppl 3, pp. S94--100, Jul 2007.
- [35] F. O. B. Spoelstra and S. Senan, "Novel tools in radiotherapy.," *Ann Oncol*, vol. 19 Suppl 7, pp. vii294--vii299, Sep 2008.
- [36] N. Papanikolaou, et al., Tissue inhomogeneity corrections for megavoltage photon beams AAPM Report No 85. *Madison, WI: Medical Physics Publishing*, 2004.
- [37] H. E. Johns and J. R. Cunningham, *The Physics of Radiology*, Springfield, IL: C.C. Thomas, 1983.
- [38] K. R. Kase, B. Björngard and F. Attix, *The Dosimetry of Ionizing Radiation*, San Diego: Academic Press Inc., 1985.
- [39] T. R. Mackie, E. el Khatib, J. Battista, J. Scrimger, J. Van Dyk and J. R. Cunningham, "Lung dose corrections for 6- and 15-MV x rays.," *Med Phys*, vol. 12, no. 3, pp. 327-332, 1985.
- [40] L. J. Rosenblum, R. A. Mauceri, D. E. Wellenstein, F. D. Thomas, D. A. Bassano, B. N. Raasch, C. C. Chamberlain and E. R. Heitzman, "Density patterns in the normal lung as determined by computed tomography.," *Radiology*, vol. 137, no. 2, pp. 409-416, Nov 1980.
- [41] J. van Dyk, T. J. Keane and W. D. Rider, "Lung density as measured by computerized tomography: implications for radiotherapy.," *Int J Radiat Oncol Biol Phys*, vol. 8, no. 8, pp. 1363-1372, Aug 1982.
- [42] D. Schuring and C. W. Hurkmans, "Developing and evaluating stereotactic lung RT trials: what we should know about the influence of inhomogeneity corrections on dose.," *Radiat Oncol*, vol. 3, p. 21, 2008.

- [43] N. Papanikolaou, T. R. Mackie, C. Meger-Wells, M. Gehring and P. Reckwerdt, "Investigation of the convolution method for polyenergetic spectra.," *Med Phys*, vol. 20, no. 5, pp. 1327-1336, 1993.
- [44] M. M. Aspradakis and A. T. Redpath, "A technique for the fast calculation of three-dimensional photon dose distributions using the superposition model.," *Phys Med Biol*, vol. 42, no. 8, pp. 1475-1489, Aug 1997.
- [45] A. Mack, D. Weltz, S. G. Scheib, B. Wowra, H. Böttcher and V. Seifert, "Development of a 3-D convolution/superposition algorithm for precise dose calculation in the skull.," *Australas Phys Eng Sci Med*, vol. 29, no. 1, pp. 1-12, Mar 2006.
- [46] P. Andreo, "Monte Carlo techniques in medical radiation physics.," *Phys Med Biol*, vol. 36, no. 7, pp. 861-920, Jul 1991.
- [47] F. Verhaegen and J. Seuntjens, "Monte Carlo modelling of external radiotherapy photon beams.," *Phys Med Biol*, vol. 48, no. 21, pp. R107--R164, Nov 2003.
- [48] P. Carrasco, N. Jornet, M. A. Duch, L. Weber, M. Ginjaume, T. Eudaldo, D. Jurado, A. Ruiz and M. Ribas, "Comparison of dose calculation algorithms in phantoms with lung equivalent heterogeneities under conditions of lateral electronic disequilibrium.," *Med Phys*, vol. 31, no. 10, pp. 2899-2911, Oct 2004.
- [49] F. Hasenbalg, H. Neuenschwander, R. Mini and E. J. Born, "Collapsed cone convolution and analytical anisotropic algorithm dose calculations compared to VMC++ Monte Carlo simulations in clinical cases.," *Phys Med Biol*, vol. 52, no. 13, pp. 3679-3691, Jul 2007.
- [50] L. R. Aarup, et. al., "The effect of different lung densities on the accuracy of various radiotherapy dose calculation methods: Implications for tumour coverage," *Radiotherapy and Oncology*, vol. 91, no. 3, pp. 405-414, 2009.

- [51] J. Chow, M. Leung and J. Van Dyk, "Variations of lung density and geometry on inhomogeneity correction algorithms: a Monte Carlo dosimetric evaluation.," *Med Phys*, vol. 36, no. 8, pp. 3619-3630, Aug 2009.
- [52] O. I. Calvo, A. N. Gutiérrez, S. Stathakis, C. Esquivel and N. Papanikolaou, "On the quantification of the dosimetric accuracy of collapsed cone convolution superposition (CCCS) algorithm for small lung volumes using IMRT.," *J Appl Clin Med Phys*, vol. 13, no. 3, p. 3751, 2012.
- [53] W. Takahashi, H. Yamashita, N. Saotome, Y. Iwai, A. Sakumi, A. Haga and K. Nakagawa, "Evaluation of heterogeneity dose distributions for Stereotactic Radiotherapy (SRT): comparison of commercially available Monte Carlo dose calculation with other algorithms.," *Radiat Oncol*, vol. 7, p. 20, 2012.
- [54] L. Tillikainen, H. Helminen, T. Torsti, S. Siljamäki, J. Alakuijala, J. Pyyry and W. Ulmer, "A 3D pencil-beam-based superposition algorithm for photon dose calculation in heterogeneous media.," *Phys Med Biol*, vol. 53, no. 14, pp. 3821-3839, Jul 2008.
- [55] A. Fogliata, E. Vanetti, D. Albers, C. Brink, A. Clivio, T. Knöös, G. Nicolini and L. Cozzi, "On the dosimetric behaviour of photon dose calculation algorithms in the presence of simple geometric heterogeneities: comparison with Monte Carlo calculations.," *Phys Med Biol*, vol. 52, no. 5, pp. 1363-1385, Mar 2007.
- [56] V. Panettieri, B. Wennberg, G. Gagliardi, M. A. Duch, M. Ginjaume and I. Lax, "SBRT of lung tumours: Monte Carlo simulation with PENELOPE of dose distributions including respiratory motion and comparison with different treatment planning systems.," *Phys Med Biol*, vol. 52, no. 14, pp. 4265-4281, Jul 2007.
- [57] E. Sterpin, M. Tomsej, B. De Smedt, N. Reynaert and S. Vynckier, "Monte carlo evaluation of the AAA treatment planning algorithm in a heterogeneous multilayer phantom and IMRT clinical treatments for an Elekta SL25 linear accelerator.," *Med*

- Phys*, vol. 34, no. 5, pp. 1665-1677, May 2007.
- [58] A. O. Jones and I. J. Das, "Comparison of inhomogeneity correction algorithms in small photon fields.," *Med Phys*, vol. 32, no. 3, pp. 766-776, Mar 2005.
- [59] X. Jia, X. Gu, J. Sempau, D. Choi, A. Majumdar and S. Jiang, "Development of a GPU-based Monte Carlo dose calculation code for coupled electron--photon transport," *Physics in medicine and biology*, vol. 55, no. 11, p. 3077, 2010.
- [60] J. Deng, T. Guerrero, C. M. Ma and R. Nath, "Modelling 6 MV photon beams of a stereotactic radiosurgery system for Monte Carlo treatment planning.," *Phys Med Biol*, vol. 49, no. 9, pp. 1689-1704, May 2004.
- [61] Y. Yang, E. Schreibmann, T. Li, C. Wang and L. Xing, "Evaluation of on-board kV cone beam CT (CBCT)-based dose calculation.," *Phys Med Biol*, vol. 52, no. 3, pp. 685-705, Feb 2007.
- [62] S. Yoo and F.-F. Yin, "Dosimetric feasibility of cone-beam CT-based treatment planning compared to CT-based treatment planning.," *Int J Radiat Oncol Biol Phys*, vol. 66, no. 5, pp. 1553-1561, Dec 2006.
- [63] G. X. Ding, D. M. Duggan and C. W. Coffey, "Characteristics of kilovoltage x-ray beams used for cone-beam computed tomography in radiation therapy.," *Phys Med Biol*, vol. 52, no. 6, pp. 1595-1615, Mar 2007.

Chapter 2

2 An in-depth Monte Carlo study of lateral electron disequilibrium for small fields in ultra-low density lung: implications for modern radiation therapy

This chapter is adapted from the research article, "An in-depth Monte Carlo study of lateral electron disequilibrium for small fields in ultra-low density lung: implications for modern radiation therapy" published in *Physics in Medicine and Biology*, 2012, March 21;57(6):1543-59 by Disher B, Hajdok G, Gaede S, Battista JJ.

2.1 Introduction

Lung cancer is a leading cause of cancer related death worldwide [1]. A growing number of patients are being diagnosed with earlier stage lung cancer, as a result of increased use of diagnostic computed tomography (CT) scans [2]. Traditional radiation therapy (RT) can be used to treat these patients, but long term survival rates remain low (16%) [3]. A more promising technique, known as stereotactic body radiation therapy (SBRT), has been shown to improve local control of these types of lung tumours [4]. SBRT uses tightly conformed Megavoltage (MV) x-ray fields to irradiate the tumour at high dose levels using few fractions, and with less damage to adjacent normal lung tissue. As well, with the advent of image-guided radiation therapy (IGRT) it is possible to reduce planned margins around tumour volumes, shrink radiation field sizes, and escalate dose. As a result, modern technologies such as intensity modulated radiation therapy (IMRT) are now frequently using sub-centimeter MV photon fields for radiation therapy. [5]

Human lung density can be abnormally low ($\leq 0.1 \text{ g/cm}^3$) for emphysematous lung [6], and up to 0.35 g/cm^3 for healthy lung tissue [7]. For this range of densities the dose distribution is affected by two competing factors: 1) a reduction of photon attenuation, and 2) enhanced secondary electron range. When secondary electron equilibrium is maintained, reduced photon attenuation is the dominating factor, and dose is increased within the lung and tumour tissues [8] compared with dose in an all-water

absorber. In the absence of electron equilibrium, in the lateral/transverse direction, large reductions of the dose distribution occur in lung [9, 10]. For instance, Aarup et al., 2009 used Monte Carlo simulations to virtually irradiate a lung phantom containing a 2 cm diameter spherical tumour with an 18 MV x-ray beam [11]. By reducing the lung density from 0.4 to 0.1 g/cm³, they showed that the mean target dose decreased from 83.3 to 61.6% (relative to water density), respectively. Large dose variations within lung and tumour tissues are possible, and accurate dose algorithms must be chosen to account for these effects. More importantly, clinical trials that do not include any (or include an inaccurate) correction for lung density will yield ambiguous results because the tumour doses will vary for a given dose prescription “in water”.

Dose calculation algorithms can be generalized into two broad categories based on energy deposition modeling [12]. The first category (1) assumes that charged particle equilibrium is always maintained, and it's as if energy deposition occurs “on the spot” of photon interaction; there is no modeling of secondary electron transport. The Modified Batho [13] and equivalent tissue-to-air ratio [14] techniques all fall into this category. The second category (category 2) assumes non-local energy deposition and considers electron transport. Superposition/Convolution [15] methods like the Collapsed Cone Convolution (CCC) [16] and Analytic Anisotropic Algorithm (AAA) [17] analytically model electron transport, while Monte Carlo techniques [18] explicitly track electron transport. The MC approach is generally considered the gold standard for determining dose distributions for circumstances of electron disequilibrium, and where interpretations of dosimetric measurements are challenging. As such, it has been used by many authors to bench mark the accuracy of different dose calculation techniques [11, 19, 20, 21, 22, 23, 24, 25].

It has been shown that category 1 dose algorithms overestimate the amount of dose deposited in lung and tumour tissues under the conditions of lateral electron disequilibrium (LED) [10, 11, 26, 27, 24, 25]. For instance, Engelsman et al., 2001 compared the dose calculating accuracy of multiple category 1 algorithms (pencil beam, modified Batho, and equivalent path length) with film and ion chamber measurements. Beam energies of 6, 8, 15, and 18 MV were used to irradiate a 50 mm polystyrene target

centrally contained within a lung slab, simulated by cork. Their results show that the three algorithms predict up to 20% higher dose levels in the lung and tumour compared with the actual delivered dose values. As well, the error in dose calculation increased with photon beam energy [26].

The ability of category 2 algorithms to accurately compute dose in lung tissue has been assessed by multiple authors. Most studies suggest that type 2 algorithms (AAA and CCC) are superior to type 1 methods for calculating dose when electron equilibrium is not maintained [11, 20, 21, 28, 24, 25]. However, Tillikainen et al., 2008 showed that the AAA algorithm produced errors up to 8% in lung tissue when using small field 18MV x-rays to irradiate a phantom [17]. A more recent comparison of CCC and MC by Chow et al., 2009 suggest that the CCC algorithm produced significant dose deviations in lung phantoms and patients for treatment parameters using high energy beams, small field sizes, and low lung density ($< 0.3 \text{ g/cm}^3$) – the usual conditions that ruin electron equilibrium [29].

Summarizing the literature, it is evident that category 1 algorithms are inadequate for prediction of correct dose in SBRT or IMRT of lung cancer patients. Category 2 algorithms are generally better, but may still be challenged to produce accurate dose distributions under extreme LED due to oversimplification and assumptions in modeling of electron transport [23]. Despite this being an active field of research, no previous efforts have fully explored the range of radiotherapeutic parameters that can lead to unexpected LED in SBRT and other modern techniques. Considering the range of treatment planning protocols and ambiguous dose prescriptions used in SBRT, a comprehensive study focused on this topic is justified and timely.

SBRT protocols set by Radiation Therapy Oncology Group (RTOG) trials [0236, 0618, 0813, and 0915] are used to quantify the conformity and coverage of the dose delivered to the planning target volume (PTV). The PTV is defined by the gross tumour volume (GTV) plus a minimal expansion of approximately 0.5 to 1 cm into lung tissue. The beam aperture is forced to correspond to the beam's eye view projection of the PTV. As a result, the iso-dose lines covering the periphery of the PTV typically range between

60 to 90%. The prescribed dose (20 Gy per fraction x 3 fractions for example) is typically set to the 80% iso-dose shell located at the edge of the PTV within lung tissue. This arrangement forces a hot spot ($\geq 100\%$ of the prescription dose) to occur within the central region of the tumour. Lastly, to ensure that the high dose volume is contained in the vicinity of the tumour, the ratio of the volume of the prescription iso-dose to the volume of PTV should be < 1.2 . Similarly the ratio of the 50% iso-dose volume to the PTV must also conform to specific criteria, which depends on tumour volume. These ratios will be discussed as the high and low dose volumes, respectively.

The treatment parameters used for SBRT of lung cancer patients are more apt to create LED. The SBRT protocols discussed above may not be attainable using modern day dose algorithms, which are more susceptible to error under the conditions of severe LED. Most importantly, the prescription dose is calculated from an iso-dose line within lung tissue where LED dose perturbations are greatest. The actual delivered dose distribution may be drastically different from the dose predicted by a treatment planning system [30, 31, 32]. Therefore a thorough understanding of the combination of radiation treatment parameters that establish LED is essential for SBRT of lung cancer patients if one wishes to avoid the strong dose variations associated with LED.

Although LED in lung RT is well documented [29], most studies present a limited set of variations in beam energy, lung density, and field size. The specific combinations of treatment conditions that create LED are not well known. In this work we use the MC technique to fully characterize the parameters that establish LED. This analysis includes energies from Co-60 up to 18 MV x-rays, including a wide range of clinically relevant field sizes ($1 \times 1 \text{ cm}^2$ up to $15 \times 15 \text{ cm}^2$) and lung densities (0.001 g/cm^3 up to 1 g/cm^3). Additionally, we study the dosimetric effects on various small lung tumour phantoms under the conditions of LED. Finally, the implications of this work are discussed in the context of SBRT and other forms of modern radiation therapy.

2.2 Methods

2.2.1 Monte Carlo codes and parameters

MC simulations were performed using EGSnrc, BEAMnrc, and DOSXYZnrc user codes (National Research Council of Canada, Ottawa, ON). Simulations were conducted simultaneously using a PC-based computer cluster that consisted of 60 independent Intel Xeon central processing units (CPU). The CPUs operated at processing speeds of 2.67GHz or 3.4 GHz. The total RAM available to the cluster was 102 GB.

BEAMnrc [55] was used to generate the phase space file for a Varian 21 EX linear accelerator (Varian Medical Systems Inc., Palo Alto, CA) 6 MV x-ray source ($5 \times 5 \text{ cm}^2$; field size at 100 cm source-to-axis distance). The primary electron beam radius was set to 0.5 mm, and 1×10^8 histories were used to create 5×10^6 particles. The variance reduction technique of selective bremsstrahlung splitting was used to increase computational efficiency. The electron and photon cutoff energies were set as 521 keV, and 10 keV (i.e. ECUT and PCUT), and PRESTA II [33] and EXACT were selected as the electron step and boundary crossing algorithms. These settings were applied for both DOSXYZnrc and BEAMnrc user codes. DOSXYZnrc was used to perform all dose calculations, and 1×10^8 to 8×10^8 histories were simulated. The statistical uncertainty in dose voxels was less than 2% for all calculation points. Also, all dose profiles were normalized to the maximum dose in water per beam and field size.

2.2.2 Experimental validation of Monte Carlo simulation in low density material

EGSnrc, BEAMnrc, and DOSXYZnrc user codes have been used extensively and validated in similar applications [23]. However, we wanted to establish the suitability of the MC technique for dose calculations in an ultra-low density medium. To this effect, dose in air was measured using a slab phantom and the Varian 6 MV ($5 \times 5 \text{ cm}^2$) source. These measurements were acquired with an A1SL Exradin miniature Shonka thimble ion chamber (Standard Imaging Inc, Middleton, WI), and results were compared to DOSXYZ

calculation results to validate the MC technique. The experimental setup consisted of a slab geometry with 5 cm of solid water (Gammex RMI[®], Middleton WI), then 10 cm of air, and followed by another 10 cm of solid water. Similarly, DOSXYZnrc was used to simulate a slab phantom consisting of $20 \times 20 \times 25 \text{ cm}^3$ volume with a voxel size of $0.25 \times 0.25 \times 0.25 \text{ cm}^3$. The slab materials were set to H2O521ICRU (i.e. water, $z = 0 \dots 5 \text{ cm}$), AIR521ICRU (i.e. air, $z = 5 \dots 15 \text{ cm}$), and H2O521ICRU ($z = 15 \dots 25 \text{ cm}$) [see Fig. 2-1]. Dose was calculated using the previously discussed phase space file for the 6 MV input source.

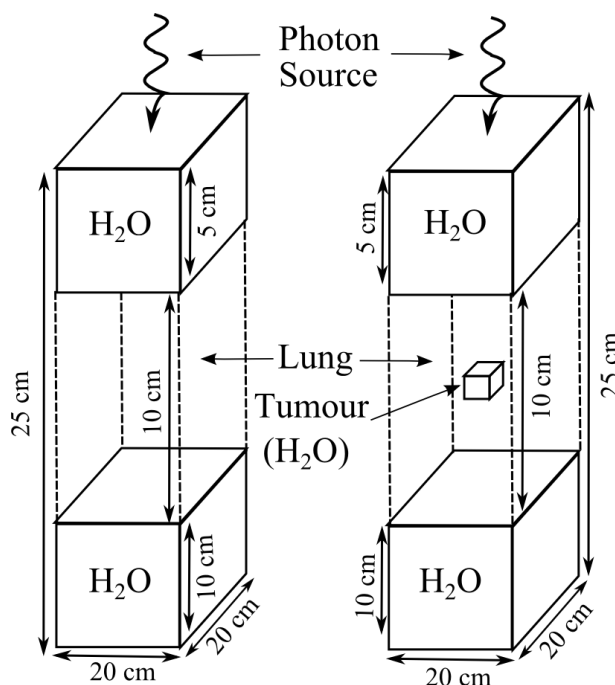


Figure 2-1 Schematic diagrams (not to scale) of the slab phantoms without tumour (shown left) and with tumour (shown right). The cubic water tumour insert ranged in size from $1 \times 1 \times 1 \text{ cm}^3$, $3 \times 3 \times 3 \text{ cm}^3$, and $5 \times 5 \times 5 \text{ cm}^3$. Simulations included combinations of 6 photon sources, 5 field sizes, and 12 lung densities. The lung insert was initially set to AIR521ICRU to validate the Monte Carlo dose calculation in a low density medium.

Figure 2-2(a) shows the central-axis depth-dose comparison between A1SL measurement and MC dose calculation. In the water slab regions, there is excellent agreement between dose calculation and measurement with differences less than 2%. In contrast, in the air region, MC dose is reduced by 31% to 36% compared to measurement. Measuring dose in air from a megavoltage photon field is challenging due to severe LED

[34]. As well, the ion chamber is not totally air-equivalent, contributing 4mm of water build-up that perturbs the equilibrium conditions [35].

To overcome this problem, we also used the MC method to simulate the material and geometrical specifications of the A1SL ion chamber from the manufacturer. The A1SL's shell, collector, guard material, and electrode stem were modeled in DOSXYZnrc and placed at central-axis depths of 1.5, 6, 8, 10, 12, and 14 cm within the slab phantom simulation; a separate dose calculation was made for each depth. Figure 2-2(b) shows the central-axis depth-dose result comparing measurement to MC dose calculation using the modeled A1SL ion chamber. Note that within the air slab, the difference between dose points is now reduced to less than 3%. DOSXYZnrc can accurately model the dose perturbation in air when ion chamber materials are placed within the photon field.

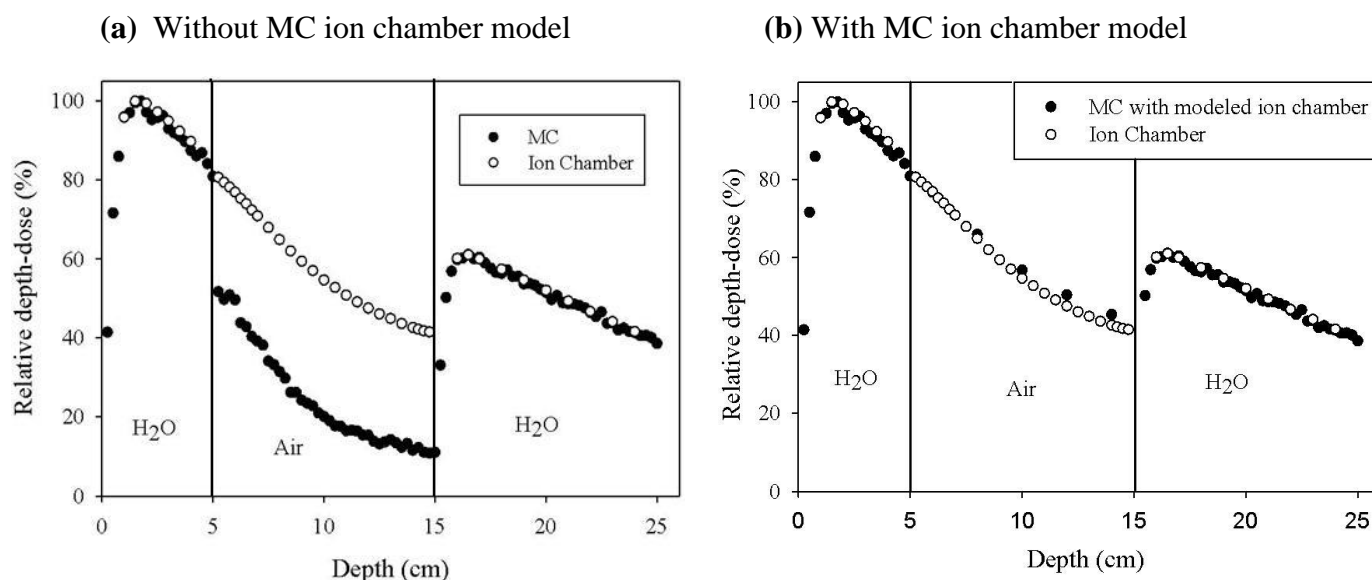


Figure 2-2 compares the MC dose calculation to measurement using the A1SL ion chamber. In the air region the ion chamber perturbs the dose-to-air measurement, reporting erroneously high dose. In **Fig. 2-2 (b)**, we modeled the ion chamber at different depths within the MC slab phantom, and calculated dose to air in the vicinity of the ion chamber; measurement and MC dose calculation were then in agreement.

2.2.3 Monte Carlo simulations of slab phantoms

DOSXYZnrc was also used to study the effects of beam energy, field size, and lung density on dose distributions. Four slabs phantoms were simulated all with identical geometry to the phantom discussed above, except that the air slab was replaced with LUNG521ICRU material. The first phantom contained lung material only, whereas the second, third, and fourth phantoms also included a $1 \times 1 \times 1 \text{ cm}^3$, $3 \times 3 \times 3 \text{ cm}^3$, and $5 \times 5 \times 5 \text{ cm}^3$ water cube insert (see Fig. 2-1). The water cube was meant to mimic a small human tumour located centrally at a depth of 10 cm within the lung material, analogous to lung SBRT conditions.

To characterize LED in lung tissue, dose calculations were performed using photon distributions from therapeutic sources including: Co-60, 4MV, 6MV, 10MV, 15MV, and 18MV spectra [36]. As well, the square field size of each beam was varied between $1 \times 1 \text{ cm}^2$, $3 \times 3 \text{ cm}^2$, $5 \times 5 \text{ cm}^2$, $10 \times 10 \text{ cm}^2$, and $15 \times 15 \text{ cm}^2$. The density of the lung slab was decreased from 1 to 0.001 g/cm^3 (1, 0.9, 0.8, 0.7, 0.6, 0.5, 0.4, 0.3, 0.2, 0.1, 0.01, and 0.001 g/cm^3). A total of 1440 simulations were performed for all combinations of beam energy, field size, and lung density (6 energies, 5 field sizes, 12 lung densities, and 4 phantoms). Dose was “scored” at depth along the central-axis of the phantoms into volume bins of $0.25 \times 0.25 \times 0.25 \text{ cm}^3$ for each simulation. Similarly, transverse-axis dose was also scored at a depth of 10 cm within the phantoms using the same sized volume bins.

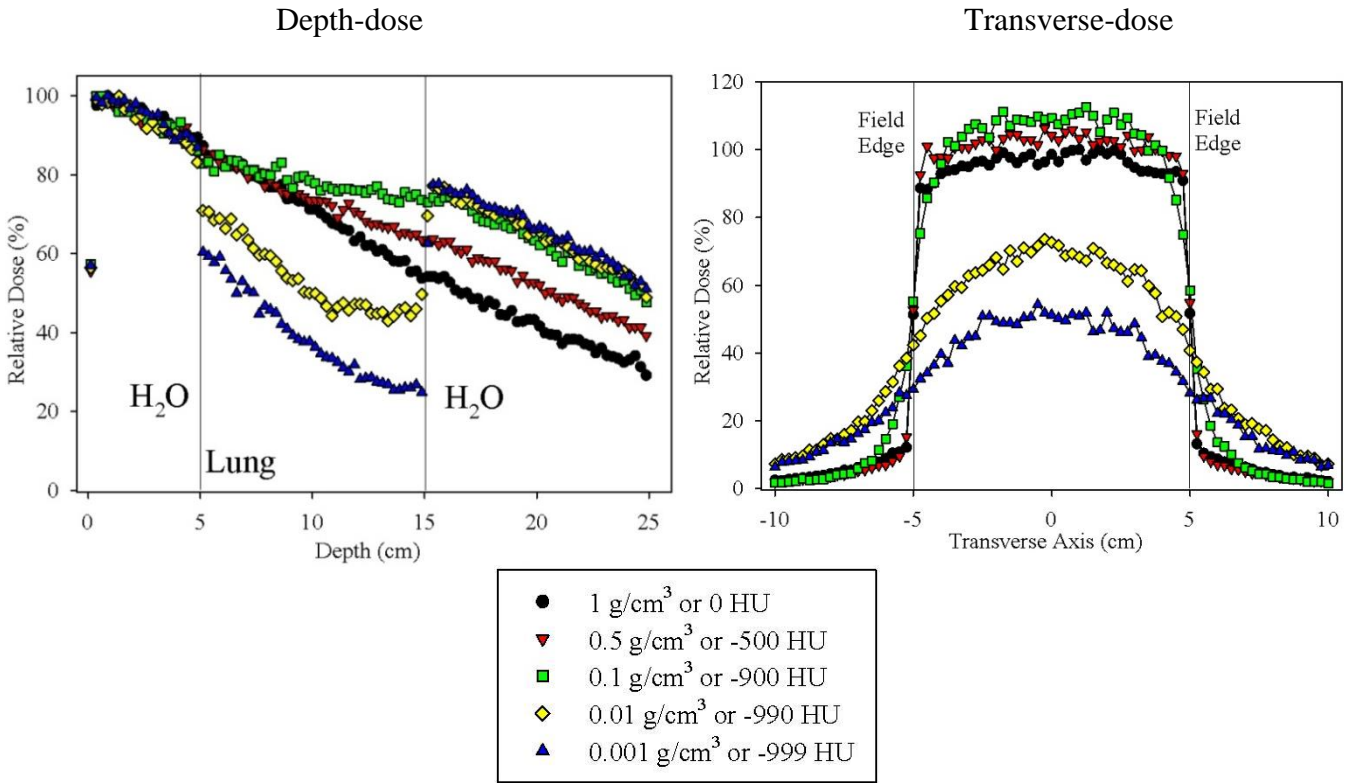
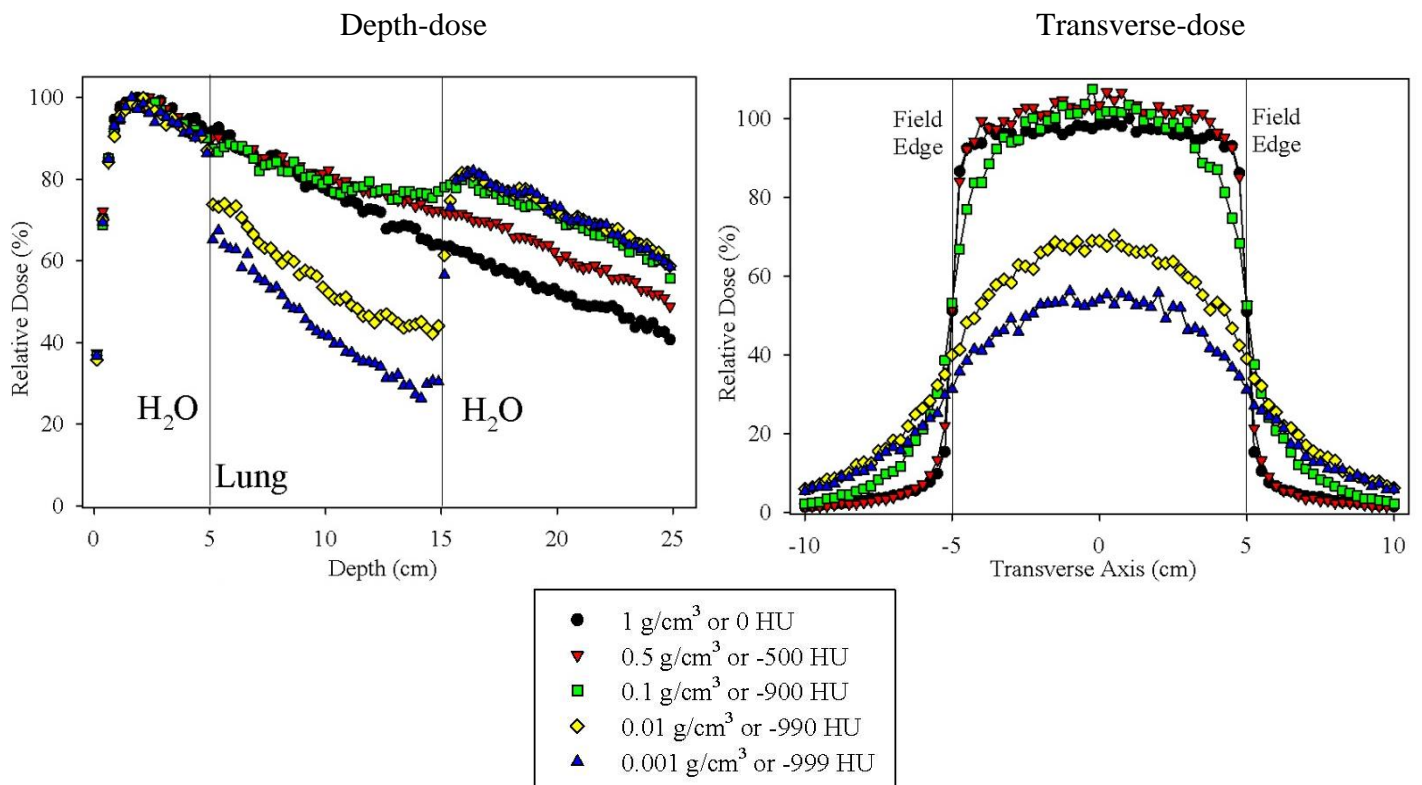
2.3 Results

2.3.1 Monte Carlo simulations of slab phantoms; no tumour insert

Figure 2-3 shows selected depth-dose and transverse-dose (at $d = 10 \text{ cm}$) profiles for various lung slab densities, beam energies (1.25, 6 and 18 MV), and a $10 \times 10 \text{ cm}^2$ field size. In Fig. 2-3 (a), (b), and (c) photon fluence was generally enhanced by decreasing the lung slab density, which increased the central-axis dose in and beyond the lung slab, as can be expected intuitively. However, for lung densities below the “critical density”,

LED occurs, and there is an observed sudden decrease lung dose. For example, in Fig. 2-3 (a) the critical lung density is 0.1g/cm^3 , and the central-axis depth-dose decreased by as much 46% (relative to water) for a density of 0.001 g/cm^3 . Note for Fig. 2-3 (b) and (c), the critical densities are 0.1g/cm^3 and 0.2g/cm^3 , respectively (not shown in Fig. 2-3). For ultra-low densities ($\rho_{\text{lung}} < 0.1\text{ g/cm}^3$), the lateral electron range of secondary electrons was significantly expanded, and became comparable or larger than the lateral beam radius (5 cm). Electrons liberated from the central-axis of the beam escaped beyond the field edge, and could not be replaced, which reduced the central-axis depth-dose and increased the transverse-dose beyond the field edge. The observed central-axis dose depression is the hallmark of severe lateral electron disequilibrium [29, 10, 36, 37, 23, 38].

Figure 2-4 displays similar results to those shown in Fig. 2-3 except the photon field size was reduced to $3\times 3\text{cm}^2$. The critical lung densities extracted from Fig. 2-4 (a), (b), and (c) are 0.2, 0.4, and 0.7 g/cm^3 , respectively. Note that LED occurs for higher lung densities than those reported in Fig. 2-3, which are in the range of clinically-observed normal lung densities. By shrinking the field size from $10\times 10\text{ cm}^2$ down to $3\times 3\text{cm}^2$, the lateral range of secondary electrons required to establish LED is only 1.5cm, and electron transports previously inhibited by higher density lung can now reach the closer field edge. As well, both Figs 2-3 and 2-4 demonstrate that higher beam energy imparts more kinetic energy to laterally scattered electrons, which can easily escape the beam periphery for lower density lung and smaller field sizes.

(a) 1.25 MV (10×10 cm²)(b) 6 MV (10×10 cm²)

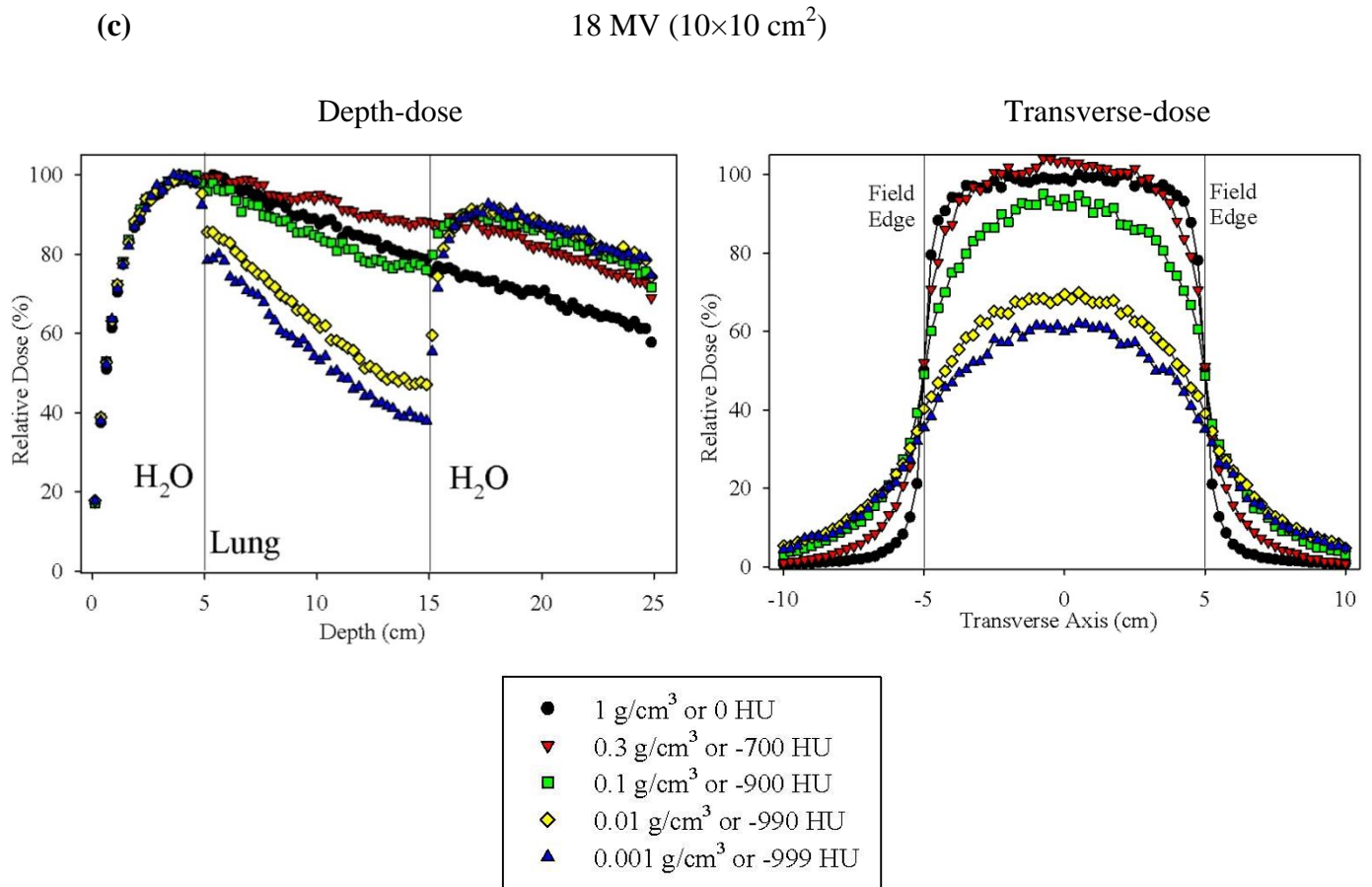


Figure 2-3 Monte Carlo calculated dose profiles for a slab phantom geometry with decreasing lung slab density (1.25 MV, 6 MV, 18 MV photon sources $10 \times 10 \text{ cm}^2$ field). The left column corresponds to central-axis depth-dose profiles. The right column corresponds to transverse-dose profiles acquired at the 10 cm depth within the phantom.

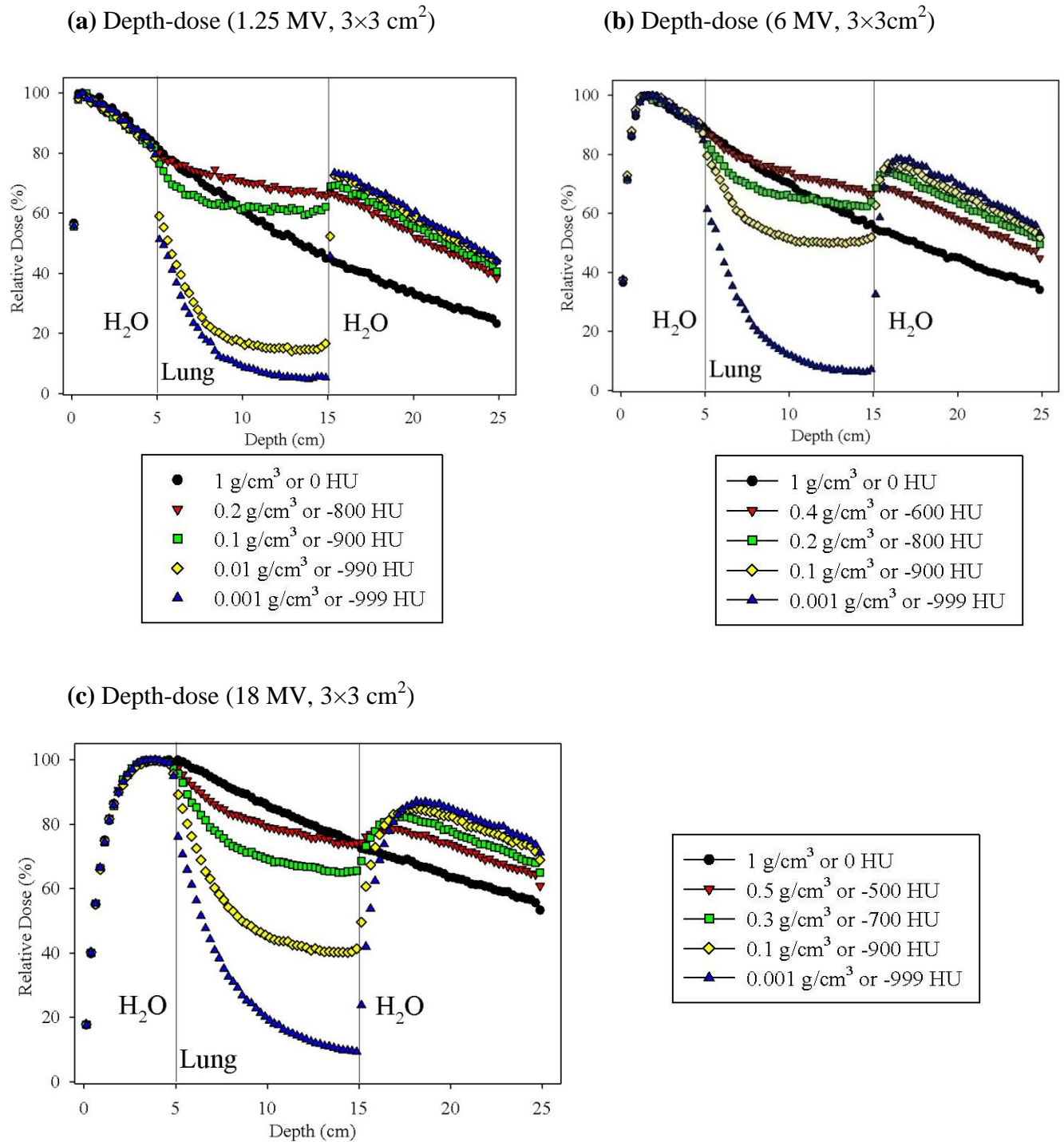


Figure 2-4 Monte Carlo calculated central-axis depth-dose profiles for a slab phantom geometry with decreasing lung slab density (1.25 MV, 6 MV, 18 MV photon sources $3 \times 3 \text{ cm}^2$ field).

2.3.2 Quantifying electron disequilibrium: relative depth-dose factors

The clinical conditions that create LED are dependent upon beam energy (E), field size (FS), and lung density (ρ_{lung}). To quantify the variations in central-axis depth-dose for the full range of treatment conditions we used the percent depth-dose value in lung, $PDD(E, FS, \rho_{lung})$, acquired at a depth of 10 cm. We then defined a ratio, the relative depth-dose factor (RDDF), to describe the extent of LED:

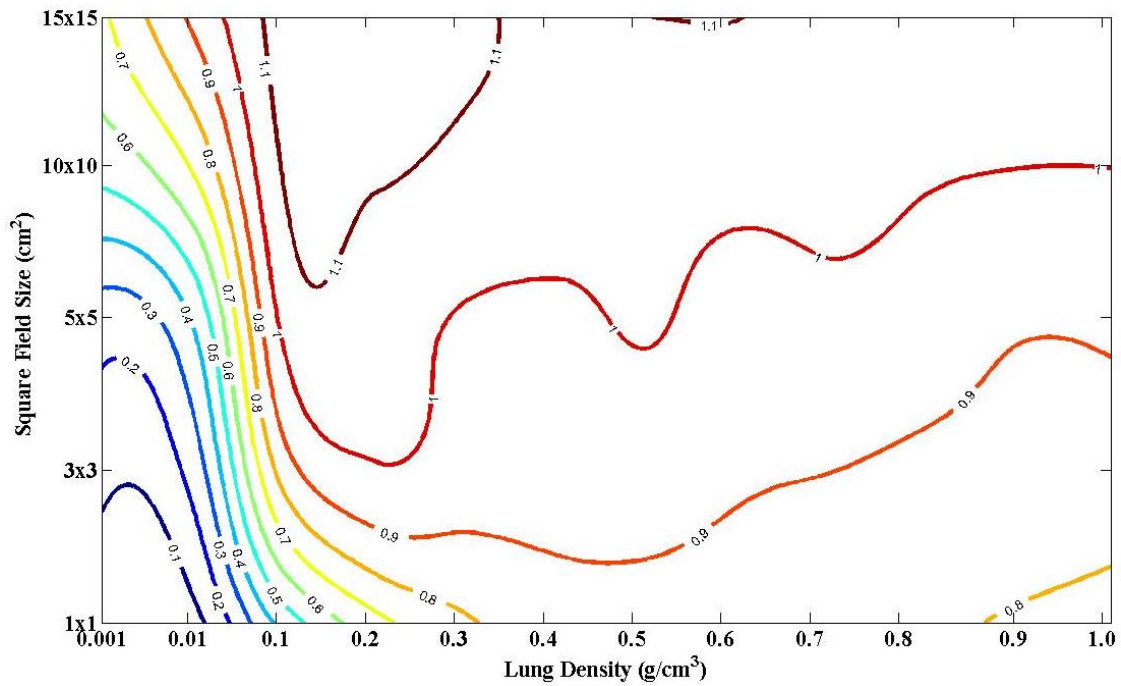
$$RDDF = \frac{PDD(E, FS, \rho_{lung})}{PDD(E, 10 \times 10 \text{ cm}^2, 1 \text{ g/cm}^3)} \quad (2.1)$$

For $RDDF \geq 1$, electron equilibrium is maintained at the central-axis, and $RDDF < 1$ represents conditions that disrupt equilibrium. The choice of normalization to water was based on two key factors: assured electron equilibrium and an often-used calibration condition. For example, from Figs **2-3 (b)** and **2-4 (b)** we can calculate $PDD(6 \text{ MV}, 10 \times 10 \text{ cm}^2, 1.0 \text{ g/cm}^3)$ and $PDD(6 \text{ MV}, 3 \times 3 \text{ cm}^2, 0.001 \text{ g/cm}^3)$ to be 78% and 12%, respectively. Taking the ratio of these values produces an RDDF (6 MV, $3 \times 3 \text{ cm}^2$, 0.001 g/cm^3) of 0.15. Using RDDF, we can estimate the severity of LED and the amount of central-axis depth-dose reduction within lung tissue as a result of selecting a specific combination of radiotherapy parameters.

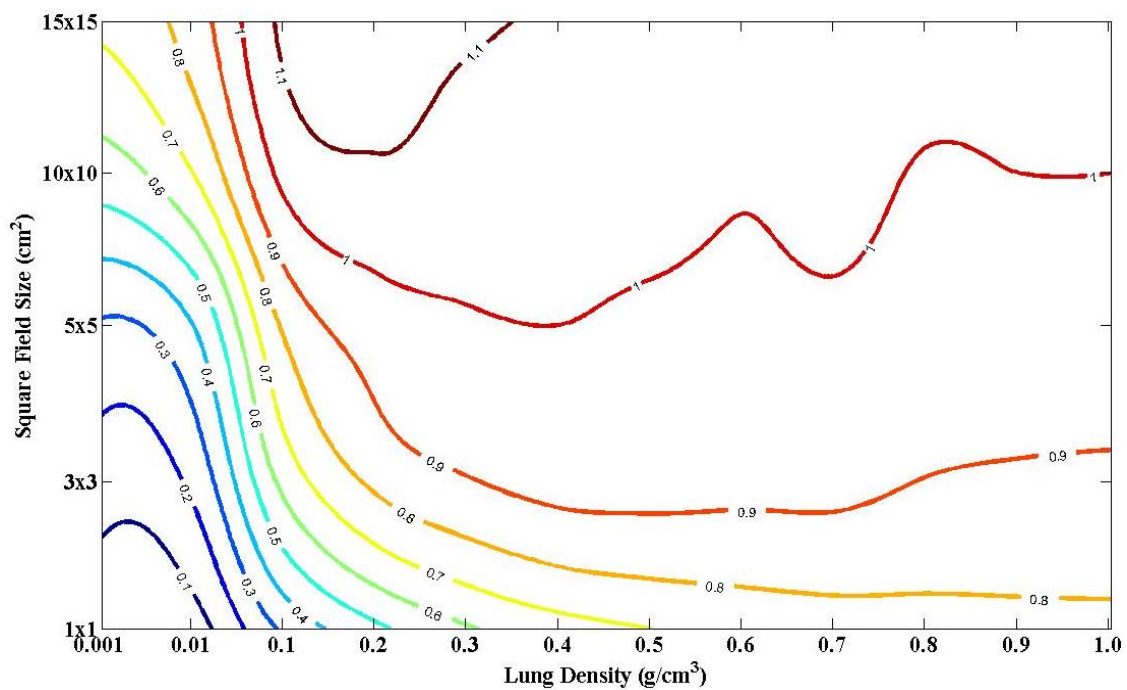
Figures **2-5 (a)**, **(b)**, and **(c)** map iso-contour RDDF values for some selected energies: Co-60, 6, and 18 MV. In Fig. **2-5 (a)**, regions of severe LED ($RDDF \leq 0.7$) occur primarily for ultra-low lung densities ($< 0.1 \text{ g/cm}^3$) and field sizes less than $5 \times 5 \text{ cm}^2$. In Fig. **2-5 (b)**, the regions of LED begin to spread out, and low RDDF values occur for larger field sizes ($FS \leq 10 \times 10 \text{ cm}^2$) and higher lung densities ($\rho_{lung} < 0.5 \text{ g/cm}^3$). As a result of using 18 MV photon energies, the iso-contour lines expand the most in Fig. **2-5 (c)**, and LED can even occur in adipose-like tissues ($0.7 \text{ g/cm}^3 < \rho_{lung} < 1.0 \text{ g/cm}^3$) and the largest field sizes ($FS \leq 15 \times 15 \text{ cm}^2$). Finally, the RDDF metric showed that lung density and field size are inversely related, and severe LED can be established for small field

sizes and low lung densities. This is expected since the lateral range of electrons is density-dependent and defines the “access” to the field edge.

(a) RDDF ratios for 1.25 MV photon energy



(b) RDDF ratios for 6 MV photon energy



(c) RDDF ratios for 18 MV photon energy

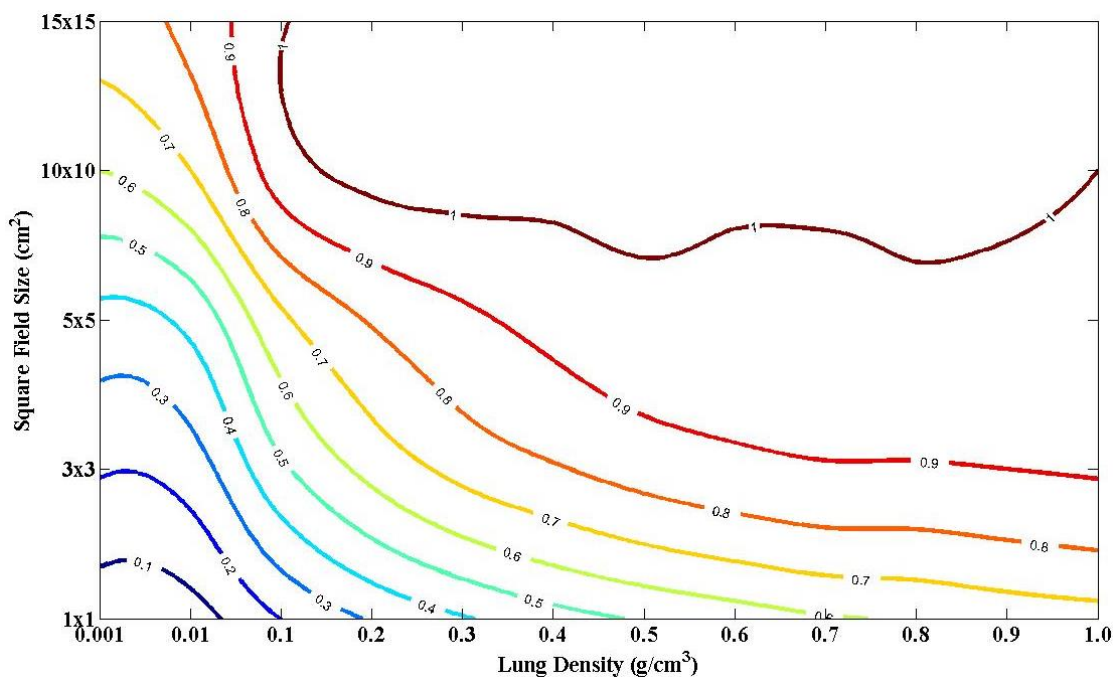


Figure 2-5 iso-contour lines displaying RDDF ratios for various combinations of field size, lung density, and beam energies (1.25 MV, 6 MV, 18 MV). Oscillations in contour lines are due to interpolation limitations over a sparsely populated matrix (5 field sizes by 12 densities).

Each point in Fig. 2-6 displays the combination of treatment parameters that established RDDFs approximately equal to 0.95, or 95% electron equilibrium. This map was created by linearly interpolating the two lung densities that produce RDDF values just above and below 0.95. For example, from Fig. 2-4 (b) RDDF (6 MV, 3x3cm², 0.3g/cm³) and RDDF (6 MV, 3x3cm², 0.2g/cm³) are 0.98 and 0.93, respectively. Thus, a lung density of 0.25g/cm³ would produce a RDDF value of 0.95 for a 6 MV, 3x3cm² photon source. In Fig. 2-6, regions below each curve (pushing to the bottom left) represent the treatment conditions necessary to cause LED with a single field.

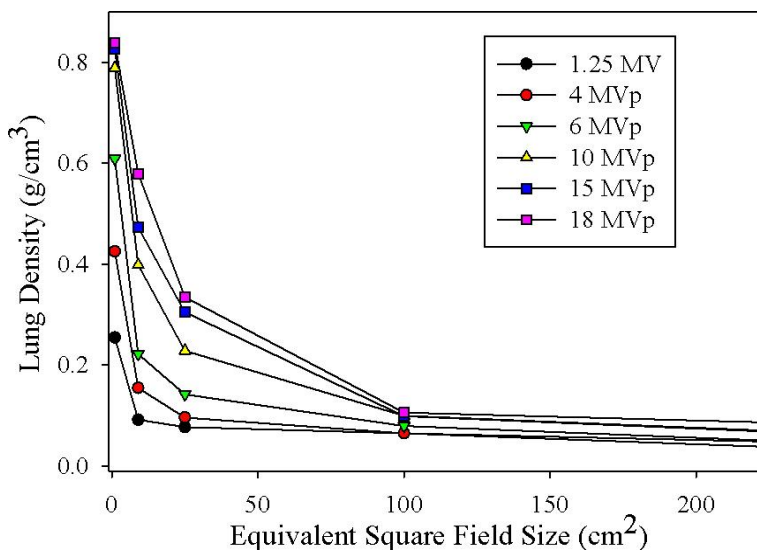


Figure 2-6 95% electron equilibrium curves showing the conditions required to cause lateral electron disequilibrium in a lung phantom using single MV photon fields of various energies and field size. LED regions occur below each line.

2.3.3 Monte Carlo simulations of slab phantoms; with small tumour insert

Figure 2-7 shows depth-dose profiles of the lung slab phantom (including a 3x3x3 cm³ tumour) for 6 and 18 MV photon fields (5x5 cm²), and variable lung densities. Despite the expected “build-up” effect of the tumour insert, LED still occurred and caused a reduction of dose within the lung tissue, and variable dose level within the tumour phantom. In Fig 2-7 (a), dose to the proximal and distal tumour surfaces (depths = 8.5 and 11.5cm) were reduced by 11% and 15% with respect to the water density calculation for severe LED (lung density = 0.001g/cm³; RDDDF = 0.3). On the contrary, the dose at the tumour center (depth = 10cm) was enhanced by 8% with respect to the water density calculation. A comparable simulation is shown in Fig. 2-7 (b), which used an 18 MV (5x5cm²) photon field for dose calculation. Similarly, dose to the proximal and distal tumour surfaces were reduced by 24% and 16%. Dose in the tumour center was minimally enhanced by 2% with regard to the water density calculation.

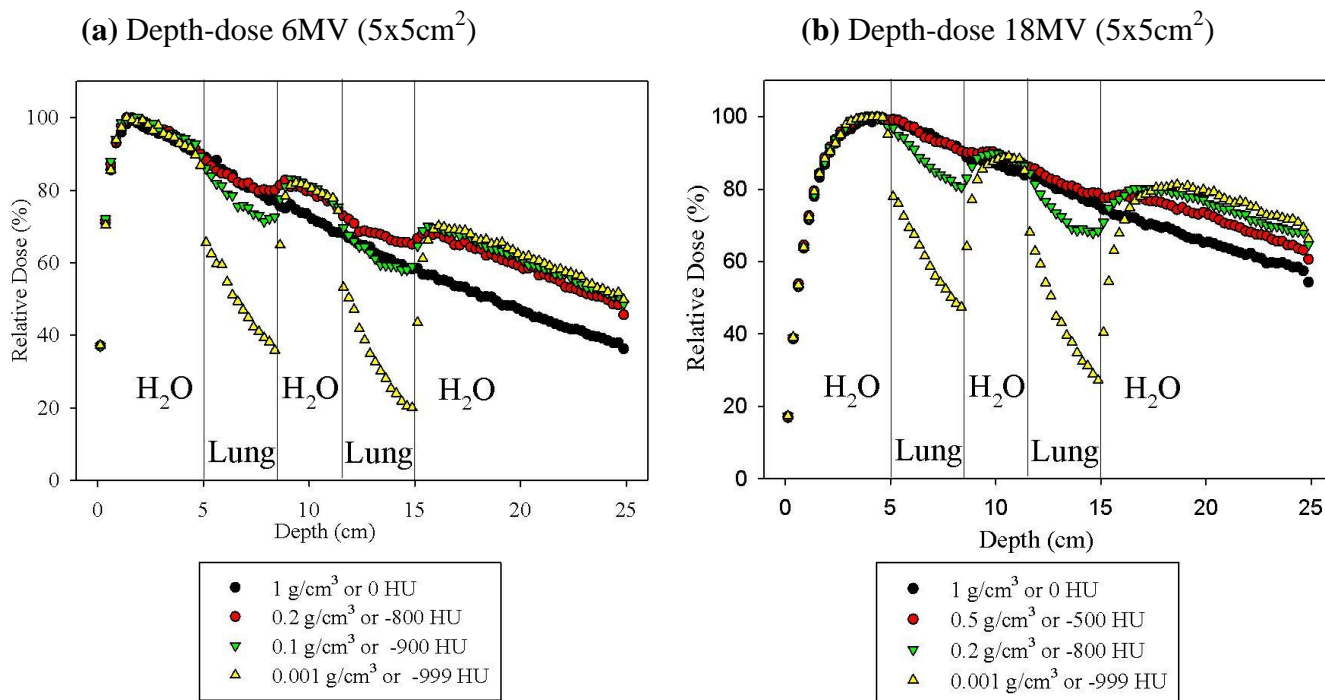


Figure 2-7 Monte Carlo calculated central-axis depth-dose profiles for the lung slab phantom geometry (including a $3 \times 3 \times 3 \text{ cm}^3$ tumour) with decreasing lung slab density.

Figure 2-8 shows depth-dose profiles in the lung slab phantom (including a $1 \times 1 \times 1 \text{ cm}^3$ tumour) for 6 and 18 MV photon fields ($3 \times 3 \text{ cm}^2$), and variable lung densities. Note that reduced depth-dose values occurs for higher lung densities (compared to Fig. 2-7), which was due to a smaller field size. Fig. 2-8 is similar to Fig. 2-7 except the depth-dose reduction within the tumour was more severe. For instance, in Fig 2-8 (a) and (b), the dose in the tumour center with lung density of 0.001 g/cm^3 (RDDF ≈ 0.2) was reduced by 10% and 20% compared to the calculated dose in an all water phantom. As well, the proximal and distal surfaces of the tumour were both greatly under-dosed in Fig. 2-8 (a) and (b).

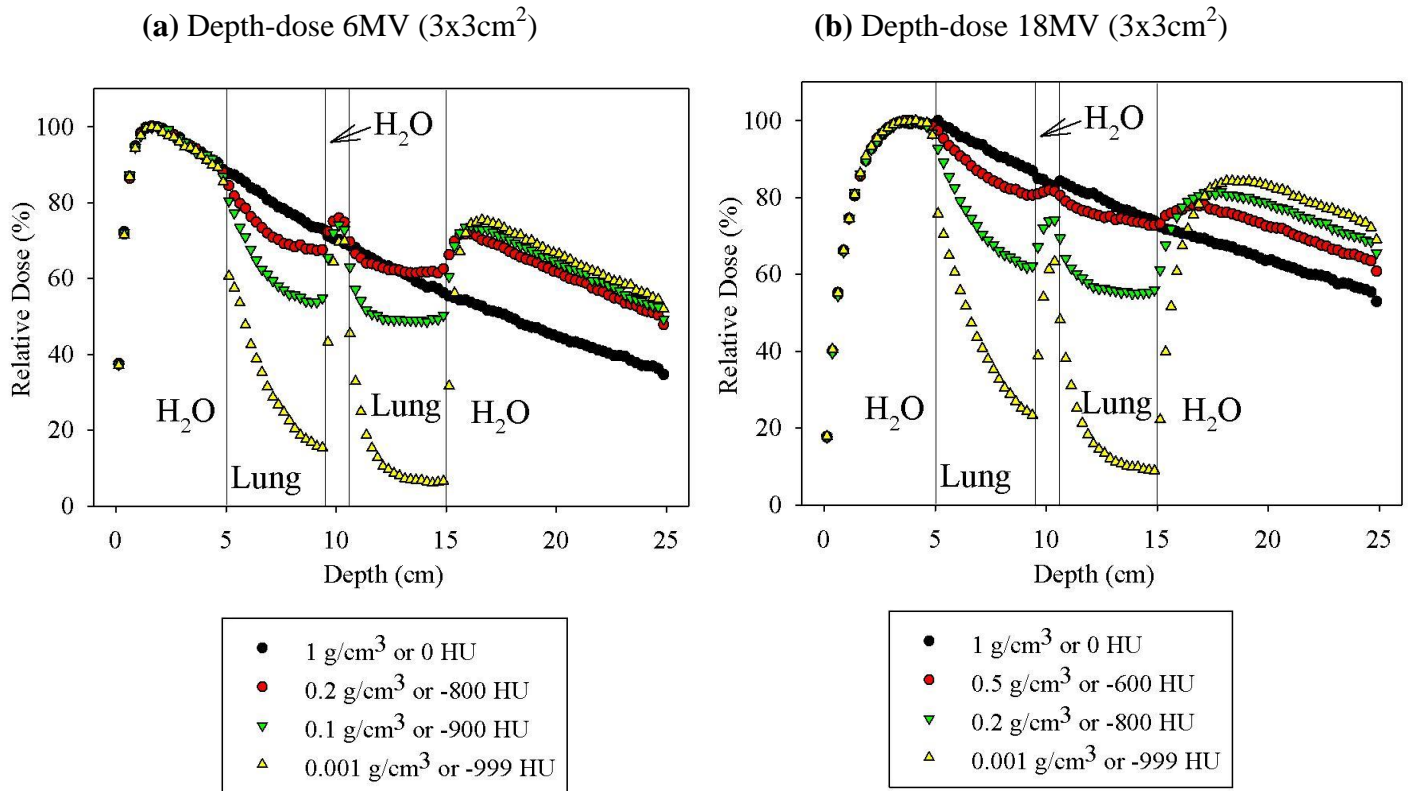


Figure 2-8 Monte Carlo calculated central-axis depth-dose profiles for the lung slab phantom geometry (including a $1 \times 1 \times 1 \text{ cm}^3$ tumour) with decreasing lung slab density.

For both Figs. 2-7 and 2-8, reductions in dose to the proximal and distal surfaces of the tumour were due to LED in up-stream and down-stream lung tissue. Elevated central tumour dose resulted from reduced photon attenuation in lung. Low lung density up-stream from the tumour reduced attenuation of the photon field, which conserved photon fluence for interaction with the tumour volume. Most importantly, note that central tumour dose depends on the beam energy and tumour size in addition to LED conditions. Higher energy photon fields require more water depth to reach full build-up conditions (i.e. d_{max} in water). In Fig. 2-8 (b), under conditions of LED, complete rebuild-up is not achieved as an 18 MV beam requires approximately 3.5 cm of water to reach maximum dose in water (i.e. d_{max}). The tumour was only 1 cm in thickness, which was insufficient to attain full build-up conditions.

2.4 Discussion

2.4.1 Dose calculations within lung tissue: quantifying electron disequilibrium

Figures 2-3 and 2-4 display depth-dose profiles acquired from the lung phantom with no tumour insert for various irradiation and tissue density parameters. These figures were chosen as they represent the lower, middle, and upper bounds of all possible combinations of beam energy, field size, and lung density. Similar results were obtained for other simulations using other combination of parameters. In general, for a given beam energy and field size, dose within lung tissue increased for reduced lung density if equilibrium conditions prevail. This trend continued until the onset of LED, whereby a drastic reduction in lung depth-dose occurred. This effect has been observed and studied previously [10, 39, 11, 38, 25, 23, 19, 20, 24, 27], but the interplay of beam energy, field size, and lung density has not been fully explored, especially in the context of lung SBRT and IMRT.

Clinics wishing to perform SBRT of lung cancer patients can use Figs. 2-5 and 2-6 for considering the risk of LED. For instance, from Fig. 2-5 it is evident that severe LED can be avoided by choosing a low energy beam (< 6 MV) and medium field sizes ($> 5 \times 5$ cm²) for radiation therapy of lung cancer patients. However, if a small field ($< 1 \times 1$ cm²) or low lung density (< 0.1 g/cm³) is encountered, the deleterious effects of LED are unavoidable. The RDDDF values reported in Fig. 2-5 can also impact the choice of dose algorithm. For clinics using dose algorithms that do not account for electron scatter (i.e. category 1), we suggest using a combination of treatment parameters that force RDDDF ≥ 1 . Otherwise, if the conditions for LED are satisfied, there is a serious risk of producing erroneous dose calculations and distributions upon which prescriptions are based. Figure 2-6 can be used as an aid for clinicians to select radiation therapy parameters that avoid the dose effects of LED, particularly when the accuracy of the dose algorithm is in question.

2.4.2 Effect of electron disequilibrium on lung tumour dose

Of the studies relevant to SBRT of lung cancer patients [26, 20, 22, 21, 40, 11, 41, 8], few have used MC simulation to study the effect of LED on lung tumour dose. Most studies assume that the dose algorithm can produce accurate calculations within heterogeneous tissues, and do not explore the space of possible irradiation parameters. Since LED is an effect that is interdependent on beam energy, field size, and lung density, our study spanned a wide scope of combinations of these parameters.

Our work indicates that the dose distribution located within the tumour is highly variable when LED occurs, which may greatly influence fulfillment of the dose prescription. Under-dosage occurred at both the distal and proximal tumour surfaces for the conditions of LED. Most importantly, the dose at the tumour center depends on beam energy and tumour size. The beam energy should be chosen such that the tumour diameter is larger than the required depth to longitudinal equilibrium (e.g. $d_{\max} \sim 2$ cm for 6 MV). Otherwise, if LED occurs, there is a high risk of severely under-dosing the tumour (see Fig. 2-8 (b)) if the dose prescription does not account for disequilibrium. In addition, cold spots can occur near beam edges.

Lastly, the primary goal of this work was to quantify the radiation therapy parameters that fundamentally cause LED. To this end, we investigated single fields of radiation and homogeneous phantoms to isolate the LED effect (note, within the spatial resolution of MC runs, microscope and interface dose effects were assumed to occur locally, and were not of clinical importance). However, the extrapolation of these findings to clinical scenarios requires further investigation. For example, when planning involves multiple fields of radiation and IMRT optimization, any dose deficiencies delivered from one field are accounted for by adjusting intensities from other fields [42] provided the dose calculation algorithm (i.e. category 2) correctly models LED. Comparison of IMRT treatment plans using 6 MV versus 18 MV beam energies for lung cancer patients showed marginal differences between calculated dose distributions [43, 44]. Therefore a future study using reliable MC analysis (e.g. DOSXYZnrc) and multiple fields of radiation would be useful to justify the clinical use of the RDDF metric in heterogeneous patient lung/geometry.

2.4.3 Implications for SBRT clinical protocols and lung cancer patients with emphysema

In-line with SBRT protocols, the prescription dose should correspond with the 80% iso-dose line at the tumour edge. This prescription assumes that electron equilibrium conditions will prevail. Figures 2-7 and 2-8 suggest that the dose distribution at the periphery of the tumour (within lung tissue) varies greatly once equilibrium has been perturbed. Selecting a dose algorithm that does not account for electron scatter (i.e. category 1) will inaccurately portray the dose distribution within the vicinity of the tumour; the predicted and delivered dose distributions will be drastically different [31]. Further, LED has the effect of increasing the beam penumbra [45] [39] [46], spreading out the dose to healthy adjacent lung. This makes fulfilling the high and low volume dose-volume constraints challenging and potentially misleading if the penumbral profile is miscalculated [31]. This implies the recommendations based upon clinical trials using dose calculations in homogeneous tissue (i.e. assuming a lung density of 1.00 g/cm^3) may lead to uninterpretable clinical outcomes due to uncontrolled dose at the tumour (RTOG 0236, and 0618). More recent protocols still recommend the use of either category 1 or 2 algorithms for delivery of SBRT to lung cancer patients [30]. Given the large changes in the dose distribution for LED conditions, we recommend that treatment planning for SBRT in lung be based on a minimum of category 2 algorithms and preferably Monte Carlo methods described herein.

Observing Figs 2-3 through 2-8, the detrimental effects of LED are the most common across all field sizes and beam energies for lung densities below 0.1 g/cm^3 . These results are relevant for SBRT/IMRT planning of radiotherapy patients afflicted with emphysema as well as lung cancer. Recently, it has been suggested that this cohort of patients present a dosimetric challenge as the tumour is poorly covered, and SBRT protocols are ill-defined dosimetrically [47]. Some studies suggest that as much as 90% of patients with bronchogenic carcinoma also present with chronic obstructive pulmonary disease (COPD), a category of lung disease that includes emphysema [48]. Given that emphysema is an independent risk factor for lung cancer [49, 50] it is highly likely that SBRT/IMRT will be used to treat many lung cancer patients with low lung density

caused by emphysema. It is suggested that future SBRT trials also consider the effects of emphysematous lung tissue on the dose distribution.

2.4.4 Electron disequilibrium creates a hyper-sensitive density dependent dose distribution

In the past, it has been suggested that the dose distribution in lung is relatively insensitive to changes in lung density, assuming electron equilibrium. Parker et al. stated that a 5% uncertainty in CT derived density resulted in a deviation of 1% in the calculated dose within inhomogeneous tissue [51]. Sontag et al. reported similar results by varying the lung density of simple inhomogeneous phantom. Changing the lung density by 10% (from 0.5 g/cm^3 to 0.55 g/cm^3) dose inaccuracies of 1.6% and 2.3% were reported at depths of 9cm and 21cm, respectively [14]. These findings, however, were relevant to circumstances involving electron equilibrium. For conditions of LED, these sensitivity ratios are no longer valid as demonstrated amply in our study. Our work suggests that the dose distribution in lung is strongly dependent upon lung density once LED occurs. For example, in Fig. 2-4 (b) at a depth of 15 cm, the percent depth-dose for lung slab densities of 0.1 g/cm^3 (i.e. -900 HU) and 0.01 g/cm^3 (i.e. -990 HU) are 51% and 18%, respectively. These changes represent only a 10% reduction of HU value, but a ten-fold reduction in density, and 48% reduction in central-axis dose under conditions of LED. Therefore, in the range of ultra-low lung density, the sensitivity of dose calculations to variations in lung density is greatly accentuated and these conditions can certainly occur for SBRT or IMRT of lung lesions. This is a concern for SBRT planning using CT-derived density from new on-line CT technologies (e.g. cone beam CT mounted on a linear accelerator [52]). These CT systems use a broad-beam geometry to scan the patient's anatomy, and are more susceptible to artifacts and miscalibrations [53, 54]. As a result, CT-derived density is less accurate and could lead to erroneous computed dose distributions in lung tissue. A study focused on lung dose variations (for conditions of LED) due to inaccurate CT-derived density would be useful.

2.5 Conclusions

This study used Monte Carlo simulations to determine the physical conditions that cause lateral electron disequilibrium in a lung phantom. The findings of this work are useful for oncologists and physicists wanting to avoid the dosimetric complications associated with unexpected LED that is not predicted by some dose algorithms. We recommend that future SBRT clinical trials only be conducted using dose calculating methods that account for electron scatter (i.e. Monte Carlo and category 2 algorithms only). Finally, special attention should be given to patients that present with emphysematous lung. These patients are much more susceptible to the detrimental effects of LED due to extremely low lung density.

2.6 Acknowledgements

The authors would like to thank: Professor Jake Van Dyk, Dr. Jeff Chen, and Dr. David Turnbull for helpful advice in development of this work. As well, we recognize and thank Mr. Matthew Mulligan for assistance with Monte Carlo simulations. Financial support from the Natural Sciences and Engineering Research Council of Canada (NSERC), and the Canadian Institutes of Health Research (CIHR) are also gratefully acknowledged.

2.7 Reference

- [1] A. J. Fakiris, R. C. McGarry, C. T. Yiannoutsos, L. Papiez, M. Williams, M. A. Henderson and R. Timmerman, "Stereotactic Body Radiation Therapy for Early-Stage Non-Small-Cell Lung Carcinoma: Four-Year Results of a Prospective Phase II Study," *International Journal of Radiation Oncology*Biography*Physics*, vol. 75, no. 3, pp. 677-682, 2009.
- [2] C. I. Henschke, D. F. Yankelevitz, D. M. Libby, M. W. Pasmantier, J. P. Smith and

- O. S. Miettinen, "Survival of patients with stage I lung cancer detected on CT screening.," *N Engl J Med*, vol. 355, no. 17, pp. 1763-1771, Oct 2006.
- [3] P. C. Cheung, W. J. Mackillop, P. Dixon, M. D. Brundage, Y. M. Youssef and S. Zhou, "Involved-field radiotherapy alone for early-stage non-small-cell lung cancer.," *Int J Radiat Oncol Biol Phys*, vol. 48, no. 3, pp. 703-710, Oct 2000.
- [4] J. H. Heinzerling, B. Kavanagh and R. D. Timmerman, "Stereotactic Ablative Radiation Therapy for Primary Lung Tumors," *The Cancer Journal*, vol. 17, no. 1, pp. 28--32 10.1097/PPO.0b013e31820a7f80, 2011.
- [5] I. J. Das, G. X. Ding and A. Ahnesjö, "Small fields: nonequilibrium radiation dosimetry.," *Med Phys*, vol. 35, no. 1, pp. 206-215, Jan 2008.
- [6] G. R. Washko, et al., "Lung Volumes and Emphysema in Smokers with Interstitial Lung Abnormalities," *New England Journal of Medicine*, vol. 364, no. 10, pp. 897-906, 2011.
- [7] L. J. Rosenblum, R. A. Mauceri, D. E. Wellenstein, F. D. Thomas, D. A. Bassano, B. N. Raasch, C. C. Chamberlain and E. R. Heitzman, "Density patterns in the normal lung as determined by computed tomography.," *Radiology*, vol. 137, no. 2, pp. 409-416, Nov 1980.
- [8] E. Yorke, L. Harisiadis, B. Wessels, H. Aghdam and R. Altemus, "Dosimetric considerations in radiation therapy of coin lesions of the lung.," *Int J Radiat Oncol Biol Phys*, vol. 34, no. 2, pp. 481-487, Jan 1996.
- [9] P. E. Metcalfe, T. P. Wong and P. W. Hoban, "Radiotherapy X-ray beam inhomogeneity corrections: the problem of lateral electronic disequilibrium in lung.," *Australas Phys Eng Sci Med*, vol. 16, no. 4, pp. 155-167, Dec 1993.
- [10] T. R. Mackie, E. e. Khatib, J. Battista, J. Scrimger, J. { . Dyk } and J. R. Cunningham, "Lung dose corrections for 6- and 15-MV x rays.," *Med Phys*, vol. 12, no. 3, pp.

327-332, 1985.

- [11] L. R. Aarup, et al., "The effect of different lung densities on the accuracy of various radiotherapy dose calculation methods: Implications for tumour coverage," *Radiotherapy and Oncology*, vol. 91, no. 3, pp. 405-414, 2009.
- [12] J. W. Wong and J. A. Purdy, "On methods of inhomogeneity corrections for photon transport.," *Med Phys*, vol. 17, no. 5, pp. 807-814, 1990.
- [13] K. J. Cassell, P. A. Hobday and R. P. Parker, "The implementation of a generalised Batho inhomogeneity correction for radiotherapy planning with direct use of CT numbers.," *Phys Med Biol*, vol. 26, no. 5, pp. 825-833, Sep 1981.
- [14] M. R. Sontag and J. R. Cunningham, "The equivalent tissue-air ratio method for making absorbed dose calculations in a heterogeneous medium.," *Radiology*, vol. 129, no. 3, pp. 787-794, Dec 1978.
- [15] N. Papanikolaou, et al., "Investigation of the convolution method for polyenergetic spectra.," *Med Phys*, vol. 20, no. 5, pp. 1327-1336, 1993.
- [16] A. Ahnesjö, P. Andreo and A. Brahme, "Calculation and application of point spread functions for treatment planning with high energy photon beams.," *Acta Oncol*, vol. 26, no. 1, pp. 49-56, 1987.
- [17] L. Tillikainen, H. Helminen, T. Torsti, S. Siljamäki, J. Alakuijala, J. Pyyry and W. Ulmer, "A 3D pencil-beam-based superposition algorithm for photon dose calculation in heterogeneous media.," *Phys Med Biol*, vol. 53, no. 14, pp. 3821-3839, Jul 2008.
- [18] P. Andreo, "Monte Carlo techniques in medical radiation physics.," *Phys Med Biol*, vol. 36, no. 7, pp. 861-920, Jul 1991.
- [19] A. Fogliata, E. Vanetti, D. Albers, C. Brink, A. Clivio, T. Knöös, G. Nicolini and L.

- Cozzi, "On the dosimetric behaviour of photon dose calculation algorithms in the presence of simple geometric heterogeneities: comparison with Monte Carlo calculations.," *Phys Med Biol*, vol. 52, no. 5, pp. 1363-1385, Mar 2007.
- [20] F. Hasenbalg, H. Neuenschwander, R. Mini and E. J. Born, "Collapsed cone convolution and analytical anisotropic algorithm dose calculations compared to VMC++ Monte Carlo simulations in clinical cases.," *Phys Med Biol*, vol. 52, no. 13, pp. 3679-3691, Jul 2007.
- [21] V. Panettieri, B. Wennberg, G. Gagliardi, M. A. Duch, M. Ginjaume and I. Lax, "SBRT of lung tumours: Monte Carlo simulation with PENELOPE of dose distributions including respiratory motion and comparison with different treatment planning systems.," *Phys Med Biol*, vol. 52, no. 14, pp. 4265-4281, Jul 2007.
- [22] E. Sterpin, M. Tomsej, B. Smedt, N. Reynaert and S. Vynckier, "Monte carlo evaluation of the AAA treatment planning algorithm in a heterogeneous multilayer phantom and IMRT clinical treatments for an Elekta SL25 linear accelerator.," *Med Phys*, vol. 34, no. 5, pp. 1665-1677, May 2007.
- [23] J.C. Chow, M.K. Leung and J. Van Dyk, "Variations of lung density and geometry on inhomogeneity correction algorithms: a Monte Carlo dosimetric evaluation.," *Med Phys*, vol. 36, no. 8, pp. 3619-3630, Aug 2009.
- [24] A. O. Jones and I. J. Das, "Comparison of inhomogeneity correction algorithms in small photon fields.," *Med Phys*, vol. 32, no. 3, pp. 766-776, Mar 2005.
- [25] P. Carrasco, N. Jornet, M. A. Duch, L. Weber, M. Ginjaume, T. Eudaldo, D. Jurado, A. Ruiz and M. Ribas, "Comparison of dose calculation algorithms in phantoms with lung equivalent heterogeneities under conditions of lateral electronic disequilibrium.," *Med Phys*, vol. 31, no. 10, pp. 2899-2911, Oct 2004.
- [26] M. Engelsman, et al., "Impact of simple tissue inhomogeneity correction algorithms on conformal radiotherapy of lung tumours.," *Radiother Oncol*, vol. 60, no. 3, pp.

299-309, Sep 2001.

- [27] T. Knöös, E. Wieslander, L. Cozzi, C. Brink, A. Fogliata, D. Albers, H. Nyström and S. Lassen, "Comparison of dose calculation algorithms for treatment planning in external photon beam therapy for clinical situations.," *Phys Med Biol*, vol. 51, no. 22, pp. 5785-5807, Nov 2006.
- [28] U. Haedinger, T. Krieger, M. Flentje and J. Wulf, "Influence of calculation model on dose distribution in stereotactic radiotherapy for pulmonary targets.," *Int J Radiat Oncol Biol Phys*, vol. 61, no. 1, pp. 239-249, Jan 2005.
- [29] N. Papanikolaou et al., "Tissue Inhomogeneity Corrections for Megavoltage Photon Beams, AAPM Report No 85, Task Group No 65 of the Radiation Therapy Committee of the American Association of Physicists in Medicine," *Med Phys*, 2004.
- [30] C. W. Hurkmans, et al., "Recommendations for implementing stereotactic radiotherapy in peripheral stage IA non-small cell lung cancer: report from the Quality Assurance Working Party of the randomised phase III ROSEL study.," *Radiat Oncol*, vol. 4, p. 1, 2009.
- [31] D. Schuring and C. W. Hurkmans, "Developing and evaluating stereotactic lung RT trials: what we should know about the influence of inhomogeneity corrections on dose.," *Radiat Oncol*, vol. 3, p. 21, 2008.
- [32] N.C. van der Voort van Zyp et al., "Clinical introduction of Monte Carlo treatment planning: a different prescription dose for non-small cell lung cancer according to tumor location and size.," *Radiother Oncol*, vol. 96, no. 1, pp. 55-60, Jul 2010.
- [33] A. F. Bielajew and D. Rogers, "Presta: The parameter reduced electron-step transport algorithm for electron monte carlo transport," *Nuclear Instruments and Methods in Physics Research Section B: Beam Interactions with Materials and Atoms*, vol. 18, no. 1-6, pp. 165-181, 1986.

- [34] X. A. Li, C. Yu and T. Holmes, "A systematic evaluation of air cavity dose perturbation in megavoltage x-ray beams.," *Med Phys*, vol. 27, no. 5, pp. 1011-1017, May 2000.
- [35] E. E. Klein, L. M. Chin, R. K. Rice and B. J. Mijnheer, "The influence of air cavities on interface doses for photon beams.," *Int J Radiat Oncol Biol Phys*, vol. 27, no. 2, pp. 419-427, Sep 1993.
- [36] R. Mohan, C. Chui and L. Lidofsky, "Energy and angular distributions of photons from medical linear accelerators.," *Med Phys*, vol. 12, no. 5, pp. 592-597, 1985.
- [37] R. K. Rice, B. J. Mijnheer and L. M. Chin, "Benchmark measurements for lung dose corrections for X-ray beams.," *Int J Radiat Oncol Biol Phys*, vol. 15, no. 2, pp. 399-409, Aug 1988.
- [38] J. J. Battista and M. B. Sharpe, "True three-dimensional dose computations for megavoltage x-ray therapy: a role for the superposition principle.," *Australas Phys Eng Sci Med*, vol. 15, no. 4, pp. 159-178, Dec 1992.
- [39] K. E. Ekstrand and W. H. Barnes, "Pitfalls in the use of high energy X rays to treat tumors in the lung.," *Int J Radiat Oncol Biol Phys*, vol. 18, no. 1, pp. 249-252, Jan 1990.
- [40] H. Saitoh, T. Fujisaki, R. Sakai and E. Kunieda, "Dose distribution of narrow beam irradiation for small lung tumor.," *Int J Radiat Oncol Biol Phys*, vol. 53, no. 5, pp. 1380-1387, Aug 2002.
- [41] M. F. Tsiakalos, S. Stathakis, G. A. Plataniotis, C. Kappas and K. Theodorou, "Monte Carlo dosimetric evaluation of high energy vs low energy photon beams in low density tissues.," *Radiother Oncol*, vol. 79, no. 1, pp. 131-138, Apr 2006.
- [42] R. Jeraj, P. J. Keall and J. V. Siebers, "The effect of dose calculation accuracy on

- inverse treatment planning.," *Phys Med Biol*, vol. 47, no. 3, pp. 391-407, Feb 2002.
- [43] I. Madani, B. Vanderstraeten, S. Bral, M. Coghe, W. De Gersem, C. De Wagter, H. Thierens and W. De Neve, "Comparison of 6 MV and 18 MV photons for IMRT treatment of lung cancer.," *Radiother Oncol*, vol. 82, no. 1, pp. 63-69, Jan 2007.
- [44] E. Weiss, J. V. Siebers and P. J. Keall, "An analysis of 6-MV versus 18-MV photon energy plans for intensity-modulated radiation therapy (IMRT) of lung cancer.," *Radiother Oncol*, vol. 82, no. 1, pp. 55-62, Jan 2007.
- [45] R. C. Miller, J. A. Bonner and R. W. Kline, "Impact of beam energy and field margin on penumbra at lung tumor-lung parenchyma interfaces.," *Int J Radiat Oncol Biol Phys*, vol. 41, no. 3, pp. 707-713, Jun 1998.
- [46] R. O. Kornelsen and M. E. Young, "Changes in the dose-profile of a 10 MV x-ray beam within and beyond low density material.," *Med Phys*, vol. 9, no. 1, pp. 114-116, 1982.
- [47] W. Yang, M. Lobo, N. Dunlap, P. Read, S. Benedict, K. Sheng and J. Lerner, "SU-E-T-790: The Effect of Pulmonary Emphysema on Lung SBRT Dosimetry," vol. 38, no. 6, pp. 3673-3673, 2011.
- [48] S. J. Mentzer and S. J. Swanson, "Treatment of Patients With Lung Cancer and Severe Emphysema*," *Chest*, vol. 116, no. suppl 3, pp. 477S-479S, 1999.
- [49] D. O. Wilson, J. L. Weissfeld, A. Balkan, J. G. Schragin, C. R. Fuhrman, S. N. Fisher, J. Wilson, J. K. Leader, J. M. Siegfried, S. D. Shapiro and F. C. Scurba, "Association of radiographic emphysema and airflow obstruction with lung cancer.," *Am J Respir Crit Care Med*, vol. 178, no. 7, pp. 738-744, Oct 2008.
- [50] J. P. de Torres, et al., "Assessing the relationship between lung cancer risk and emphysema detected on low-dose CT of the chest.," *Chest*, vol. 132, no. 6, pp. 1932-1938, Dec 2007.

- [51] R. P. Parker, P. A. Hobday and K. J. Cassell, "The direct use of CT numbers in radiotherapy dosage calculations for inhomogeneous media.," *Phys Med Biol*, vol. 24, no. 4, pp. 802-809, Jul 1979.
- [52] D. A. Jaffray, J. H. Siewerdsen, J. W. Wong and A. A. Martinez, "Flat-panel cone-beam computed tomography for image-guided radiation therapy.," *Int J Radiat Oncol Biol Phys*, vol. 53, no. 5, pp. 1337-1349, Aug 2002.
- [53] J. H. Siewerdsen and D. A. Jaffray, "Cone-beam computed tomography with a flat-panel imager: magnitude and effects of x-ray scatter.," *Med Phys*, vol. 28, no. 2, pp. 220-231, Feb 2001.
- [54] K. Y. Seet, et al., "The effects of field-of-view and patient size on CT numbers from cone-beam computed tomography.," *Phys Med Biol*, vol. 54, no. 20, pp. 6251-6262, Oct 2009.
- [55] D.W.O. Rogers, et al., "BEAM: A Monte Carlo code to simulate radiotherapy treatment units.," *Med Phys*, vol. 22, no. 503, Dec 1995.

Chapter 3

3 Forcing Lateral Electron Disequilibrium to Spare Lung Tissue: A novel technique for stereotactic body radiation therapy of lung cancer

This chapter is adapted from the research article, "Forcing Lateral Electron Disequilibrium to Spare Lung Tissue: A novel technique for stereotactic body radiation therapy of lung cancer", accepted pending revisions, *Physics in Medicine and Biology*, 2013, submitted April 16, by Disher B, Hajdok G, Gaede S, Mulligan M, and Battista JJ.

3.1 Introduction

Non-small-cell lung cancer continues to be a leading cause of cancer related death in North America [1]. The number of lung cancer patients being diagnosed with early staged disease (i.e. stage I or II) has grown due to the increased availability of computed tomography (CT) imaging [2]. For these patients, the preferable treatment option is surgical lung resection. However, comorbidities, such as emphysema and heart disease, can make surgery intolerable [3]. An alternative form of treatment for these patients is conventional radiation therapy [RT] (delivered in 20-30 fractions), where a homogeneous dose is delivered to the target. Unfortunately, this technique results in poor tumour control probabilities (TCP) of 30% to 40% [3], and a five year survival rate of 20% [4]. A recently developed RT technique, known as stereotactic body radiation therapy (SBRT) or stereotactic ablative radiotherapy (SABR), has been shown to improve TCP to greater than 90% and survival rates up to 40% at three years [5]. The SBRT technique uses image guidance [6, 7] to accurately focus multiple, small megavoltage (MV) radiation beams onto a tumour volume, delivering ablative doses (e.g. 54 Gy) in only a few treatment fractions (e.g. 1-5 sessions) [8]. In contrast to conventional RT, SBRT uses steep dose gradients and heterogeneous dose distributions to keep lung toxicity low while delivering ablative levels of dose to the tumour.

Healthy lung tissue can range in density from 0.1 g/cm^3 to 0.4 g/cm^3 [9, 10]. In contrast, for lung cancer patients also afflicted by emphysema [11], lung densities can be lower than 0.1 g/cm^3 [12]. The dose distribution in low density media is affected by two opposing effects: 1) increased primary photon transmission, and 2) amplified secondary electron range. For conditions of charged particle equilibrium, enhanced photon transmission (effect 1) dominates the lung dose distribution, which increases the dose within lung and tumour (compared to a homogeneous water medium) [13]. In contrast, for conditions that disrupt electron equilibrium (effect 2), large reductions of dose within lung and tumour tissues are possible [14, 15, 16, 17, 18]. Lateral electron disequilibrium (LED) also significantly expands the dose penumbra at the field edge, which may result in inadequate target coverage at the field periphery [19, 20].

The effects of LED on lung dose are generally poorly accounted for by commercial dose calculation algorithms, which oversimplify the secondary electron trajectory [16, 21, 17, 22, 23, 24]. For ‘SBRT-like’ treatment conditions in lung tissue, poorly modelled LED dose perturbations may not predict the actual delivered dose distribution [25] [26]. Historically, to avoid the deleterious effects of LED and algorithm deficiencies, previous authors suggested using lower energy photons ($< 10\text{MV}$) and larger “equilibrium” field sizes ($> 5 \times 5 \text{cm}^2$) for RT of lung cancer patients [27, 28, 29, 30, 19, 31, 32].

For radiotherapeutic conditions that disrupt equilibrium ($> 4\text{MV}$ photons, field sizes $< 5 \times 5 \text{cm}^2$, lung density $< 0.4 \text{ g/cm}^3$), the Monte Carlo (MC) technique [33] is the preferred method for determining accurate dose distributions. In contrast to analytical methods [33] [34], MC methods explicitly track electron transport, and have been used to benchmark simpler dose calculation algorithms [16, 24, 35, 36, 37, 21, 22, 17]. Previously, our group used the MC technique to determine the specific combination of radiation therapy parameters that result in LED [14]. In a phantom study, a small tumour ($1 \times 1 \times 1 \text{cm}^3$) was embedded within lung tissue, and irradiated using a single 18 MV ($3 \times 3 \text{cm}^2$) field. Under conditions of severe LED, lung and tumour depth dose were reduced by as much as 80% and 15% (with respect to an all water absorber), respectively. These results imply that LED could be exploited to leverage a therapeutic ratio that

maximizes the dose within the tumour, while controlling healthy lung dose to acceptable levels. Blomquist, et al. were the first to propose that LED could be used to safely increase the dose delivered to lung tumours [38, 39]. They proposed using 50 MV radiation fields (e.g. 2), and a traditional dose fractionation scheme (e.g. 30 fractions). However, such a technique is not clinically viable.

In this work, we propose a novel LED-optimized SBRT (LED-SBRT) treatment method, where specific radiotherapeutic parameters are chosen in order to cause extreme LED. This will be demonstrated with the introduction of a new clinical ‘tool’ described as LED maps. Further, using both a lung phantom and patient MC simulation, it will be shown that LED-SBRT can be used to enhance the steepness of dose gradients, to additionally increase the ablative levels of dose within the tumour, and further reduce the dose in normal lung. The LED-SBRT technique provides an opportunity to optimize the desired tumour dose enhancement and/or lung tissue sparing via manipulation of RT parameters (beam energy and field size) for a given tumour size. With LED-SBRT, there is an opportunity to increase tumour dose. However, this may be perceived as controversial to the community, and a discussion on this topic is provided here-in.

3.2 Methods

3.2.1 Monte Carlo codes and parameters

MC simulations were performed using the DOSXYZnrc user code (National Research Council of Canada, Ottawa, ON). Simulations were run concurrently using a cluster of PC-based 60 independent Intel Xeon central processing units (Intel Corporation, Santa Carla, CA). These systems operated at processing speeds of 2.67 or 3.4 GHz, and had a combined accessible total RAM of 102 GB. For lung phantom simulations, electron and photon transport parameters (i.e. ECUT and PCUT) were set as ECUT = 0.521 MeV, and PCUT = 0.010 MeV. For the lung patient simulation, ECUT was varied between 0.521MeV, 6MeV, or 18MeV energies, and PCUT = 0.010 MeV. For electron energies below ECUT, DOSXYZnrc terminates the history and deposits the electron energy “on the spot” [40]. Setting ECUT to the maximal photon energy will result in all liberated

electrons being absorbed locally or at the site of photon interaction. This is analogous to simulating charged particle equilibrium (CPE), and the calculated dose is unaffected by electron transport. By setting E CUT as low as possible [i.e. 0.521 MeV (including rest mass energy)] the dose is dependent on electron scattering conditions, and CPE or LED maybe observed. Finally, PRESTA II [41] and EXACT algorithms were selected as the electron step and boundary crossing algorithms. DOSXYZnrc was used to perform all dose calculations, and up to 8×10^9 histories were used per simulation to keep statistical noise to less than 2% for dose voxels. The depth-dose profiles displayed in subsequent figures were normalized to the dose at maximum depth (i.e. D_{\max} ; per energy and field size) in water unless specified otherwise.

The suitability of DOSXYZnrc to accurately calculate the dose distribution for conditions of extreme LED has been assessed previously by our group [14]. In brief, a real water-air-water phantom was created at our centre, which was also virtually modelled within the DOSXYZnrc software. We observed better than 2% agreement comparing measurement against MC dose calculation within water regions. Similarly in air regions, where severe LED persists, measurement and calculation agreed within 3%. An analogous MC validation study was performed by Chow, et al., 2009, which produced results comparable to our own [21].

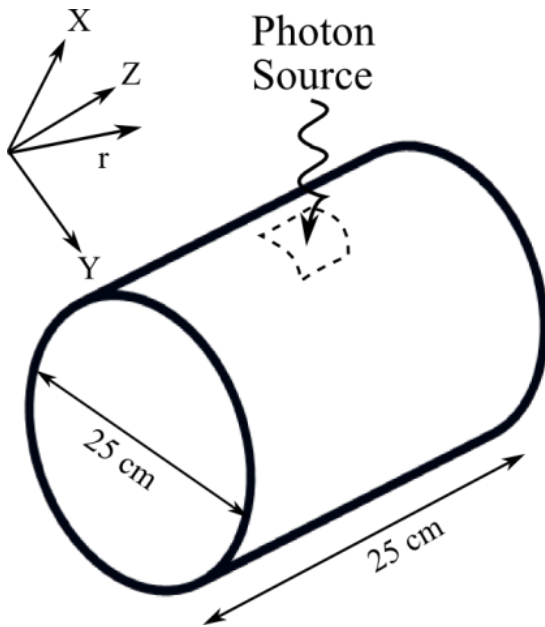
3.2.2 Cylindrical lung phantom simulations

MicroView Analysis+ software V2.2 (GE Healthcare®, Waukesha, WI) was used to create a virtual CT image of a cylindrical lung phantom [see Fig. 3-1 a) and b)]. This phantom was used to demonstrate the potential tumour/lung dose effects of LED-SBRT under the assumptions of homogeneous lung density, and in the absence of lung breathing motion. The height and diameter of the phantom were 25 cm. At the phantom centre, a 1 cm solid water cylindrical tumour (density = 1 g/cm^3) was embedded into an inner cylindrical lung shell (density = 0.25 g/cm^3), which had annuli extending from $r = 0.5$ to 7.5 cm, and a height equal to 25 cm ($z = -12.5 \text{ cm}$ to 12.5 cm). The outer-most “chest wall” shell consisted of water (density = 1 g/cm^3) annuli traversing $r = 7.5 \text{ cm}$ to 12.5 cm

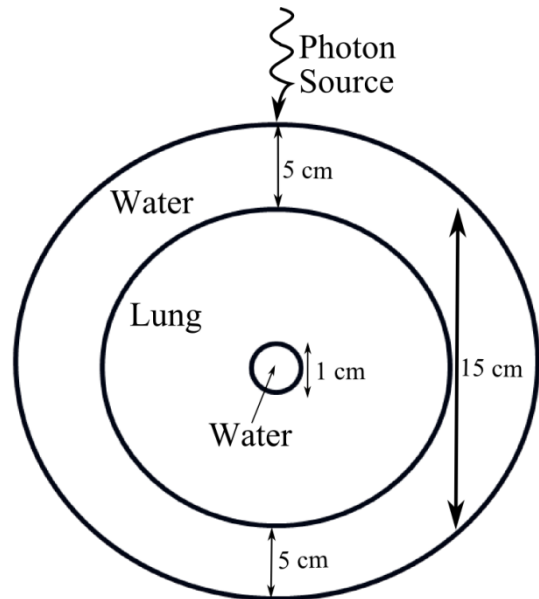
in addition to having a height equal to 25 cm ($z = -12.5\text{cm}$ to 12.5cm). The CTCREATE module [40] was used to convert the CT image of the phantom into a DOSXYZnrc-compatible form (i.e. an eggsphant file) with $1 \times 1 \times 3 \text{ mm}^3$ sized voxels.

Source type '0' (i.e. parallel rectangular beam) was selected within the input settings, and 6 MV and 18 MV photon spectra [42] were applied. For each energy, square field sizes of $1 \times 1 \text{ cm}^2$, $3 \times 3 \text{ cm}^2$, and $5 \times 5 \text{ cm}^2$ were used to collimate the photon field. To simulate a 180° SBRT arc, a single field dose distribution was calculated at 0° . This dose distribution was then exported into Matlab V. R2012a (The MathWorks Inc., Natick, MA) software where it was rotated and summed incrementally by 1° segments until the total cumulative 180° arc dose was complete. This approach was valid as the phantom is symmetric and homogeneous in composition.

(a) The cylindrical phantom



(b) Transverse view showing the x-y plane intersecting at the tumour ($z = 0$).



(c) Transverse view of the lung patient CT

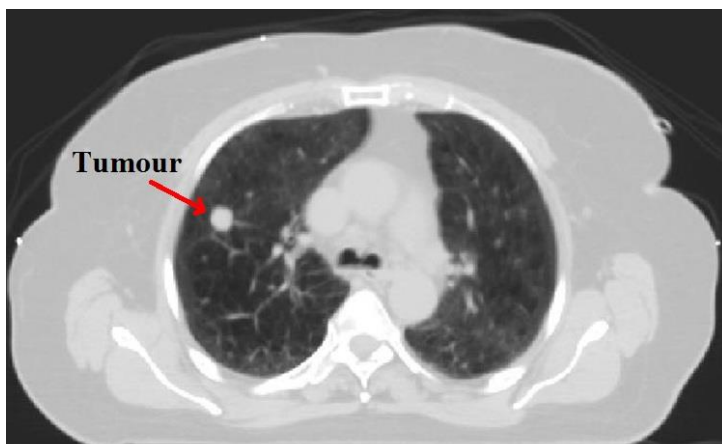


Figure 3-1 (a) shows a schematic diagram (not to scale) of the cylindrical phantom used in this work. Fig. **3-1 (b)** displays the transverse view of the phantom at the tumour center. The tumour was modelled by a small water cylinder with a height and diameter of 1cm. Fig. **3-1 (c)** shows the transverse view of the lung patient including tumour (spherical diameter ~ 1 cm). To demonstrate the lung sparing effect of lateral electron disequilibrium, 6 MV or 18 MV beam energies (various field sizes) were focused onto the tumour center in both phantom and patient Monte Carlo simulations.

3.2.3 Lung patient simulations

A CT image of a SBRT lung cancer patient was acquired using a 16-slice helical CT simulator unit (Brilliance Big Bore CT, Philips Medical Systems, USA). Image acquisition parameters were set to: 120 kVp, 400 mAs/slice, 0.5 sec rotation time, and the pitch varied in accordance with the patient's breathing cycle. CT images were reconstructed at 10 different points within the breathing cycle, and a time-averaged 4-dimensional CT (4DCT) was created for use in this study. The 4DCT image set was reconstructed using a slice thickness of 3 mm, onto a 512 x 512 pixel matrix over a field-of-view of 45 cm [see Fig. **3-1 (c)**]. CTCREATE was again used to convert the lung patient CT data to the "egsphant" format with a voxel resolution of approximately equal to $1 \times 1 \times 3 \text{ mm}^3$.

As the lung cancer patient was originally treated with the SBRT technique at our centre, lung and tumour contours were generated by a radiation oncologist. The patient's lung tumour was spherically shaped with a diameter of ~ 1 cm. Ten separate gross tumour volume (GTV) contours were created to encompass the extent of the tumour motion for each phase of the patient's breathing cycle (tumour motion occurred primarily along the superior-inferior direction). The internal gross tumour volume (IGTV) was created by taking the union of each GTV in 3-dimensions over the entire breathing cycle. The planning target volume (PTV) included the IGTV plus a 5mm isotropic expansion to account for treatment uncertainties (i.e. patient setup). The PTV was ovoid shaped with a length of ~ 3 cm along the superior-to-inferior direction, and a diameter of ~ 1.5 cm in the transverse plane. As well, a healthy lung volume was determined by considering the patient's entire lung volume less the IGTV. Dose calculations were performed within DOSXYZnrc by aiming either 6 MV or 18 MV photon beams [42] onto the patient's tumour centre. Source type '1' was selected within the input settings for the patient MC simulations. This allowed for angular rotation of the photon source about the patient's superior-inferior axis. The field size was chosen to be as small as possible while still providing adequate longitudinal coverage to the PTV. Variations in field size were therefore only possible along the transverse axis.

Since LED is more prevalent at higher beam energies we varied the square field size for the 18 MV energy only (3×3 cm², 3×2.5 cm², 3×2 cm², and 3×1 cm²). Clinical SBRT lung recommendations [Radiation Therapy Oncology Group (RTOG) trials 0236, 0618, 1021, 0813, and 0915] suggest using beam energies less than 10MV. Thus, the 6 MV (3×3 cm²) simulation was selected to represent the clinical control for comparison. For each combination of beam energy and field size, 36 equally spaced and weighted fields were used to span a range of 360° to simulate an SBRT arc treatment. All arc dose distributions were normalized such that 95% or more of the PTV received at least 54Gy (i.e. the D95 dose prescription requirement). Finally, the normalized dose distributions, contours, and CT data were analyzed using the Computational Environment for Radiotherapy Research (CERR) software run within Matlab. [43]

3.2.4 Lateral electron disequilibrium maps

An excellent review of the relevant physics involving MV photons and low density media has been provided by The American Associate of Physicists in Medicine (AAPM) Report Number 85[32]. In short, energy deposition in human tissues (due to impinging photon fluence) can be broken into two sequential components: 1) photon interactions that impart kinetic energy to electrons, and 2) electrons depositing energy locally through ionization and excitation events along their path. From step 1), we define KERMA as the kinetic energy released to electrons per unit mass; from step 2), $KERMA_C$ is the kinetic energy released and absorbed locally along electron paths per unit mass ($KERMA_C$ is equal to KERMA less radiative Bremsstrahlung events). Charged particle equilibrium (CPE) exists when there is a balance between the electron energy fluence entering and leaving a small volume of interest. For CPE conditions, the absorbed dose (D) is equal to $KERMA_C$ (K_c):

$$D = K_C \quad (3.1)$$

However, true CPE is impossible in a clinical radiotherapy beam because photon beam divergence and attenuation perturb the “steady state” flux of electrons [44]. Conversely, transient charged particle equilibrium (TCPE) is achievable along the central-axis of a field of radiation, so long as the depth exceeds the maximum forward electron range, and the field radius surpasses the lateral electron range (establishing lateral electron equilibrium). Under TCPE the dose scales proportionally to $KERMA_C$ such that their ratio is always greater than unity at depths greater than D_{max} :

$$\frac{D}{K_C} > 1 \quad (3.2)$$

The primary goal of this paper was to select appropriate radiotherapeutic parameters that force lateral electron disequilibrium within lung tissue such that the ratio in equation (3.2) is advantageously less than unity:

$$\frac{D}{K_C} < 1 \quad (3.3)$$

As such, it may be possible to spare lung tissue from the effects of radiation exposure along beam path directions. Finally, by considering D/K_C , we can determine how electron trajectories affect the overall dose distribution and have an index of disequilibrium. Visualizations of this ratio can provide a map of lateral electron disequilibrium.

3.3 Results

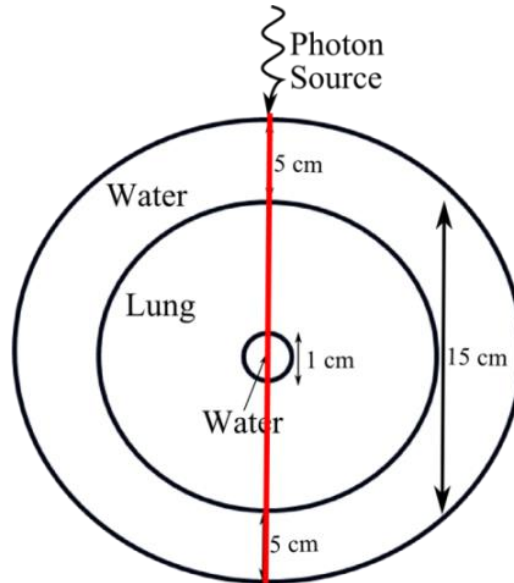
3.3.1 Cylindrical Lung Phantom Simulations

Figure 3-2 (a) displays a transverse slice of the cylindrical lung phantom at the tumour centre. The red line depicts where single field dose profiles were extracted. Fig. 3-2 (b) shows the central-axis depth-dose profile for a 6 MV beam energy collimated to $1 \times 1 \text{ cm}^2$, $3 \times 3 \text{ cm}^2$ or $5 \times 5 \text{ cm}^2$ field sizes. For the 6 MV ($5 \times 5 \text{ cm}^2$) profile, the dose within the downstream lung, tumour and water shell was maintained due to reduced photon attenuation through the low density lung tissue. On the contrary, the 6 MV ($3 \times 3 \text{ cm}^2$) and 6 MV ($1 \times 1 \text{ cm}^2$) dose profiles both showed reduced dose levels within the lung shell as equilibrium was lost for this selection of RT parameters. As a general rule, the lateral path-length of free electrons is approximately $1/3$ to $1/2$ the longitudinal electron range [18]. In water, for a 6 MV photon source ($D_{\text{max}} = 1.5 \text{ cm}$), the lateral range of electrons was between 0.5 cm and 0.75 cm. However, since the electron path-length scales inversely with density, the lateral range increased from 2 cm up to 3 cm in lung tissue. As such, the lateral electron trajectory could reach the lateral beam radius (1.5 cm). These electrons scattered beyond the field edge, were not replaced, which reduced the central-axis depth-dose profile within lung tissues [18, 21, 32]. Also note that LED was more severe using the $1 \times 1 \text{ cm}^2$ field size, which produced the lowest dose levels within lung tissue. Despite the ‘build-down’ of dose within lung tissues, there was still a ‘build-up’ of dose within the tumour.

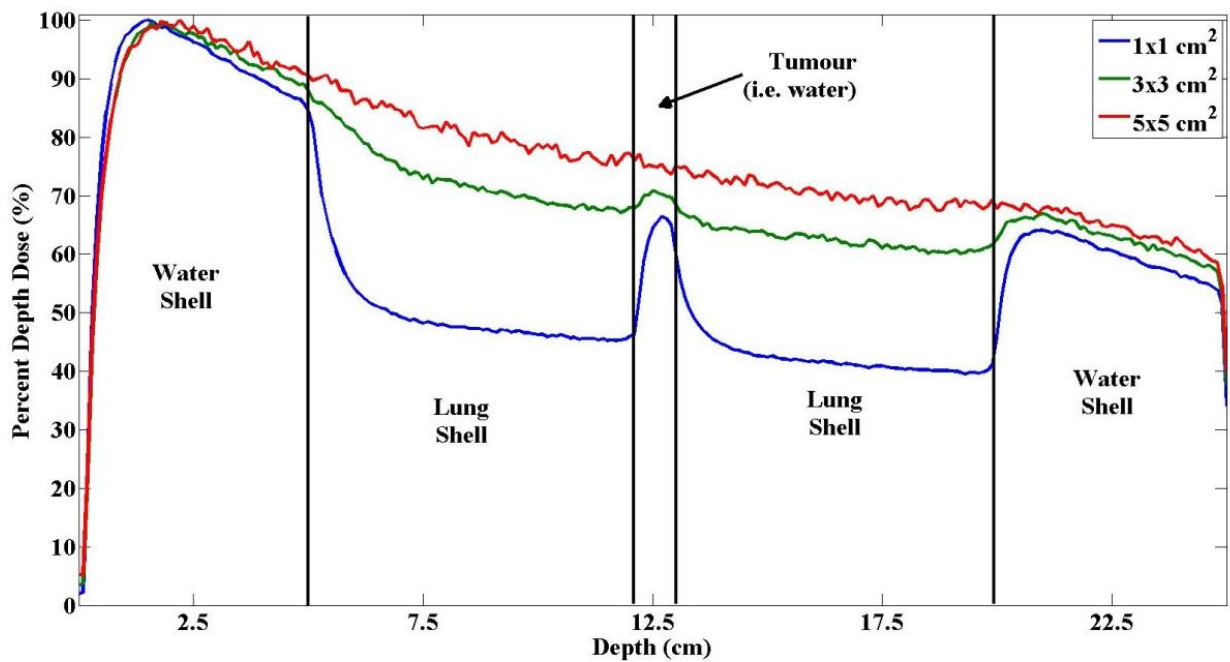
Figure 3-2 (c) shows comparable results for the 18 MV beam. Also notice that D_{max} appeared to be slightly more shallow for the 18 MV ($1 \times 1 \text{ cm}^2$) result in comparison to the other profiles. As the field size was decreased below the lateral electron range in water, Compton electrons liberated from the field periphery no longer reach the central-

axis at depths below the site of photon interaction, which shifted D_{\max} back toward the phantom surface [45].

(a) A transverse view of the phantom (at the tumour center) displaying the location of the depth dose profile (i.e. the red line), and the single field of radiation.



(b) Single field depth-dose profiles acquired from 6 MV simulations.



(c) Single field depth-dose profiles acquired from 18 MV simulations.

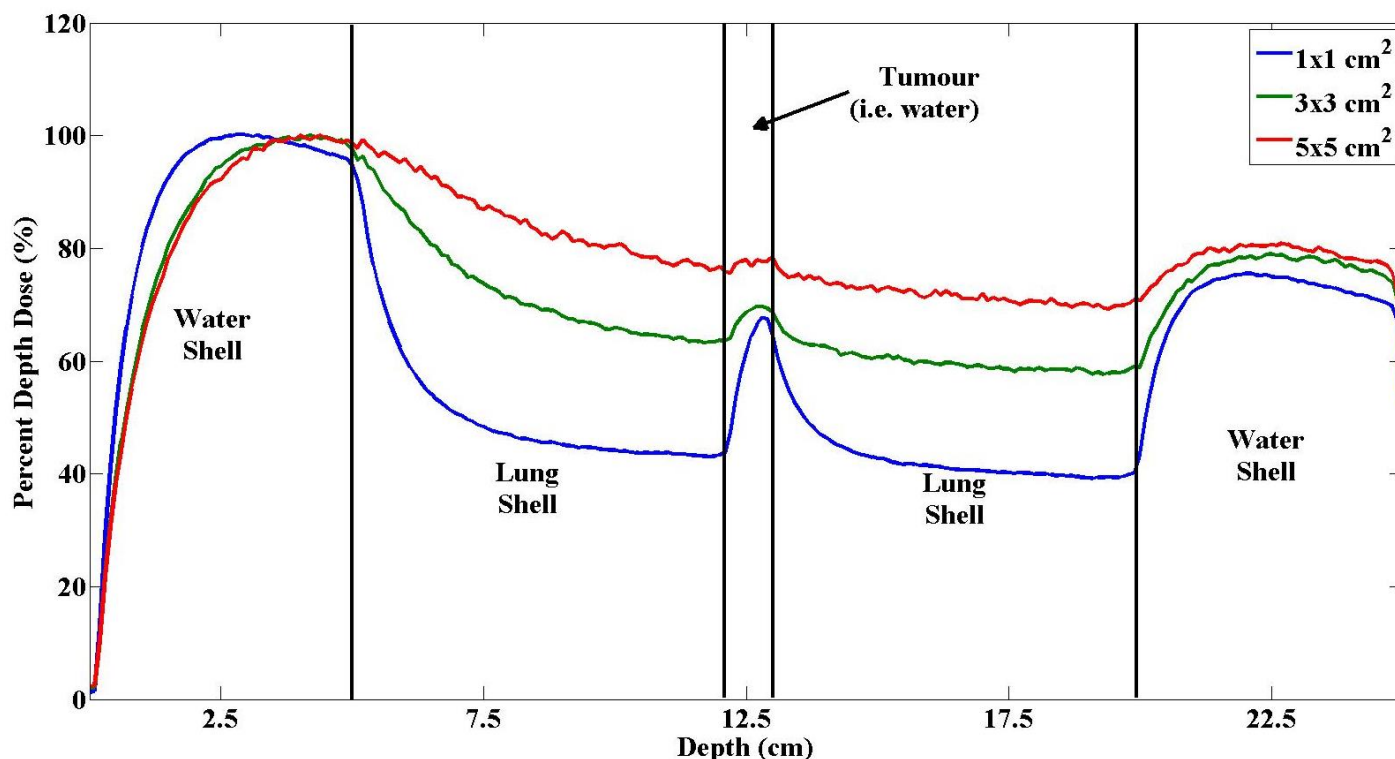
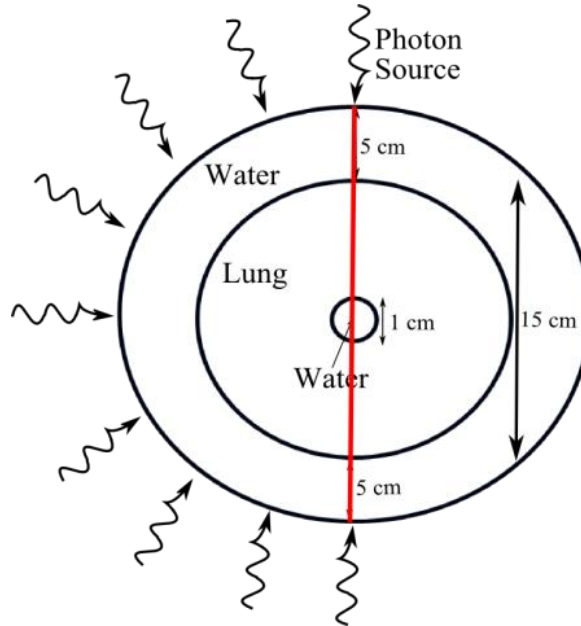


Figure 3-2 (a) shows a transverse view of the cylindrical phantom (at the tumour center) including the line profile where single field depth-dose profiles were acquired for a 6 MV [**Fig. 3-2 (b)**] and 18 MV [**Fig. 3-2 (c)**] beam energy. Note that lateral electron disequilibrium is more dominant at higher beam energies and smaller field sizes.

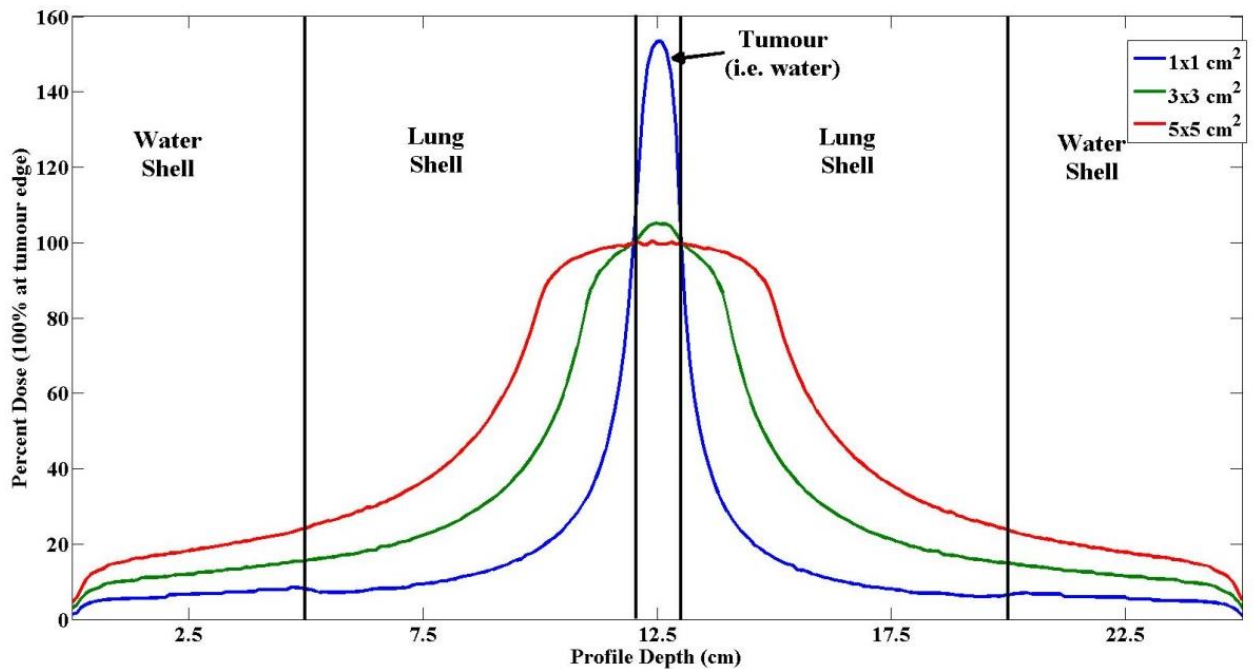
Figure 3-3 (a) displays a transverse slice of the cylindrical lung phantom at the tumour centre. The red line depicts where 180° arc dose profiles were extracted. **Figs. 3-3 (b)** and **(c)** display arc depth-dose profiles for 6 MV and 18 MV beam energies for various field sizes (1x1 cm², 3x3 cm² or 5x5 cm²). Results were normalized such that 100% depth dose falls on the tumour edge. In this way, changes in lung and tumour dose can be better visualized for equal dose coverage of the tumour. In both figures, shrinking the field size exaggerated LED, which greatly spared the lung tissue. For example, in **Fig. 3-3 (c)**, the lung dose at depth = 10.5 cm decreased from 92% to 62% or 23% for the 5x5 cm², 3x3 cm² or 1x1 cm² fields (18 MV energy). In both **Figs. 3-3 (b)** and **(c)**, despite reduced lung dose levels, the maximal tumour dose was greater than 125% for the 1x1

cm^2 field size (6 and 18 MV energy). These dosimetric effects are due to the enhanced dose gradients present at the lung/tumour interface, which occur when LED is severe.

(a) A transverse view of the phantom (at the tumour center) displaying the location of the depth-dose profile (i.e. the red line), and the 180° arc of radiation.



(b) 180° arc depth-dose profiles acquired from 6 MV simulations.



(c) 180° arc-depth dose profiles acquired from 18 MV simulations.

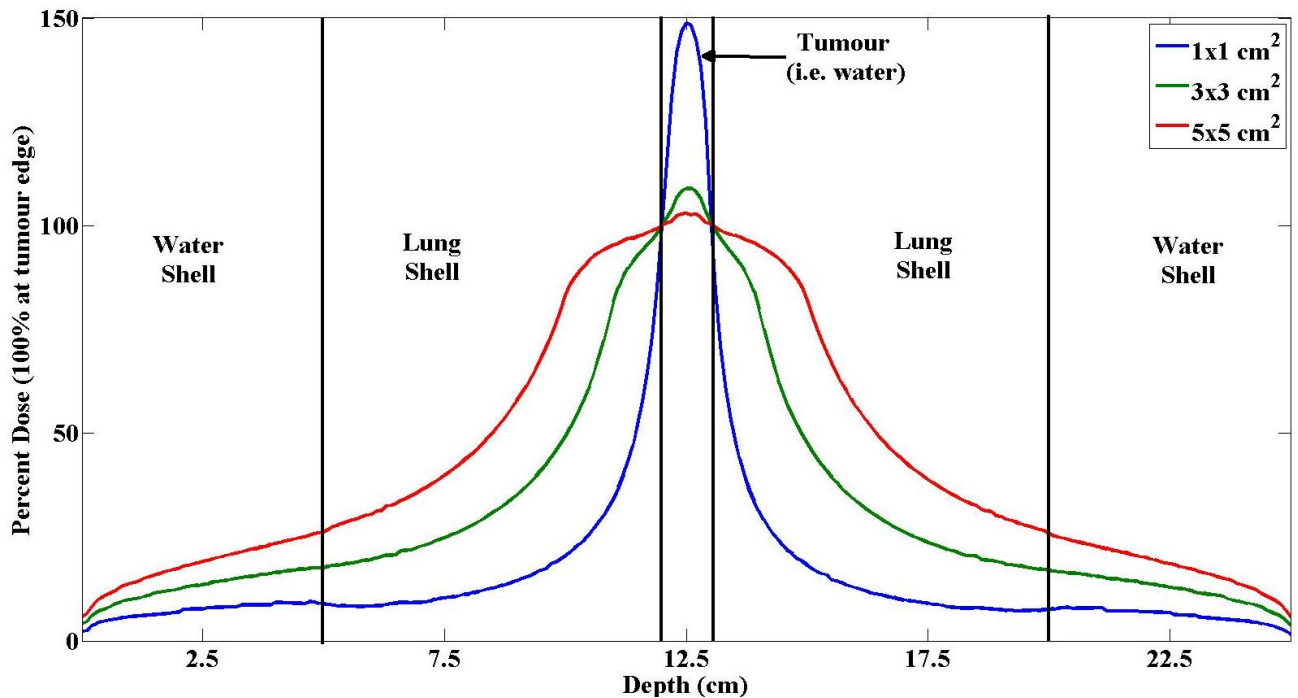


Figure 3-3 (a) shows a transverse view of the cylindrical phantom (at the tumour center) including the line profile where arc depth dose profiles were acquired for 6 MV [**Fig. 3-3 (b)**] and 18 MV [**Fig. 3-3 (c)**] beam energies. Note that lateral electron disequilibrium, established for 18 MV ($1 \times 1 \text{ cm}^2$) energies, reduced lung dose by as much as 70%.

3.3.2 Lung patient simulations

Figure 3-4 (a) shows a transverse view of a lung patient at the tumour centre. The red line indicates where arc depth-dose comparisons were made in **Fig. 3-4 (d)**. **Figs. 3-4 (b)** and **(c)** display the clinical standard [6 MV ($3 \times 3 \text{ cm}^2$)] and LED-optimized [18 MV ($3 \times 1 \text{ cm}^2$)] 360° arc dose distributions overlaid on the lung patient anatomy. Comparing **Fig. 3-4 (b)** to **(c)**, the reduction in field size along the transverse plane is easily visualized. Further, the high dose and steep dose gradient regions are better confined to the vicinity

of tumour in Fig 3-4 (c). Also notice the low to medium dose region within the right lung (light green and yellow colours) that encompasses a smaller area in Fig. 3-4 (c). Figure 3-4 (d) compares the 6 MV (3x3 cm²) arc to the various sized arcs at 18 MV energy. The magnitude of lung sparing and tumour dose increase was related to the extent of LED. For example, the lung dose at depth = 12 cm was 22 Gy, 24 Gy, 26 Gy, and 29 Gy for the 18 MV 3x1 cm², 3x2 cm², 3x2.5 cm², or 3x3 cm² compared to 28 Gy for the 6 MV (3x3 cm²) plan. The greatest lung sparing occurred using the highest energy beam collimated to the smallest field size. Also, tumour dose was increased to a greater extent for arc plans where LED was more severe. Table 3-1 displays the maximal, mean, and minimum dose metrics for the PTV across the various arc plans. For example, comparing the LED-optimized plan [18 MV (3x1 cm²)] to the conventional arc [6 MV (3x3 cm²)], the maximal, mean, and minimal dose were increased by 80 Gy, 11 Gy, and 3 Gy, respectively. These results indicate that LED can be exploited to create steep dose gradients, which increase and localize high dose levels within the PTV, while maintaining or improving the peripheral lung dose.

Table 3-1 compares the mean, maximum, and minimum dose values within the planning target volume (PTV) for the various arc plans. The LED-optimized plan [18 MV (3x1 cm²)] produced the highest dose values for all three PTV dose metrics.

PTV Dose Metrics	360° Arc Plans				
	6 MV 3x3cm ²	18 MV 3x1cm ²	18 MV 3x2cm ²	18 MV 3x2.5cm ²	18 MV 3x3cm ²
Mean Dose (Gy)	70	81	72	70	70
Max. Dose (Gy)	89	169	105	96	91
Min. Dose (Gy)	44	47	45	44	44

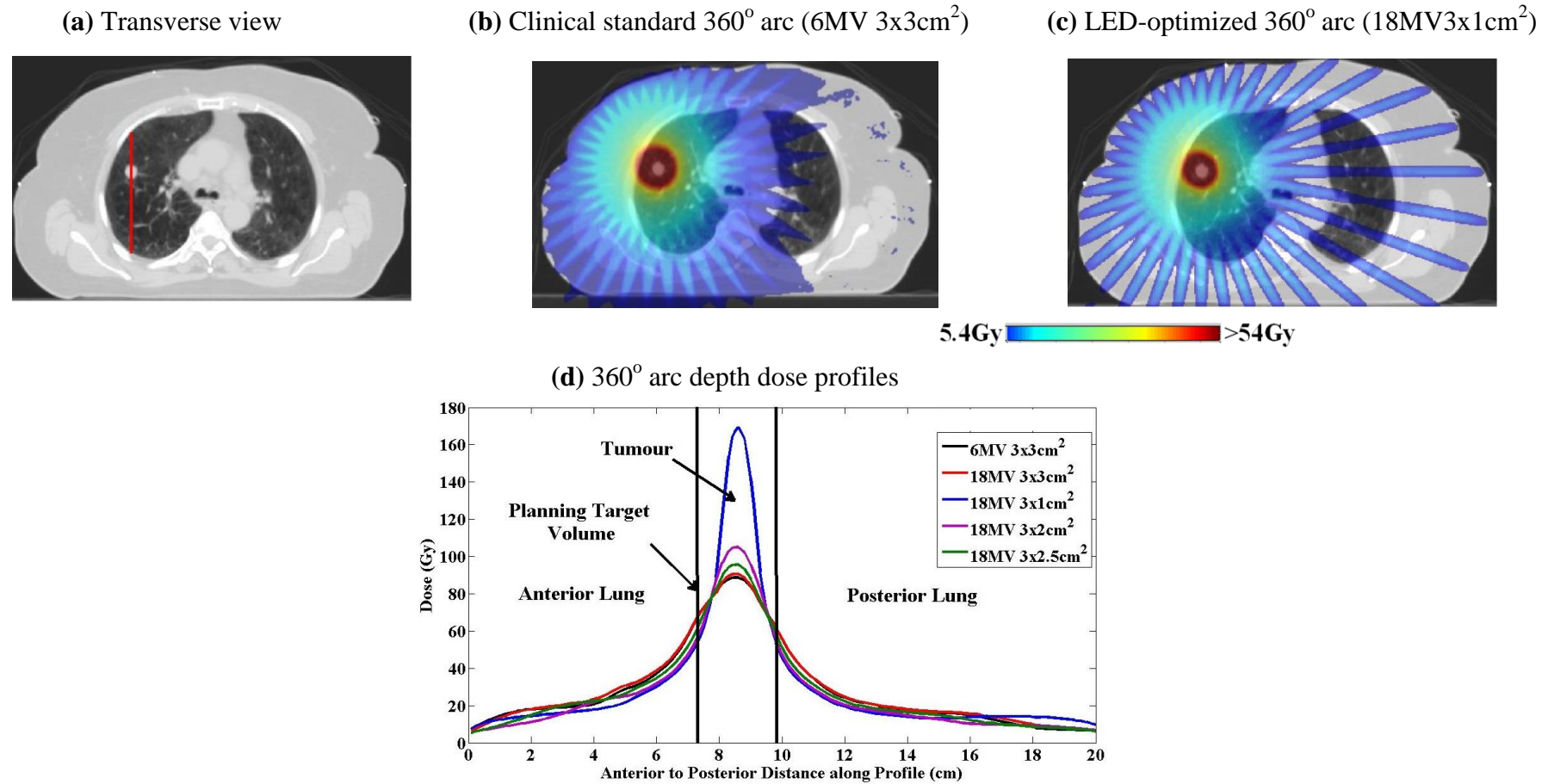


Figure 3-4 (a) shows a transverse view of the lung patient including the line profile where arc depth-dose profiles were acquired. Fig. 3-4 (b) and (c) display a transverse view of the 6 MV (3x3cm²) and 18 MV (3x1cm²) 360° arc dose distributions in the vicinity of the tumour. Fig. 3-4 (d) presents various 360° arc depth-dose profiles. The LED-optimized arc [i.e. 18 MV (3x1cm²)] produced a ‘hot spot’ in the tumour center that was approximately two times the value observed using the clinical standard arc [i.e. 6 MV (3x3cm²)]. Despite increased tumour dose levels, the LED-optimized plan produced the lowest lung dose distribution. Note, the colour bar is relevant to Fig.s 3-4 (b) and (c) only.

Figure **3-5 (a)** shows a coronal view of the lung patient at the tumour centre. The red line indicates where arc depth-dose comparisons were made in Fig. **3-5 (d)**. Figs. **3-5 (b)** and **(c)** display the clinical standard [6 MV ($3 \times 3 \text{ cm}^2$)] and LED-optimized [18 MV ($3 \times 1 \text{ cm}^2$)] 360° arc dose distributions overlaid on the lung patient anatomy. As the PTV's longest axis aligned with the superior-to-inferior direction, it was not possible to reduce the field size in the coronal plane while maintaining adequate PTV coverage. Also, comparing Fig. **3-5 (b)** and **(c)**, the dose penumbra was wider for the LED-optimized plan, an effect due to the increased lateral electron range for higher energy electrons. This is also evident from observing Fig. **3-5 (d)** as the dose profile just beyond the PTV border is the highest for the LED-optimized plan. As in Fig. **3-4 (d)**, the coronal dose profile within the PTV was largest for the 18 MV ($3 \times 1 \text{ cm}^2$) arc, followed by the 18 MV ($3 \times 2 \text{ cm}^2$), 18 MV ($3 \times 2.5 \text{ cm}^2$), 18 MV ($3 \times 3 \text{ cm}^2$), and 6 MV ($3 \times 3 \text{ cm}^2$) plans (see Table **3-1** for specific dose values within the PTV).

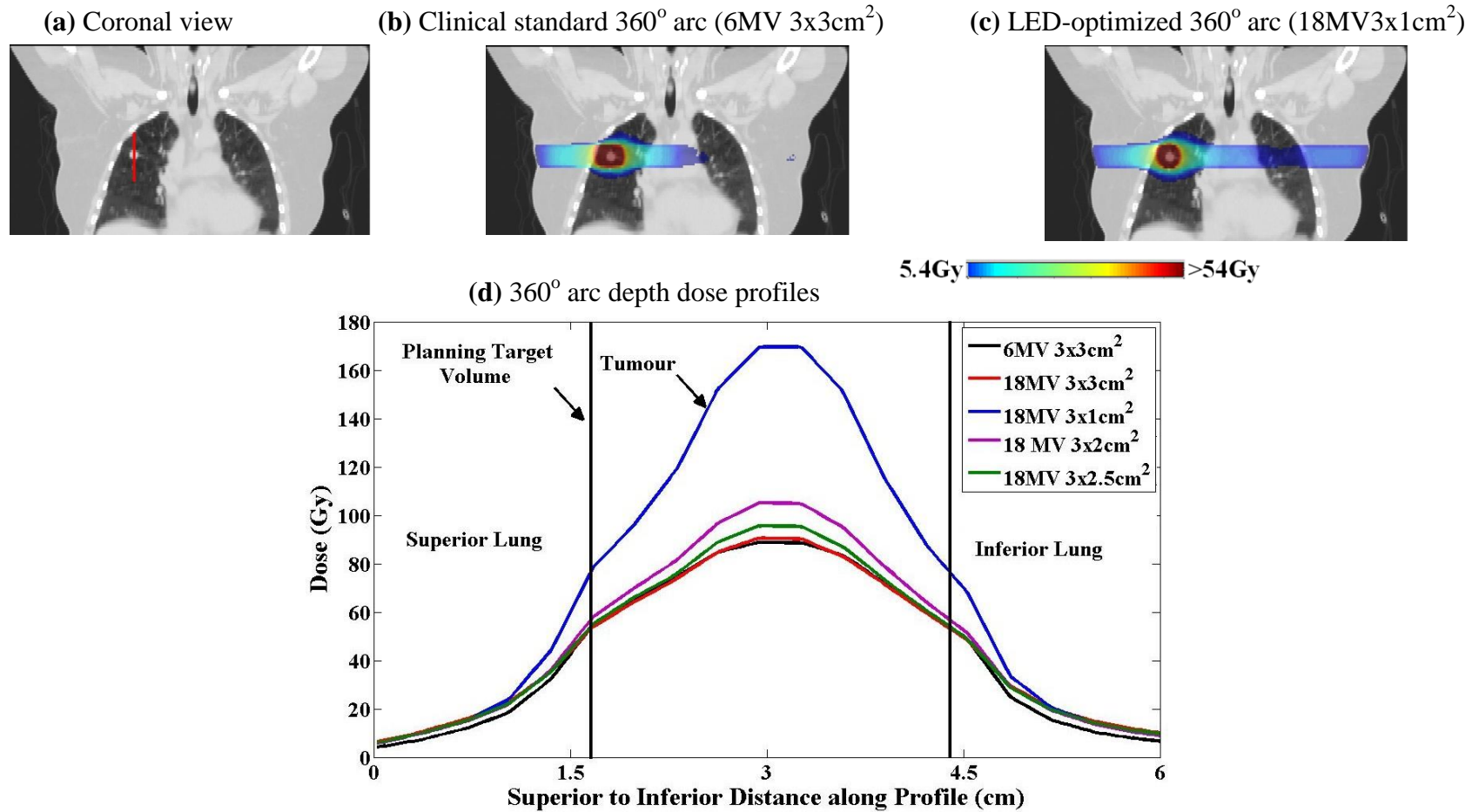


Figure 3-5 (a) shows a coronal view of the lung patient including the line profile where arc depth-dose profiles were acquired. **Figs 3-5 (b) and (c)** display a coronal view of the 6 MV (3x3cm²) and 18 MV (3x1cm²) 360° arc dose distributions in the vicinity of the tumour. Fig. 5 (d) presents various 360° arc depth dose profiles. Comparing the LED-optimized arc [i.e. 18 MV (3x1cm²)] to the clinical standard arc [i.e. 6 MV (3x3cm²)], the planning target volume (PTV) received more dose along the superior-inferior axis. Note, the colour bar is relevant to Figs 3-5 (b) and (c) only.

Figure 3-6 compares the dose volume histograms (DVH) for the PTV for the 18 MV (3x1 cm²), 18 MV (3x2 cm²), 18 MV (3x2.5 cm²), 18 MV (3x3 cm²), and 6 MV (3x3 cm²) arc plans. All plans met the prescription requirement such that 95% or more of the PTV received at least 54 Gy (i.e. D95). However, plans that exploited the LED phenomenon produced a significant ‘hot spot’ within the PTV centre (see maximum dose in Table 3-1).

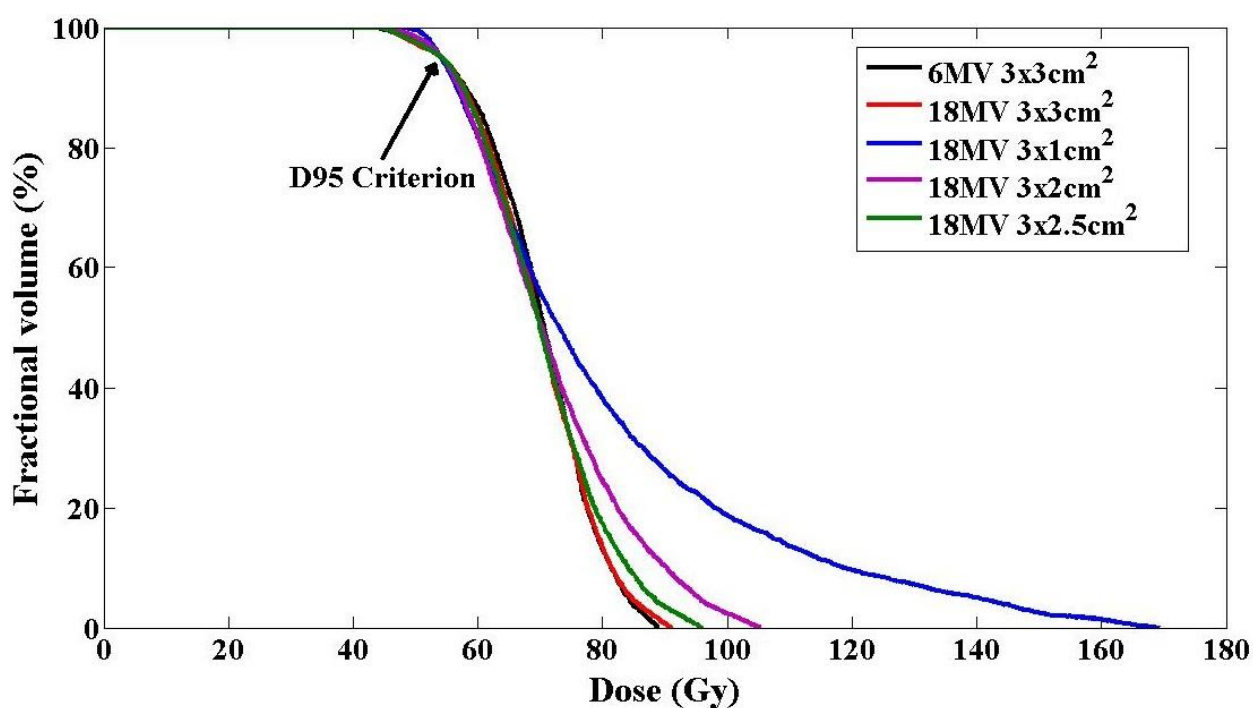


Figure 3-6 displays the dose volume histograms comparing arc dose for the planning target volume (PTV) using either the 6 MV 3x3cm², 18 MV 3x3cm², 18 MV 3x2.5cm², 18 MV 3x2cm², or 18 MV 3x1cm² plans. All plans met the D95 prescription requirement. In addition, the LED-optimized plan (i.e. 18 MV 3x1cm²) produced a ‘hotspot’ of approximately 170Gy at the tumour center (~ 3 times the prescription dose of 54Gy).

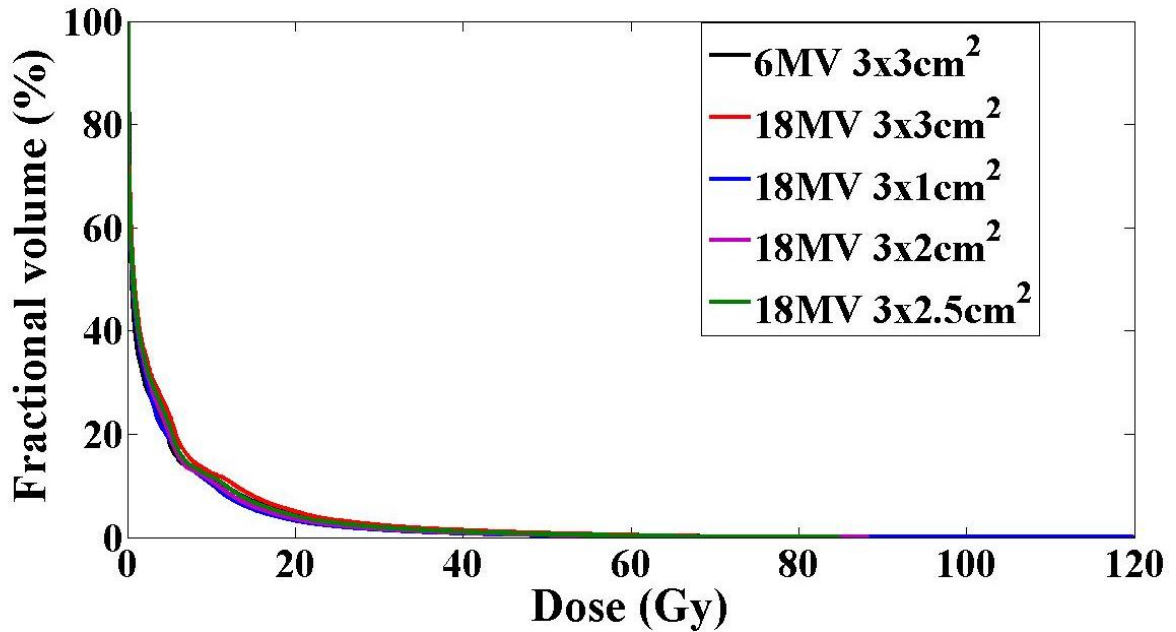
Figure 3-7 displays DVHs with regard to the healthy lung volume and the various arc plans. Upon first inspection of Fig. 3-7 (a), there appeared to be very little difference

between the lung DVHs across all plans. However, Fig. 3-7 (b) shows an expanded view of the DVHs, and in general, the lung DVHs increase in order starting from the 18 MV (3x1 cm²) plan, up to 18 MV (3x2 cm²), 18 MV (3x2.5 cm²), 6 MV (3x3 cm²), and 18 MV (3x3 cm²) plans. Note there were some deviations away from this trend in the vicinity of the V5 region where the 6 MV (3x3 cm²) and 18 MV (3x1 cm²) arcs were comparable, but lower than for the remaining plans. The specific variations in the V5, V20, and mean lung dose are provided in Table 3-2. Of noticeable importance is the sensitivity of these lung dose metrics to changes in the radiotherapeutic parameters. For example, by increasing the 18 MV transverse field size from 1 cm to 3 cm, we observed changes in the mean lung dose, V20, and V5 of 0.8 Gy, 1.8%, and 6%, respectively. Finally, comparing the lung dose metrics of the LED-optimized arc [18 MV (3x1 cm²)] to our clinical standard [6 MV (3x3 cm²)], the V20 and mean lung dose were lower while the V5 remained the same. Indeed, careful attention must be paid to these parameters if we are to improve or maintain the normal lung dose distribution, while intentionally manipulating the extent of LED.

Lung Metrics	360° Arc Plans				
	6 MV 3x3cm ²	18 MV 3x1cm ²	18 MV 3x2cm ²	18 MV 3x2.5cm ²	18 MV 3x3cm ²
Mean Dose	3.7Gy	3.4Gy	3.6Gy	3.9Gy	4.2Gy
V20	4.3%	3.2%	3.6%	4.1%	5.0%
V5	18%	18%	20%	22%	24%

Table 3-2 compares three lung dose metrics for the various arc plans. Mean Dose = average dose from the entire volume of healthy lung tissue (lung volume less the internal gross tumour volume). V20 = the percent of the healthy lung volume receiving 20Gy or more. V5 = the percent of the healthy lung volume receiving 5Gy or more. Both the V20 and Mean Dose metrics are lowest for the LED-optimized, 18 MV (3x1 cm²), plan.

(a) Dose volume histogram for healthy lung



(b) Expanded view of dose volume histogram for healthy lung

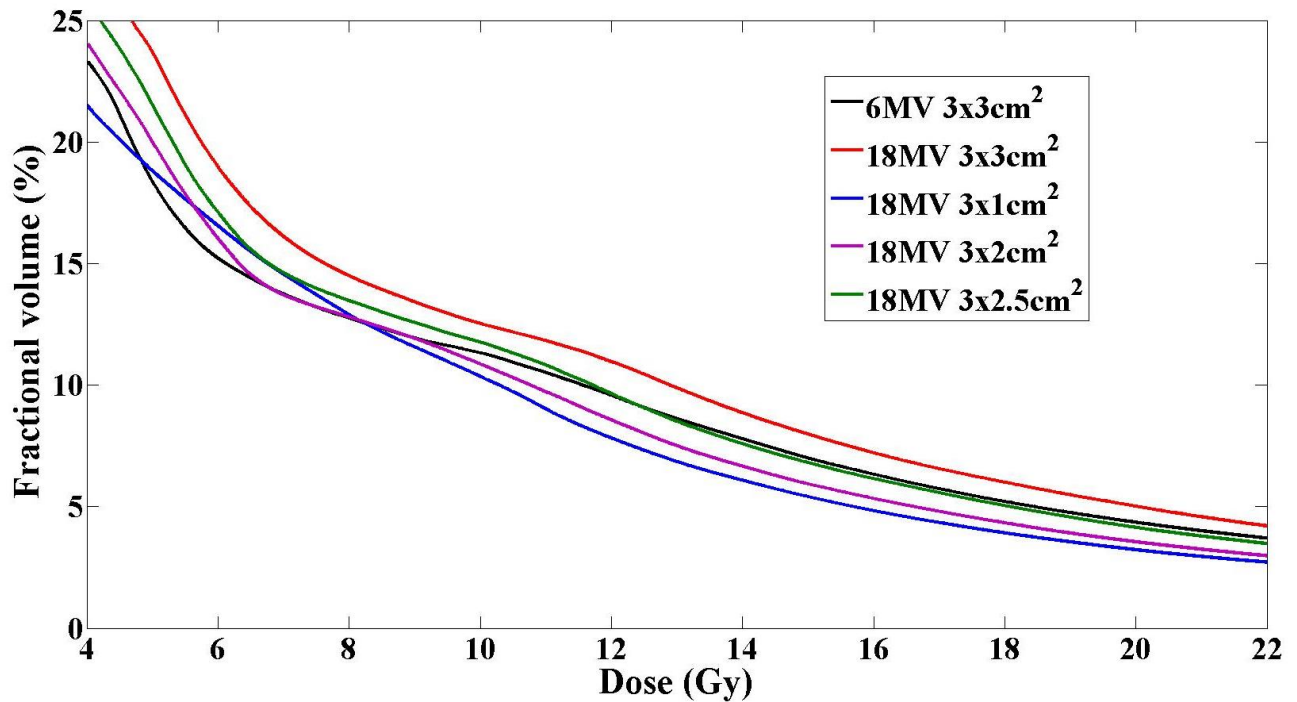


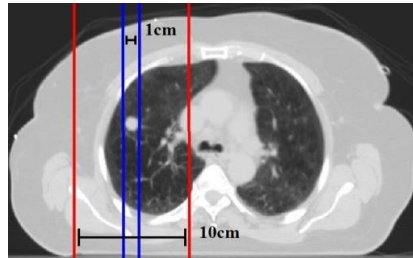
Figure 3-7 (a) displays the dose volume histograms comparing arc dose for the healthy lung volume (lung volume less the internal gross tumour volume) using either the 6 MV 3x3cm², 18 MV 3x3cm², 18 MV 3x2.5cm², 18 MV 3x2cm², or 18 MV 3x1cm² plans. **Fig. 3-7 (b)** displays the same information, but expands on the V5 and V20 regions (i.e. the volume of healthy lung receiving 5Gy or 20Gy or more). Note the lung DVH related to the 18 MV 3x1cm² plan received the least dose in the V20 region. See Table 2 for a comparison of lung dose metrics.

3.3.3 Lateral electron disequilibrium maps

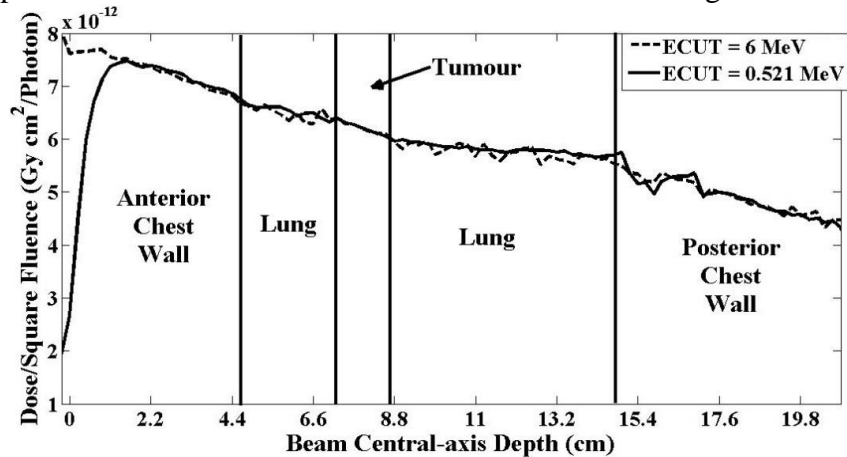
By studying the dose to KERMA ratio we can determine whether the chosen RT parameters (i.e. photon energy, field size, and lung density) combine to promote LED (dose/KERMA < 1). As a demonstration, we focused a single 6 MV (10x10 cm²) field of radiation onto the tumour centre of our test patient, and calculated both the KERMA (ECUT = 6 MeV) and dose (ECUT = 0.521 MeV). We then repeated this process using a single field of radiation utilizing the proposed LED-optimized RT parameters [i.e. 18 MV (3x1cm²)]. Figure 3-8 (a) shows the transverse view of the lung patient with the 6 MV (10x10 cm²) field demarked in red, and the 18 MV (3x1 cm²) field demarked in blue. In Fig. 3-8 (b) the KERMA and dose for the 6 MV (10x10 cm²) field are plotted along the central-axis of the beam. Initially, within the patient's anterior chest wall, the dose is well below the KERMA. However, beyond D_{max} the KERMA and dose values converge. For shallow depths above D_{max}, longitudinal electron disequilibrium exists, which creates the characteristic build-up curve within the anterior chest wall. For depths below D_{max}, the dose is similar to the KERMA within the chest wall, tumour, and lung tissues. Since the 10x10 cm² field size is large enough to establish lateral electron equilibrium, the conditions for TCPE are met, and dose is maintained throughout these tissues.

Figure 3-8 (c) shows a similar comparison using the 18 MV (3x1 cm²) settings. For a 3x1 cm² field size, with the shortest axis aligned along the transverse plane, lateral electron equilibrium was not achievable for water density. Therefore, the dose was less than the KERMA over the entire profile. The largest reductions in the dose profile occurred within lung tissue, as low densities exaggerated LED and enhanced lung sparing. Also, there was an observed dose 'rebuild-up' within the tumour despite the lower lung dose.

(a) Transverse view of lung patient CT with the single field edges demarked (red and blue)



(b) Comparison of KERMA and dose for a 6 MV $10 \times 10 \text{ cm}^2$ single field



(c) Comparison of KERMA and dose for an 18 MV $3 \times 1 \text{ cm}^2$ single field

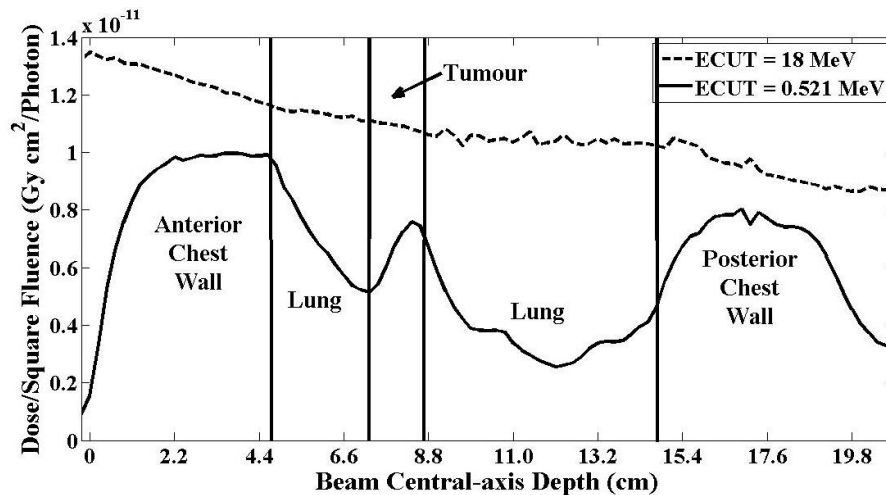


Figure 3-8 (a) shows a transverse view of the lung patient with the 6 MV ($10 \times 10 \text{ cm}^2$) and 18 MV ($3 \times 1 \text{ cm}^2$) field edges demarked in red and blue. **Figs 3-8 (b) and (c)** compare the KERMA (ECUT = 6MeV or 18MeV) to dose (ECUT = 0.521MeV) along the field central-axis. In **Fig. 3-8 (c)**, lateral electron disequilibrium (LED) causes the KERMA and dose profiles to diverge. This effect can be exploited to spare lung tissue for SBRT of lung cancer.

Figures **3-9 (a) – (e)** display a transverse slice of the dose-to-KERMA ratios (or LED maps) for the 6 MV ($3 \times 3 \text{ cm}^2$), 18 MV ($3 \times 3 \text{ cm}^2$), 18 MV ($3 \times 2.5 \text{ cm}^2$), 18 MV ($3 \times 2 \text{ cm}^2$), and 18 MV ($3 \times 1 \text{ cm}^2$) arc plans. For increased beam energy and smaller field sizes, the ratio was reduced below unity (an indicator of LED). On the contrary, for lower energy and larger field sizes, the ratio approached unity. For example, the 18 MV ($3 \times 1 \text{ cm}^2$) LED map contained many lung regions valued from 0.4 to 0.6, while the 6 MV ($3 \times 3 \text{ cm}^2$) map displayed values between 0.6 and 1.0. Figure **3-9 (f)** shows the lateral electron disequilibrium volume histograms (LVH) for the various arc plans. These histograms were created by considering only those lung voxels contained within the beam paths (the entire healthy lung volume was not considered in this analysis). Once again, for the volume of lung tissue traversed by the arcs, the lowest dose to KERMA ratios were observed for those plans with the highest energy and smallest field size [i.e. 18 MV ($3 \times 1 \text{ cm}^2$) or LED-optimized plan]. These findings explain the results shown in Figures **3-4** through **3-7**, and support the hypothesis that the LED phenomenon can be exploited to maintain or lower lung dose, while increasing dose levels within the tumour volume. Finally, the ripple artifact observed between adjacent fields in Figs. **3-9 (a) - (e)**, and discontinuities present within Fig. **3-9 (g)**, are due to an under-sampled arc dose distribution. We expect these artifacts to greatly diminish with the addition of more overlapping fields to complete a full 360° SBRT arc.

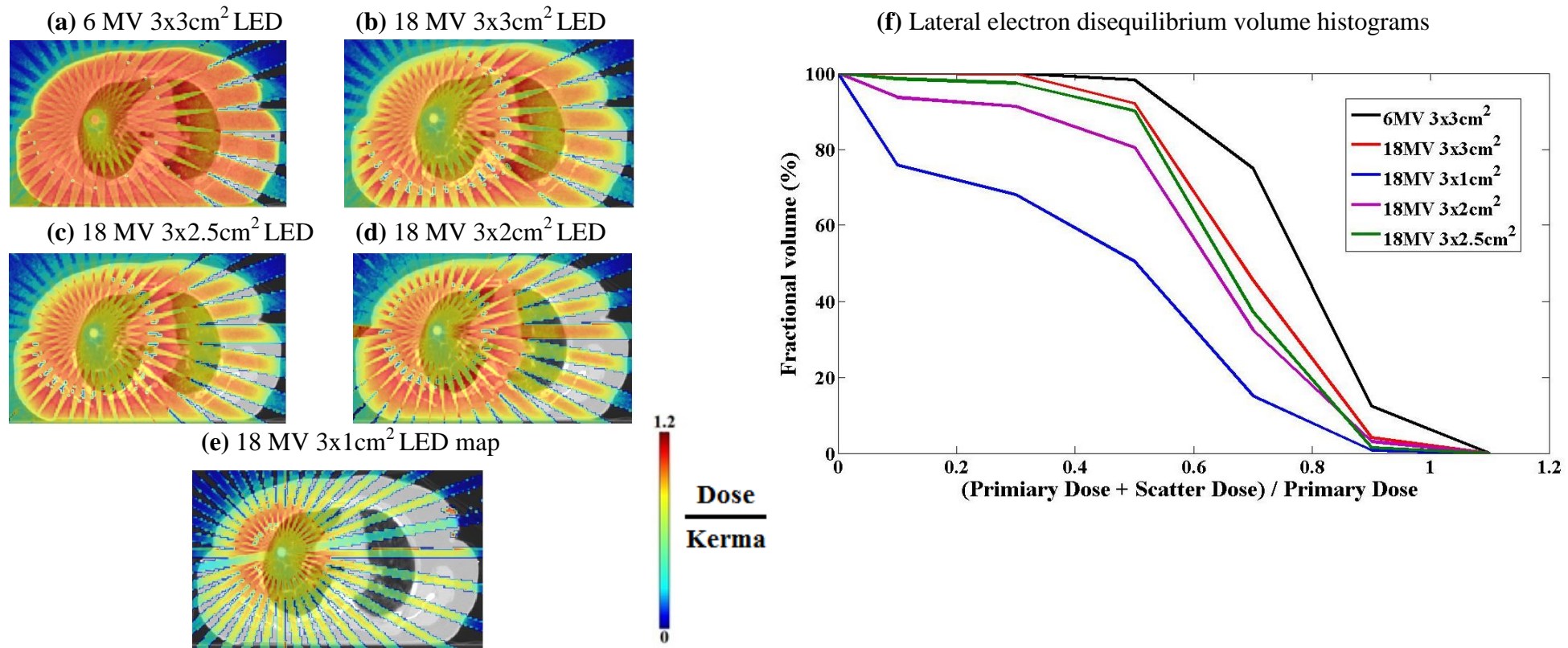


Figure 3-9 (a) – (e) displays the ratio of dose to KERMA, which indicates the severity of lateral electron disequilibrium for each arc plan. As the ratio decreases to zero, LED is more prevalent, which spares lung tissue along beam path directions. **Fig. 3-9** (f) shows lateral electron disequilibrium volume histograms (LVH) acquired from the various arc plans. The LVHs were acquired from the volume of healthy tissue along beam path directions only (not the entire healthy lung volume). The LVH for the 18 MV 3x1cm² demonstrates that LED is most prevalent for this choice of beam energy and field size.

3.4 Discussion

3.4.1 LED-SBRT: potential benefits and controversy

The LED-SBRT technique uses specific combinations of beam energy and field size in order to intentionally disrupt charged particle equilibrium in lung tissue, thus forcing lateral electron disequilibrium. In doing so, an extremely steep dose gradient at the tumour/lung interface occurs, which can be used to increase dose within the tumour, and/or maintain or lower dose in normal lung. The magnitude of the dose gradient spanning these tissues depends on the selected RT and patient parameters (e.g. lung density). Thus, in the planning of LED-SBRT, a physicist must be aware of the dose balance between adjacent tumour and lung tissues, and carefully design treatment in accordance with SBRT protocols [46].

Using LED-SBRT for our sample patient, we were able to increase the minimum, mean, and maximum dose found within the PTV, while maintaining PTV dose coverage and lung dose. The hypothetical benefit of increasing tumour dose for early-stage lung cancer may include: higher tumour control, lower probability of local tumour recurrence, improved radiobiological effects (tumour hypoxia), and hence better overall survival rates. Simultaneously, the benefit associated with a lower lung dose can potentially reduce side-effects, such as radiation pneumonitis and fibrosis. However, the therapeutic benefits associated with LED-SBRT will be limited in clinical practice, depending upon the location of the tumour within lung. For example, in our sample patient, the tumour was surrounded by sufficient lung tissue to force LED. In contrast, tumours located adjacent to chest wall or mediastinum will become difficult to intentionally establish LED, due to surrounding water equivalent material. Nonetheless, under the latter scenario, our technique may still be beneficial if some LED can be produced, thereby creating a steeper dose gradient to spare adjacent critical structures (e.g. ribs, bronchus, trachea, and esophagus).

The idea of further increasing tumour dose using LED-SBRT may seem controversial. Currently, SBRT treatment plans are normalized anywhere between the 60% to 90% isodose lines, which can create hotspots on the order of 111% up to a

maximum of 167% [47]. While other SBRT protocols do not specifically limit the maximum dose within the PTV [25]. In a recent publication, van Baardwijk et al. argued against this SBRT prescription philosophy [48]. They completed a systematic review of radiation doses required to eradicate early-stage lung cancer, where they hypothesized that a lower and more uniform dose to the entire PTV may be sufficient to achieve local tumour control and reduce high-grade toxicity. However, conclusions from their study were focused on centrally located tumours only. In clinical practice, alternative fractionation schedules (e.g. 60 Gy in 8 fractions) are generally used for these tumours to reduce surrounding normal tissue toxicity. Clearly, further investigation is required to determine whether additional increases in SBRT tumour dose will lead to further increases in tumour control (current ablative doses may be sufficient to achieve the desired tumour control probability without tumour overkill).

3.4.2 LED-SBRT and tumour size

In this study, we also varied the size of the tumour from 0.25 cm up to 5 cm within the cylindrical lung phantom. This was done in order to assess the dosimetric effect of tumour size on LED-SBRT derived dose distributions. We classified the tumour size as small (< 1cm), medium (1 to 3 cm), or large (> 3 cm) in accordance with clinical observation of early-staged lung cancers. For small-sized tumours, a minor increase in maximal dose occurred (due to insufficient dose rebuild-up within the tumour) with excellent lung sparing; for medium-sized tumours, increased levels of tumour dose were observed ('hot-spot' > 140%) with reduced normal lung dose; and for large tumours, normal lung dose increased (as larger radiation field sizes limits the extent of LED) with minor enhancements in tumour dose. Thus, we hypothesize that LED-SBRT is best suited for treating tumours no larger in diameter than 3 cm, which is applicable to many patients with early-staged lung cancer (data for variable tumour sizes may be obtained from the authors upon request).

3.4.3 Dose calculation algorithms for use with LED-SBRT

Dose calculation algorithms can be broadly separated into two classes. The first class of algorithms do not consider electron transport, and can greatly overestimate the lung and tumour dose distribution by as much as 20% for RT conditions involving LED [49]. Strictly speaking, class one algorithms should not be used for dose calculation with regard to LED-SBRT.

Unlike class one, class two algorithms model electron transport in an approximate or explicit manner. Clinically accessible algorithms that approximate electron trajectory include: analytical anisotropic algorithm (AAA) [34], collapsed cone convolution (CCC) algorithm [50], and recently developed Acuros XB (AXB) algorithm [51]. The AAA and CCC algorithm has been deemed acceptable for conditions of moderate electron disequilibrium [16, 17, 21, 25] but errors as large as 8% were observed when an 18MV small field was used to irradiate a lung phantom [21, 34]. In comparison to the AAA and CCC algorithms, the AXB algorithm seems to produce more accurate dose calculations within heterogeneous mediums [52, 53, 54, 24, 55]. For example, Han et. al., 2011, showed better than 2% agreement when comparing dose distributions produced by the AXB algorithm and MC simulation for an 18 MV ($2.5 \times 2.5 \text{ cm}^2$) field incident on a heterogeneous phantom [52]. It appears the AXB algorithm may be appropriate for calculation of LED-SBRT dose distributions in lung. However, a future study would be useful to validate this assertion, and test the accuracy of the AXB algorithm under conditions of extreme LED.

Finally, as the Monte Carlo technique explicitly tracks electron range [33], it can accurately predict the dosimetric effects of LED in lung tissue. Recent advances in graphical processing units and parallel computing have made MC VMAT simulations clinically feasible with computation times on the order of seconds [56, 57, 58, 59]. Similar MC techniques have already been adopted clinically [e.g. Cyberknife stereotactic radiosurgery system (Accuray Inc., Sunnyvale, CA) [60]], and will likely be the algorithm of choice for treatment planning of LED-SBRT in the future.

3.4.4 Clinical implementation of LED-SBRT

Our study used 36 equally weighted square or rectangular fields to simulate an SBRT arc technique. This approach was taken in order to understand the basic physical principals that govern the dose distribution within the lung and tumour tissues. In reality, modern day SBRT techniques employ volume modulated arc therapy (VMAT) [7, 61] and/or intensity-modulated radiation therapy (IMRT) [62], which are capable of optimizing the dose distribution with respect to specific constraints. A future study involving a MC modelled, LED optimized, VMAT technique [63] may be useful to further improve the tumour-to-lung dose ratio using inverse optimization techniques.

Beyond dose optimization techniques, the LED phenomenon could be further exploited by gating the SBRT delivery. As the extent of LED is inversely related to lung density, further reductions in lung dose could be gained by delivering the radiation during an *inhale* phase of the breathing cycle (i.e. respiratory gating the radiation treatment). For instance, Hanley, et al., 1999 [64] and Yorke, et al., 2002 [65] have proposed using a deep inspiration breath-hold (DIBH) technique for radiation therapy of lung cancer. Hanley et al., suggest that lung density can be reduced from 0.26 g/cm^3 to 0.19 g/cm^3 using DIBH [64]. Also it was reported that DIBH immobilizes the target, improving tumour localization, and allows for target margin reduction. With LED-SBRT, internal target volume reduction should be pursued (via 4DCT and gating) in order to reduce the tissue heterogeneity of the PTV, and localize high dose levels within the tumour volume.

Unfortunately, gated LED-SBRT will involve longer treatment times, which will be compounded by attempts to increase tumour dose levels. A large dose rate is required in order to deliver a sufficient amount of monitors units through a small field aperture. This may be conceivable using the TrueBeam LINAC in flattening filter free mode where dose rates can be up to four times larger (at certain energies; 6MV or 10MV) than traditional LINAC technology [66]. Before LED-SBRT can be implemented clinically, a future study is required to resolve issues involving: 1) limitations concerning tumour size and location within the thorax, 2) toxicity levels in adjacent healthy tissues (including peripheral tissues that receive a greater neutron dose at a higher energy), 3) gating and

choice of breathing phase, 4) Monte Carlo VMAT optimization, and 5) clinical time constraints given the necessity of high dose rates.

3.5 Conclusion

This article introduces a novel SBRT technique for application to patients with early staged lung cancer. By exploiting the LED phenomenon, we have demonstrated the possibility of increasing tumour dose while maintaining or lowering normal lung dose levels. Future work is required to determine the limitations of LED-SBRT implementation within a clinical environment, and resolve the controversy concerning toxicity of adjacent healthy tissues.

3.6 Acknowledgements:

The authors would like to thank: Professor Jake Van Dyk, Dr. Jeff Chen, Dr. David Palma, Dr. David Holdsworth, and Mr. Michael Jensen for helpful conversation and aid in development of this work. Financial support from the Natural Sciences and Engineering Research Council of Canada (NSERC), and the Canadian Institutes of Health Research (CIHR) are also gratefully acknowledged.

3.7 References:

- [1] R. Siegel, E. Ward, O. Brawley and A. Jemal, "Cancer statistics, 2011: the impact of eliminating socioeconomic and racial disparities on premature cancer deaths.," *CA Cancer J Clin*, vol. 61, no. 4, pp. 212-236, 2011.
- [2] C. I. Henschke and a. et., "Survival of patients with stage I lung cancer detected on CT screening," *N Engl J Med*, vol. 355, pp. 1763-1771, 2006.

- [3] R. Timmerman, R. Paulus, J. Galvin, J. Michalski, W. Straube, J. Bradley, A. Fakiris, A. Bezjak, G. Videtic, D. Johnstone, J. Fowler, E. Gore and H. Choy, "Stereotactic body radiation therapy for inoperable early stage lung cancer.," *JAMA*, vol. 303, no. 11, pp. 1070-1076, Mar 2010.
- [4] J. P. Wisnivesky, M. Bonomi, C. Henschke, M. Iannuzzi and T. McGinn, "Radiation therapy for the treatment of unresected stage I-II non-small cell lung cancer.," *Chest*, vol. 128, no. 3, pp. 1461-1467, Sep 2005.
- [5] J. H. Heinzerling, B. Kavanagh and R. D. Timmerman, "Stereotactic ablative radiation therapy for primary lung tumors.," *Cancer J*, vol. 17, no. 1, pp. 28-32, 2011.
- [6] J. P. Bissonnette, T. G. Purdie, J. A. Higgins, W. Li and A. Bezjak, "Cone-beam computed tomographic image guidance for lung cancer radiation therapy.," *Int J Radiat Oncol Biol Phys*, vol. 73, no. 3, pp. 927-934, Mar 2009.
- [7] K. Otto, "Volumetric modulated arc therapy: IMRT in a single gantry arc," *Medical physics*, vol. 35, p. 310, 2008.
- [8] R. D. Timmerman, B. D. Kavanagh, L. C. Cho, L. Papiez and L. Xing, "Stereotactic body radiation therapy in multiple organ sites.," *J Clin Oncol*, vol. 25, no. 8, pp. 947-952, Mar 2007.
- [9] L. J. Rosenblum, R. A. Mauceri, D. E. Wellenstein, F. D. Thomas, D. A. Bassano, B. N. Raasch, C. C. Chamberlain and E. R. Heitzman, "Density patterns in the normal lung as determined by computed tomography.," *Radiology*, vol. 137, no. 2, pp. 409-416, Nov 1980.
- [10] J. van Dyk, T. J. Keane and W. D. Rider, "Lung density as measured by computerized tomography: implications for radiotherapy.," *Int J Radiat Oncol Biol Phys*, vol. 8, no. 8, pp. 1363-1372, Aug 1982.

- [11] D. O. Wilson, J. L. Weissfeld, A. Balkan, J. G. Schragin, C. R. Fuhrman, S. N. Fisher, J. Wilson, J. K. Leader, J. M. Siegfried, S. D. Shapiro and F. C. Sciurba, "Association of radiographic emphysema and airflow obstruction with lung cancer.," *Am J Respir Crit Care Med*, vol. 178, no. 7, pp. 738-744, Oct 2008.
- [12] G. R. Washko, et al., "Lung Volumes and Emphysema in Smokers with Interstitial Lung Abnormalities," *New England Journal of Medicine*, vol. 364, no. 10, pp. 897-906, 2011.
- [13] E. Yorke, L. Harisiadis, B. Wessels, H. Aghdam and R. Altemus, "Dosimetric considerations in radiation therapy of coin lesions of the lung.," *Int J Radiat Oncol Biol Phys*, vol. 34, no. 2, pp. 481-487, Jan 1996.
- [14] B. Disher, G. Hajdok, S. Gaede and J. J. Battista, "An in-depth Monte Carlo study of lateral electron disequilibrium for small fields in ultra-low density lung: implications for modern radiation therapy.," *Phys Med Biol*, vol. 57, no. 6, pp. 1543-1559, Mar 2012.
- [15] P. E. Metcalfe, T. P. Wong and P. W. Hoban, "Radiotherapy X-ray beam inhomogeneity corrections: the problem of lateral electronic disequilibrium in lung.," *Australas Phys Eng Sci Med*, vol. 16, no. 4, pp. 155-167, Dec 1993.
- [16] L. R. Aarup, et al., "The effect of different lung densities on the accuracy of various radiotherapy dose calculation methods: Implications for tumour coverage," *Radiotherapy and Oncology*, vol. 91, no. 3, pp. 405-414, 2009.
- [17] P. Carrasco, N. Jornet, M. A. Duch, L. Weber, M. Ginjaume, T. Eudaldo, D. Jurado, A. Ruiz and M. Ribas, "Comparison of dose calculation algorithms in phantoms with lung equivalent heterogeneities under conditions of lateral electronic disequilibrium.," *Med Phys*, vol. 31, no. 10, pp. 2899-2911, Oct 2004.
- [18] T. R. Mackie, E. el Khatib, J. Battista, J. Scrimger, J. Van Dyk and J. R.

- Cunningham, "Lung dose corrections for 6- and 15-MV x rays.," *Med Phys*, vol. 12, no. 3, pp. 327-332, 1985.
- [19] K. E. Ekstrand and W. H. Barnes, "Pitfalls in the use of high energy X rays to treat tumors in the lung.," *Int J Radiat Oncol Biol Phys*, vol. 18, no. 1, pp. 249-252, Jan 1990.
- [20] R. O. Kornelsen and M. E. Young, "Changes in the dose-profile of a 10 MV x-ray beam within and beyond low density material.," *Med Phys*, vol. 9, no. 1, pp. 114-116, 1982.
- [21] J. Chow, M. Leung and J. Van Dyk, "Variations of lung density and geometry on inhomogeneity correction algorithms: a Monte Carlo dosimetric evaluation.," *Med Phys*, vol. 36, no. 8, pp. 3619-3630, Aug 2009.
- [22] A. O. Jones and I. J. Das, "Comparison of inhomogeneity correction algorithms in small photon fields.," *Med Phys*, vol. 32, no. 3, pp. 766-776, Mar 2005.
- [23] T. Knöös, E. Wieslander, L. Cozzi, C. Brink, A. Fogliata, D. Albers, H. Nyström and S. Lassen, "Comparison of dose calculation algorithms for treatment planning in external photon beam therapy for clinical situations.," *Phys Med Biol*, vol. 51, no. 22, pp. 5785-5807, Nov 2006.
- [24] A. Fogliata, E. Vanetti, D. Albers, C. Brink, A. Clivio, T. Knöös, G. Nicolini and L. Cozzi, "On the dosimetric behaviour of photon dose calculation algorithms in the presence of simple geometric heterogeneities: comparison with Monte Carlo calculations.," *Phys Med Biol*, vol. 52, no. 5, pp. 1363-1385, Mar 2007.
- [25] D. Schuring and C. W. Hurkmans, "Developing and evaluating stereotactic lung RT trials: what we should know about the influence of inhomogeneity corrections on dose.," *Radiat Oncol*, vol. 3, p. 21, 2008.
- [26] N. C. van der Voort van Zyp, M. S. Hoogeman, S. van de Water, P. C. Levendag, B.

- van der Holt, B. J. M. Heijmen and J. J. Nuyttens, "Clinical introduction of Monte Carlo treatment planning: a different prescription dose for non-small cell lung cancer according to tumor location and size.," *Radiother Oncol*, vol. 96, no. 1, pp. 55-60, Jul 2010.
- [27] I. Madani, B. Vanderstraeten, S. Bral, M. Coghe, W. De Gerse, C. De Wagter, H. Thierens and W. De Neve, "Comparison of 6 MV and 18 MV photons for IMRT treatment of lung cancer.," *Radiother Oncol*, vol. 82, no. 1, pp. 63-69, Jan 2007.
- [28] M. A. Hunt, G. E. Desobry, B. Fowble and L. R. Coia, "Effect of low-density lateral interfaces on soft-tissue doses.," *Int J Radiat Oncol Biol Phys*, vol. 37, no. 2, pp. 475-482, Jan 1997.
- [29] L. Wang, E. Yorke, G. Desobry and C.S. Chui, "Dosimetric advantage of using 6 MV over 15 MV photons in conformal therapy of lung cancer: Monte Carlo studies in patient geometries.," *J Appl Clin Med Phys*, vol. 3, no. 1, pp. 51-59, 2002.
- [30] R. C. Miller, J. A. Bonner and R. W. Kline, "Impact of beam energy and field margin on penumbra at lung tumor-lung parenchyma interfaces.," *Int J Radiat Oncol Biol Phys*, vol. 41, no. 3, pp. 707-713, Jun 1998.
- [31] H. Saitoh, T. Fujisaki, R. Sakai and E. Kunieda, "Dose distribution of narrow beam irradiation for small lung tumor.," *Int J Radiat Oncol Biol Phys*, vol. 53, no. 5, pp. 1380-1387, Aug 2002.
- [32] N. Papanikolaou, J. Battista, A. Boyer, C. Kappas, E. Klein, T. Mackie, M. Sharpe and J. van Dyk, "Tissue inhomogeneity corrections for megavoltage photon beams AAPM Report No 85," *Madison, WI: Medical Physics Publishing*, 2004.
- [33] A. Ahnesjö and M. M. Aspradakis, "Dose calculations for external photon beams in radiotherapy.," *Phys Med Biol*, vol. 44, no. 11, pp. R99--155, Nov 1999.
- [34] L. Tillikainen, H. Helminen, T. Torsti, S. Siljamäki, J. Alakuijala, J. Pyyry and W.

- Ulmer, "A 3D pencil-beam-based superposition algorithm for photon dose calculation in heterogeneous media.," *Phys Med Biol*, vol. 53, no. 14, pp. 3821-3839, Jul 2008.
- [35] F. Hasenbalg, H. Neuenschwander, R. Mini and E. J. Born, "Collapsed cone convolution and analytical anisotropic algorithm dose calculations compared to VMC++ Monte Carlo simulations in clinical cases.," *Phys Med Biol*, vol. 52, no. 13, pp. 3679-3691, Jul 2007.
- [36] V. Panettieri, B. Wennberg, G. Gagliardi, M. A. Duch, M. Ginjaume and I. Lax, "SBRT of lung tumours: Monte Carlo simulation with PENELOPE of dose distributions including respiratory motion and comparison with different treatment planning systems.," *Phys Med Biol*, vol. 52, no. 14, pp. 4265-4281, Jul 2007.
- [37] E. Sterpin, M. Tomsej, B. De Smedt, N. Reynaert and S. Vynckier, "Monte carlo evaluation of the AAA treatment planning algorithm in a heterogeneous multilayer phantom and IMRT clinical treatments for an Elekta SL25 linear accelerator.," *Med Phys*, vol. 34, no. 5, pp. 1665-1677, May 2007.
- [38] M. Blomquist and M. Karlsson, "Measured lung dose correction factors for 50 MV photons.," *Phys Med Biol*, vol. 43, no. 11, pp. 3225-3234, Nov 1998.
- [39] M. Blomquist, J. Li, C.-M. Ma, B. Zackrisson and M. Karlsson, "Comparison between a conventional treatment energy and 50 MV photons for the treatment of lung tumours.," *Phys Med Biol*, vol. 47, no. 6, pp. 889-897, Mar 2002.
- [40] C. Ma, P. Reckwerdt, M. Holmes, D. Rogers and B. Geiser, DOSXYZ users manual, NRC Report, 1995.
- [41] I. Kawrakow, "Accurate condensed history Monte Carlo simulation of electron transport. I. EGSnrc, the new EGS4 version," *Medical physics*, vol. 27, p. 485, 2000.
- [42] R. Mohan, C. Chui and L. Lidofsky, "Energy and angular distributions of photons

- from medical linear accelerators.," *Med Phys*, vol. 12, no. 5, pp. 592-597, 1985.
- [43] J. O. Deasy, A. I. Blanco and V. H. Clark, "CERR: a computational environment for radiotherapy research.," *Med Phys*, vol. 30, no. 5, pp. 979-985, May 2003.
- [44] H. Johns and J. Cunningham, *The Physics of Radiology. Fourth Edition.*, Springfield, Illinois: Charles C. Thomas, 1983.
- [45] K. E. Sixel and E. B. Podgorsak, "Buildup region of high-energy x-ray beams in radiosurgery.," *Med Phys*, vol. 20, no. 3, pp. 761-764, 1993.
- [46] C. W. Hurkmans, et al., "Recommendations for implementing stereotactic radiotherapy in peripheral stage IA non-small cell lung cancer: report from the Quality Assurance Working Party of the randomised phase III ROSEL study.," *Radiat Oncol*, vol. 4, p. 1, 2009.
- [47] R. Timmerman, R. McGarry, C. Yiannoutsos, L. Papiez, K. Tudor, J. DeLuca, M. Ewing, R. Abdulrahman, C. DesRosiers, M. Williams and J. Fletcher, "Excessive toxicity when treating central tumors in a phase II study of stereotactic body radiation therapy for medically inoperable early-stage lung cancer.," *J Clin Oncol*, vol. 24, no. 30, pp. 4833-4839, Oct 2006.
- [48] A. van Baardwijk, W. A. Tomé, W. van Elmpt, S. M. Bentzen, B. Reymen, R. Wanders, R. Houben, M. Ollers, P. Lambin and D. De Ruyscher, "Is high-dose stereotactic body radiotherapy (SBRT) for stage I non-small cell lung cancer (NSCLC) overkill? A systematic review.," *Radiother Oncol*, vol. 105, no. 2, pp. 145-149, Nov 2012.
- [49] M. Engelsman, et al., "Impact of simple tissue inhomogeneity correction algorithms on conformal radiotherapy of lung tumours.," *Radiother Oncol*, vol. 60, no. 3, pp. 299-309, Sep 2001.
- [50] A. Ahnesjö, P. Andreo and A. Brahme, "Calculation and application of point spread

functions for treatment planning with high energy photon beams.," *Acta Oncol*, vol. 26, no. 1, pp. 49-56, 1987.

- [51] O. N. Vassiliev, T. A. Wareing, J. McGhee, G. Failla, M. R. Salehpour and F. Mourtada, "Validation of a new grid-based Boltzmann equation solver for dose calculation in radiotherapy with photon beams.," *Phys Med Biol*, vol. 55, no. 3, pp. 581-598, Feb 2010.
- [52] T. Han, J. K. Mikell, M. Salehpour and F. Mourtada, "Dosimetric comparison of Acuros XB deterministic radiation transport method with Monte Carlo and model-based convolution methods in heterogeneous media.," *Med Phys*, vol. 38, no. 5, pp. 2651-2664, May 2011.
- [53] S. Rana and K. Rogers, "Dosimetric evaluation of Acuros XB dose calculation algorithm with measurements in predicting doses beyond different air gap thickness for smaller and larger field sizes.," *J Med Phys*, vol. 38, no. 1, pp. 9-14, Jan 2013.
- [54] M. Kan, L. Leung, R. So and P. Yu, "Experimental verification of the Acuros XB and AAA dose calculation adjacent to heterogeneous media for IMRT and RapidArc of nasopharyngeal carcinoma.," *Med Phys*, vol. 40, no. 3, p. 031714, Mar 2013.
- [55] T. Han, D. Followill, J. Mikell, R. Repchak, A. Molineu, R. Howell, M. Salehpour and F. Mourtada, "Dosimetric impact of Acuros XB deterministic radiation transport algorithm for heterogeneous dose calculation in lung cancer.," *Med Phys*, vol. 40, no. 5, p. 051710, May 2013.
- [56] X. Jia, X. Gu, J. Sempau, D. Choi, A. Majumdar and S. Jiang, "Development of a GPU-based Monte Carlo dose calculation code for coupled electron--photon transport," *Physics in medicine and biology*, vol. 55, no. 11, p. 3077, 2010.
- [57] X. Jia, X. Gu, Y. J. Graves, M. Folkerts and S. B. Jiang, "GPU-based fast Monte Carlo simulation for radiotherapy dose calculation.," *Phys Med Biol*, vol. 56, no. 22, pp. 7017-7031, Nov 2011.

- [58] X. Jia, J. Schümann, H. Paganetti and S. B. Jiang, "GPU-based fast Monte Carlo dose calculation for proton therapy.," *Phys Med Biol*, vol. 57, no. 23, pp. 7783-7797, Dec 2012.
- [59] W. Chen, D. Kolditz, M. Beister, R. Bohle and W. A. Kalender, "Fast on-site Monte Carlo tool for dose calculations in CT applications.," *Med Phys*, vol. 39, no. 6, pp. 2985-2996, Jun 2012.
- [60] J. Deng, T. Guerrero, C. M. Ma and R. Nath, "Modelling 6 MV photon beams of a stereotactic radiosurgery system for Monte Carlo treatment planning.," *Phys Med Biol*, vol. 49, no. 9, pp. 1689-1704, May 2004.
- [61] E. Chin and K. Otto, "Investigation of a novel algorithm for true 4D-VMAT planning with comparison to tracked, gated and static delivery," *Medical Physics*, vol. 38, p. 2698, 2011.
- [62] G. Videtic, K. Stephans, C. Reddy, S. Gajdos, M. Kolar, E. Clouser, T. Djemil and others, "Intensity-modulated radiotherapy--based stereotactic body radiotherapy for medically inoperable early-stage lung cancer: excellent local control," *International journal of radiation oncology, biology, physics*, vol. 77, no. 2, pp. 344-349, 2010.
- [63] J. Lobo and I. Popescu, "Two new DOSXYZnrc sources for 4D Monte Carlo simulations of continuously variable beam configurations, with applications to RapidArc, VMAT, TomoTherapy and CyberKnife," *Physics in medicine and biology*, vol. 55, no. 16, p. 4431, 2010.
- [64] J. Hanley, M. Debois, D. Mah, G. Mageras, A. Raben, K. Rosenzweig, B. Mychalczak, L. Schwartz, P. Gloegler, W. Lutz and others, "Deep inspiration breath-hold technique for lung tumors: the potential value of target immobilization and reduced lung density in dose escalation," *International Journal of Radiation Oncology* Biology* Physics*, vol. 45, no. 3, pp. 603-611, 1999.

- [65] E. Yorke, L. Wang, K. Rosenzweig, D. Mah, J. Paoli and C. Chui, "Evaluation of deep inspiration breath-hold lung treatment plans with Monte Carlo dose calculation," *International Journal of Radiation Oncology* Biology* Physics*, vol. 53, no. 4, pp. 1058-1070, 2002.
- [66] J. Hrbacek, S. Lang and S. Klöck, "Commissioning of photon beams of a flattening filter-free linear accelerator and the accuracy of beam modeling using an anisotropic analytical algorithm," *International Journal of Radiation Oncology* Biology* Physics*, vol. 80, no. 4, pp. 1228-1237, 2011.

Chapter 4

4 Correction for “artificial” electron disequilibrium due to cone-beam CT density errors: Implications for on-line adaptive stereotactic body radiation therapy of lung

This chapter is adapted from the research article, "Correction for “artificial” electron disequilibrium due to cone-beam CT density errors: Implications for on-line adaptive stereotactic body radiation therapy of lung" published in *Physics in Medicine and Biology*, 2013 Jun 21;58(12):4157-74 by Disher B, Hajdok G, Wang A, Craig J, Gaede S, and Battista JJ.

4.1 Introduction

The clinical workflow for external beam radiation therapy begins by imaging a patient using a helical CT scanner to produce a planning CT image (PCT). The PCT image yields quantitative tissue information in the form of CT numbers (i.e. Hounsfield Units or HU). The PCT number data is imported into a treatment planning system (TPS), where it is converted to tissue electron density through an HU-to-relative electron density (HU-to-RED) calibration curve, and then used to calculate a planning CT dose distribution or matrix (DM_{PCT}). The DM_{PCT} represents an ideal prescribed dose distribution, which is assumed to be reproducible over all treatment fractions. However, daily deformations of patient anatomy and motion of organs, and/or patient set-up variations can lead to perturbations of the intended daily dose distribution. Accumulation of such dose variations over multiple fractions can lead to a total delivered dose that does not match the prescribed dose distribution (i.e. DM_{PCT}).

With the advent of image-guided radiation therapy (IGRT), it may be possible to reduce the propagation of these dosimetric errors. IGRT combines an imaging modality with a radiation treatment unit. For example, the Varian On-Board Imaging (OBI) system integrates the functionality of a kilovoltage CT scanner with a linear accelerator. It can generate cone-beam CT (CBCT) images for volumetric reconstruction of the patient's

“anatomy-of-the-day”. Currently, this technology is used primarily to account for geometric errors in patient setup [1]. CBCT information could also be utilized in a process referred to as dose adaptive radiation therapy (DART), which accounts for tissue deformation through modifications to the delivered dose distribution over the course of fractionated radiation therapy [2].

In general, the DART paradigm can be segmented into five sequential steps (see Fig. 4-1). For each treatment fraction (denoted by i), the first step of the process begins by acquiring an updated CBCT image of patient anatomy. Second, the CBCT number data is imported into a TPS and converted to tissue electron density through a HU-to-RED calibration curve. The TPS is then used to calculate a CBCT image-based dose matrix (i.e. DM_{CBCT}^i), which can be used to generate a dose-based decision metric (e.g. dose volume histogram [DVH], dose difference matrix, tumor control probability, normal tissue complication probability, etc.) to prompt for treatment plan re-optimization. For example, the original treatment planning dose, DM_{PCT} , could be subtracted from DM_{CBCT}^i to generate a dose difference matrix, Δ_i , which represents the dosimetric deviations between the PCT and CBCT image sets. Δ_i could then be compared to an acceptable minimum threshold value (Δ_{TH}). For $\Delta_i > \Delta_{TH}$, dose differences are severe enough to warrant plan re-optimization, which would ideally be carried out on-line using the most up-to-date CBCT data set. Once re-optimized, the i^{th} fraction of radiation is delivered, and the entire process is repeated until the prescribed dose to target is achieved. For $\Delta_i < \Delta_{TH}$, no re-optimization is required, and treatment delivery proceeds with the next fraction of radiation therapy.

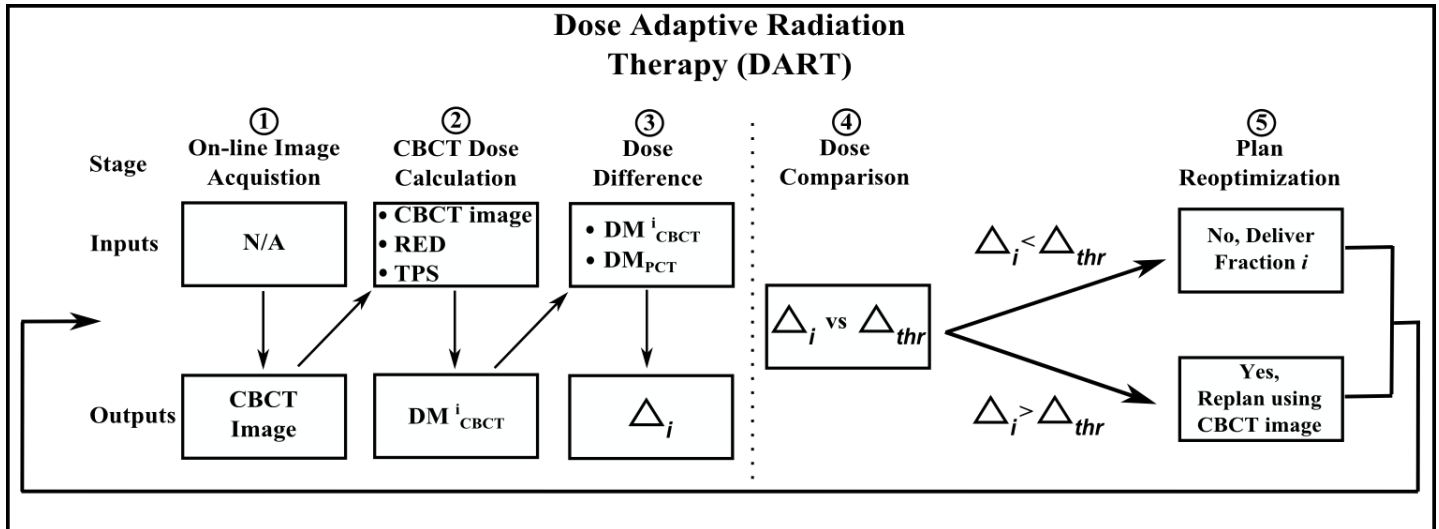


Figure 4-1 the process of dose adaptive radiation therapy (DART). Ideally, CBCT images should be used for online dose calculation, which prompts a decision regarding treatment plan re-optimization to account for variations in patient anatomy or set-up error. Unfortunately, CBCT image artifacts are observed in images of the thorax and can affect decisions regarding DART re-optimization. RED = HU-to-relative electron density conversion curve. TPS = treatment planning system. DM_{PCT} = prescription dose matrix derived from the PCT image set. DM_{CBCT}^i = dose matrix produced from the up-to-date CBCT image preceding the next fraction (i) of radiation treatment. Δ_i = dose difference matrix ($DM_{CBCT}^i - DM_{PCT}$). Δ_{thr} = a selected dose difference threshold upon which dose re-optimization decisions are based.

Ideally, the dose difference, Δ_i , should solely be due to geometric variations in patient anatomy observed between the original PCT and subsequently acquired CBCT images. However, CBCT images are susceptible to artifacts resulting from the cone-beam geometry acquisition, including acceptance of scattered photons [3, 4, 5], spectral beam hardening and filtration [6], temporal lag in data acquisition [7], and potentially respiratory motion [8, 9, 10, 11]. The dosimetric impact of these artifacts has been studied extensively using phantoms and/or patient image data for various treatment sites including: head & neck, pelvis/prostate, lung, and spine [12, 13, 14, 15, 16, 17, 18, 19, 20, 21, 22, 23, 24]. The investigations associated with lung patients revealed CT number reductions of up to 200 HU [14], and dosimetric errors as high as 5%, when comparing PCT and CBCT based plans. Thus, within the context of DART, Δ_i will be both a

function of patient tissue deformation (i.e. $\Delta_{patient}$) and tissue density errors due to CBCT artifacts (i.e. $\Delta_{artifacts}$):

$$\Delta_i = \Delta_{patient} + \Delta_{artifacts} \quad (4.1)$$

Clearly, contributions from $\Delta_{artifacts}$ must be minimized relative to Δ_i because excessive CBCT number inaccuracy may result in 1) ill-founded decisions on the need for plan re-optimization (Fig. 4-1; Step 4), and 2) erroneous prediction of the accumulated *in vivo* dose distribution (Fig. 4-1; Step 5).

The absorbed dose in lung strongly depends on its density. In humans, lung density can vary up to approximately 0.35 g/cm^3 [25]. At these densities, the dose distribution is affected by two factors: 1) reduced photon attenuation, and 2) enhanced secondary electron range. When electron equilibrium is established, factor 1) dominates, and dose is increased to the target within lung and downstream tissues [26]. For conditions of lateral electron disequilibrium (LED), factor 2) dominates, and dose within lung and tumor tissues can be severely reduced [27]. The impact of any small change in density will depend on the state of electron equilibrium. Under equilibrium conditions, several investigators reported that a 5% uncertainty in CT-derived tissue density only produced a 1% deviation in dose calculation [28, 29, 22]. In contrast, under disequilibrium conditions, Disher et al., 2012, showed that a 10% reduction in lung HU (-900 HU to -990 HU) resulted in a 48% reduction in central-axis dose [30].

Therefore, in order to avoid problems associated with LED, accurate dose calculations in lung require high-fidelity CT number data, correct HU-to-RED conversion, and a treatment planning system that can account for electron disequilibrium.

In our investigation, we hypothesize that erroneously low CT numbers from CBCT-based images can cause significant dose errors for dose adaptive stereotactic body radiation therapy (SBRT) of lung tumors. Low CBCT numbers within lung tissue will cause “artificial” electron disequilibrium, which would in turn artificially reduce the calculated dose distribution. In order to demonstrate and quantify the magnitude of artificial LED on dose calculations, we use deformable image registration to warp up-to-date CBCT images

of a lung cancer test patient onto an original PCT (reference) image. As a result, dose differences between PCT and CBCT image-based plans are no longer related to patient tissue deformation ($\Delta_{\text{patient}} = 0$), and are solely due to errors in CBCT-derived lung tissue density that can potentially produce artificial LED:

$$\Delta_i = \Delta_{\text{artificial LED}} \quad (4.2)$$

To highlight the extent of CBCT number differences in patient lung tissue, we first perform CBCT number analysis using an anthropomorphic thorax phantom. In addition, three practical CBCT number correction methods are developed and tested: 1) lung-specific HU-to-RED conversion curves to convert raw CBCT numbers to tissue electron density using calibration methods, 2) substitution of individual CBCT pixel information with bulk CT (BCT) numbers averaged from PCT images for comparable regions (lung, adipose, muscle, and bone), and 3) partial substitution of CBCT pixel information with LED-sensitive CT (LCT) numbers that suppress artificial lateral electron disequilibrium in lung. Finally, we discuss the capability of each technique in improving dose calculation accuracy for adaptive lung SBRT of three sample patients. It should be noted that dose results are influenced by lung tumour location and size, and differences in lung densities between the three patients. Thus, we report on a particular case that best demonstrates the potential dose impacts of electron disequilibrium.

4.2 Materials and Methods

4.2.1 CT phantoms

The Gammex RMI TomoTherapy phantom (Gammex RMI[®], Middleton, WI; referred to as the electron density phantom) is a modified version of the Gammex 467 Electron Density CT Phantom (Gammex RMI[®], Middleton WI). It consists of a 30 cm diameter solid water base with a length of 18 cm. The solid water base contains cylindrical holes that can hold multiple tissue-mimicking inserts, each 3 cm in diameter. The inserts vary in electron density from 0.28 to 1.69 (lung to cortical bone), relative to water.

The RANDO[®] phantom (The Phantom Laboratory, Salem, NY) is an anthropomorphic phantom that represents human male anatomy. Three tissue-simulating materials are used: 1) a soft tissue material (physical density = 0.997 g/cm³), 2) lung material (physical density = 0.352 g/cm³), and 3) adult skeleton (physical density = 1.3 g/cm³). The phantom is constructed into the shape of a typical thorax with an approximate transverse cross-section (20×30 cm²).

4.2.2 CT scanners

CT images of phantoms and lung patients were obtained using a Philips 16-slice helical CT simulator unit (Brilliance Big Bore CT, Philips Inc., Cleveland, OH). The Philips simulator unit was calibrated according to the manufacturer's specifications (Philips, 2006), and operated at the following settings: 120 kVp, 400 mAs/slice, 0.5 s rotation time, and varying pitch based on the patient's breathing cycle. CT images of the lung patients were acquired at 10 different phases of the breathing cycle, and a time-averaged 4D-CT was calculated and designated as the PCT. Images were reconstructed on a 512 x 512 pixel matrix over a field-of-view (FOV) of 45 cm for electron density and RANDO phantoms, and 50 cm for lung patients. Slice thickness was fixed to 3 mm.

CBCT images of phantoms and lung patients were acquired with a Varian OBI unit (V 1.4; Varian Medical Systems Inc., Palo Alto, CA), which was calibrated according to Varian's user manual (Varian, 2006). CBCT images of the electron density phantom, RANDO phantom, and lung patients were acquired in "thorax mode" with the following settings: 110 kVp, 20 mA, 20 ms/pulse, scan length = 16 cm. For these scans, the system was set to half-fan (HF) mode, and used a corresponding bow-tie filter. In general, CBCT image acquisition uses approximately 650 x-ray pulses per rotation, with a gantry rotation time of approximately 60 s. Image reconstruction for the CBCT images also spanned a 512 x 512 pixel matrix over a FOV of 45 cm for the electron density and RANDO phantoms, and lung patients. Slice thickness for all CBCT images were set to 3.0 mm.

4.2.3 Deformed CBCT (dCBCT) images

Inter-fraction organ motion creates variations in patient anatomy when comparing CBCT to PCT lung images acquired at different scan times. These variations contribute to dose differences between treatment plans based on either PCT or CBCT image data [13, 18]. Image registration software was therefore used to deform CBCT data to PCT images, producing a deformed CBCT image set (dCBCT). The dCBCT image retains CT number data from the original CBCT image, but maintains the anatomical geometry from the PCT study. Our registration method, developed in-house, uses the algorithm known as ANIMAL (automated non-linear image matching and anatomical labeling) [31, 32]. This algorithm uses 3D simplex optimization, and was previously validated in a lung study [33] using volumes provided by the Deformable Image Registration (DIR)-laboratory group [34]. Following a similar analysis, 3 thorax patients were examined in a separate study, and our technique produced a mean registration error of 2.53 mm when comparing the dCBCT and PCT image sets [35, 36], even when the fields of view were different. Note that in this work, intra-fraction motion effects were not considered as both the PCT and CBCT images were acquired with slow scanning protocols to produce time-averaged CT numbers.

For this level of accuracy, dose differences due to mis-registration between image sets should be minimal. For instance, Yang et al. 2007 purposely introduced registration errors of 3 mm between PCT and CBCT image sets of patients. Their results showed negligible dose differences due to registration error ($< 1.5\%$) [13]. In our study, we observed greater than 10% differences for dose calculated within the PTV using PCT versus deformed CBCT image sets. The magnitude of these differences is characteristic of LED due to ultra-low lung density, not smaller errors in image registration.

4.2.4 CT number corrective techniques

4.2.4.1 CT number (HU) to relative electron density (RED curve)

Phantoms may be used to produce lung-specific HU-to-RED conversion curve [15, 12, 20, 21]; however, previous efforts have shown that the chosen phantom should reproduce photon scattering conditions for a comparable volume to that of the body region to be imaged [20, 21]. We used the large electron density phantom for HU-to-RED conversion to create a planning HU-to-RED conversion curve (or RED_{PCT}), and a cone-beam HU-to-RED conversion curve (or RED_{CBCT}).

4.2.4.2 Bulk CT (BCT) images

Bulk CT number replacement in large regions of interest may be used to avoid inaccurate CBCT number data [37, 38]. In this study, MicroView Analysis⁺ software V2.2 (GE Healthcare[®], Waukesha, WI) was used to create bulk-density images (BCT) of the lung patients. The software has a 3-dimensional (3D) tissue segmentation tool that allowed for selection of adipose, lung, muscle, and bone tissue regions from the PCT images of the lung patients. Using these 3D volumetric tissue selections, a single average CT number was calculated from the PCT data for each tissue type: $PCT_{adipose} = -95 \pm 74$ HU, $PCT_{bone} = 404 \pm 234$ HU, $PCT_{muscle} = 58 \pm 25$ HU and $PCT_{lung} = -746 \pm 101$ HU. A similar process was used to segment the 3D tissues of the dCBCT lung image sets, where each dCBCT voxel was replaced with a corresponding regional average tissue PCT number.

4.2.4.3 LED-sensitive CT (LCT) images

LED enhances the sensitivity of the dose calculation to small variations in lung density, and perturbs the dose distribution for SBRT of lung cancer [39]. If lung pixel value replacement is to be attempted, the substituted density should offset artificial LED. Figure 4-2 displays the relative depth dose factor (RDDF) for a 6 MV (3x3 cm²) photon

field that represents the equivalent fields used in our volume modulated arc therapy (VMAT) plan for our case study (i.e. one of the three patients). The critical lung density that causes severe LED (RDDF $\sim \leq 0.8$) is approximately 0.2 g/cm^3 or -800 HU, and is used as the CT number threshold for selective pixel substitution. This value is predicated on avoiding the region of Fig. 4-2 where the RDDF is strongly dependent on density. Fig. 4-3 shows histograms of CT number data acquired from the lung tissue within PCT and dCBCT data sets for this patient. Within the PCT image, we selected pixels with values below the threshold (-800 HU) and calculated an average LCT number, $LCT = -882 \pm 39 \text{ HU}$. Next, all pixel values below the threshold within the dCBCT lung volume were selected, and **only** these pixel values were replaced with the average LCT number. In this way, we produced density maps that are more representative of true density, and do not induce artificial LED. This process was repeated for the remaining two lung patients.

RDDF maps were produced from the PCT, dCBCT, BCT, and LCT image sets to map regions of expected electron disequilibrium and to explain observed dosimetric differences. These disequilibrium maps were estimated by converting CT number data to tissue density using a HU-to-density curve derived from PCT images of the electron density phantom. Then, each pixel-by-pixel density value was converted to a corresponding RDDF number using the relation below:

$$RDDF = 0.1503 + 0.7998(1 - (6.7954 \times 10^{-5})^\rho) \quad (4.3)$$

where ρ represents the CT-derived tissue density per pixel. SigmaPlot V.11 (Systat Software Inc., Chicago, IL) was used to determine equation (4.3) by fitting an exponential function to the data displayed in Fig. 4-2.

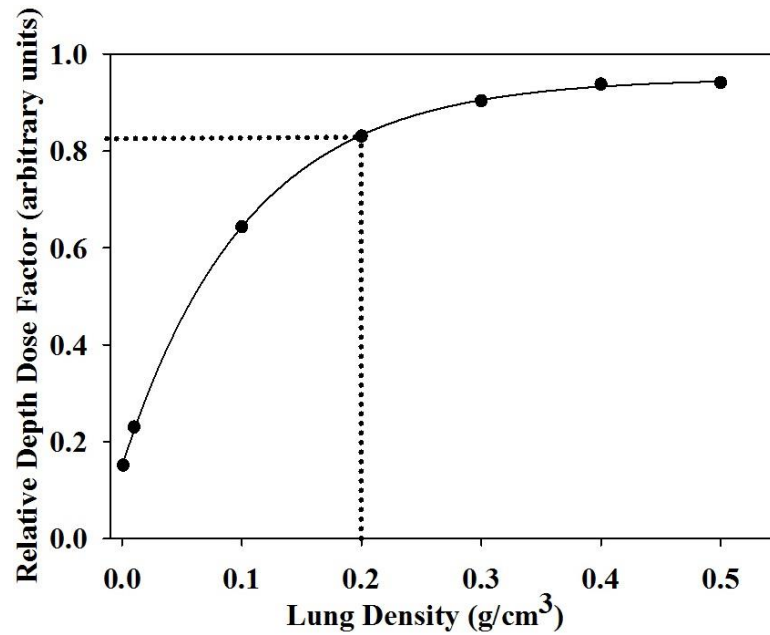


Figure 4-9 shows the Relative Depth Dose Factor (RDDF) [30] for a 6 MV (3x3 cm²) photon field – the radiation therapy parameters that approximately match the clinical situation described herein. Note that the RDDF \ll 1 for lung densities below 0.2 g/cm³, which indicates the onset of severe LED. This threshold was chosen in order to avoid the region where the RDDF was strongly dependent on density (i.e. the region indicated to left and below the dotted line shown above).

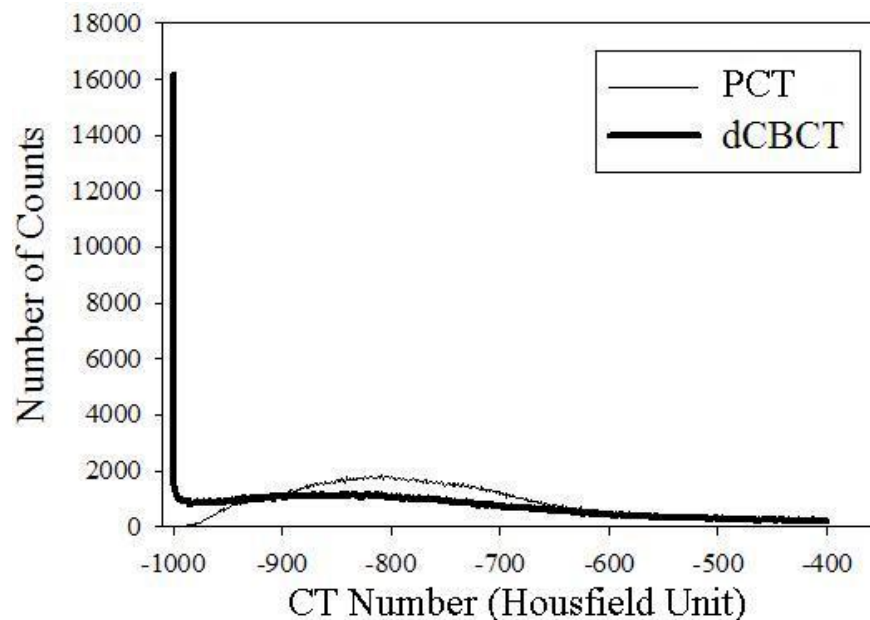


Figure 4-3 displays CT number histograms acquired from the lung tissue within PCT and dCBCT image sets. The dCBCT lung histogram is largely populated by ultra-low artificial lung densities (< 0.1 g/cm³ or -900 HU).

4.2.5 Dose calculations with treatment planning system (TPS)

For radiotherapy planning purposes, the PCT, dCBCT, LCT and BCT image sets for all three lung patients were entered into the Philips Pinnacle³ TPS (Philips Medical Systems, Madison, WI) for inverse plan optimization. Note that we only report the treatment parameters relevant to the example case study; however, a similar approach was used to treat all three patients. A planning target volume (PTV) contour was created to cover the full range of tumour motion over the breathing cycle (volume $\approx 10 \text{ cm}^3$). 6 MV beams (field size $\approx 3 \times 3 \text{ cm}^2$) were centered on the tumor using a 225° VMAT technique, as is commonly used in our center. The approximate $3 \times 3 \text{ cm}^2$ field size was determined by calculating the equivalent square field size per VMAT segment in accordance with the following equation:

$$FS = \frac{\sum_i^N (MU_i)(ESFS_i)}{\sum_i^N (MU_i)} \quad (4.4)$$

where FS is the fluence-weighted average field size, N is the total of segments (i.e. beam angles), i is the individual segment, MU_i is the monitor unit per segment, and $ESFS_i$ is the equivalent square field size per segment. FS was used to determine an appropriate RDDF equation, which is beam energy and field size dependent.

The VMAT plan was designed such that the constraints of the ROSEL study [39] were satisfied using the PCT data set for dose calculation. The planned dose prescription was set to 54 Gy (delivered in 3 fractions) to 95% of the PTV (i.e. D_{95} prescription). The monitor units (MUs), beam geometry, and contours from the PCT plan were copied “as is” onto dCBCT, LCT, and BCT image-based treatment plans. A 3D dose grid spacing of $0.25 \times 0.25 \times 0.25 \text{ cm}^3$ was used for dose calculations. As well, dose results were analyzed using Computational Environment for Radiotherapy Research [40] software run within Matlab R2012a (The MathWorks Inc., Natick, MA). For consistency of intercomparisons, the collapsed cone convolution (CCC) algorithm was selected for dose computations as it is a commercially available clinical option. The suitability of the CCC algorithm for accurate dose calculation under SBRT conditions has been assessed by multiple authors [27, 41, 42, 43, 44, 45]. These investigators report dose calculation

inaccuracies between 1-4% using the CCC algorithm. In our study, observed dose differences between the various image-based plans were greater than the 1-4% range, which is indicative of dose variations due to changes in CT-derived density under conditions of LED. Finally, we refer the reader to Table **4-1** for a review of the experimental design.

Table 4-1 A summary of techniques referred to in this work. The PCT is a time averaged multi-slice helical CT image of the patient (our standard for comparison). The CBCT data set is the originally acquired cone-beam CT image of the patient. Whereas the dCBCT image contains CBCT image data, but deformed onto PCT geometry. The BCT image set is derived from the deformed cone-beam CT image of the patient using pixel-by-pixel replacement with bulk substitutes created from different tissues within the PCT (lung, adipose, muscle, bone). The LCT image set is a modified version of the dCBCT, where *only specific* lung pixels are replaced with a LED sensitive substitute originating from the PCT. The RED_{PCT} was derived from multi-slice helical images of the electron density phantom. The RED_{CBCT} was derived from CBCT images of the electron density phantom. The treatment planning system used the RED_{PCT} curve to convert PCT, dCBCT, LCT, and BCT image sets to tissue electron density. As well, the feasibility of converting dCBCT numbers to an accurate tissue electron density was tested by using the RED_{CBCT} curve. Five dose distributions were calculated for the same VMAT plan: PCT Dose (as the fixed reference for all comparisons), LCT Dose, BCT Dose, dCBCT Dose (RED_{PCT}), and dCBCT Dose (RED_{CBCT}).

CT Data	Image Source	Deformation Required?	Pixel Substitution	Source of CT number data	HU-to-RED Conversion
PCT	PCT	No	N/A	PCT	RED _{PCT}
dCBCT	CBCT	Yes	N/A	CBCT	RED _{PCT}
dCBCT	CBCT	Yes	N/A	CBCT	RED _{CBCT}
BCT	CBCT	Yes	Regional tissue-based	Average tissue PCT numbers	RED _{PCT}
LCT	CBCT	Yes	LED threshold-based	CBCT and average PCT lung numbers	RED _{PCT}

4.3 Results

4.3.1 RANDO phantom and lung patient CT image data

We obtained PCT and CBCT images of the RANDO phantom, displayed in Figs. 4-4 (a) and (b). Note the CBCT shadow artifacts in the region of the spine and periphery of lung in Fig. 4-4 (b). Figures 4-5 (a) and (b) display a PCT and dCBCT image for the lung patient case study, respectively. The image quality of the dCBCT lung was inferior compared to the PCT image. Many image regions showed shadow, blur, and streak artifacts, and it was challenging to distinguish muscle from fat. Quantitatively, Figs. 4-5 (c) and (d) compare the PCT and dCBCT lung densities below 0.2 g/cm^3 or -800 HU . The dCBCT image contained many artificially low density regions.

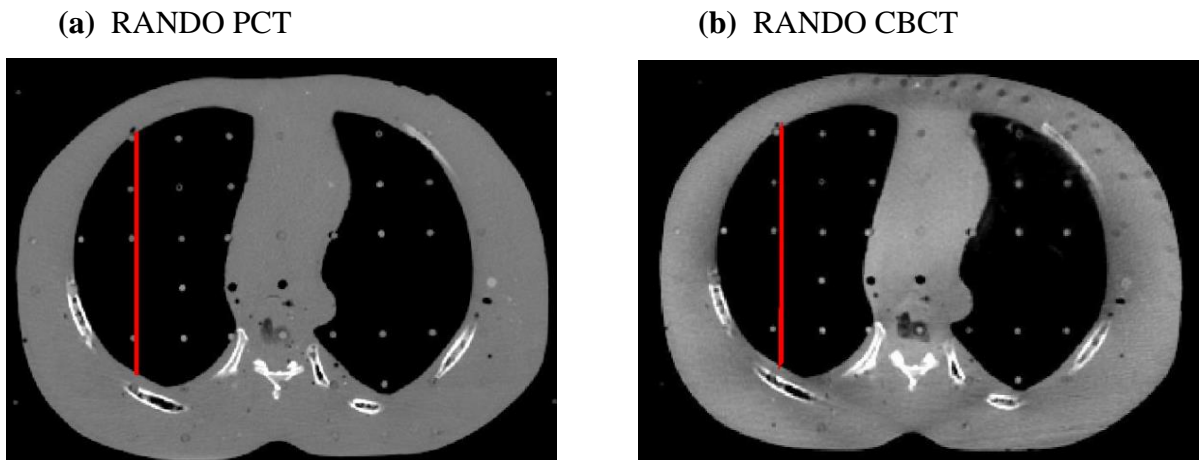


Figure 4-4 (a) PCT image and (b) CBCT image of the RANDO phantom. The red line indicates where CT number comparisons are made in **Figure 4-6**. Notice the CBCT shadow artifacts in **Fig. 4-4 (b)**.

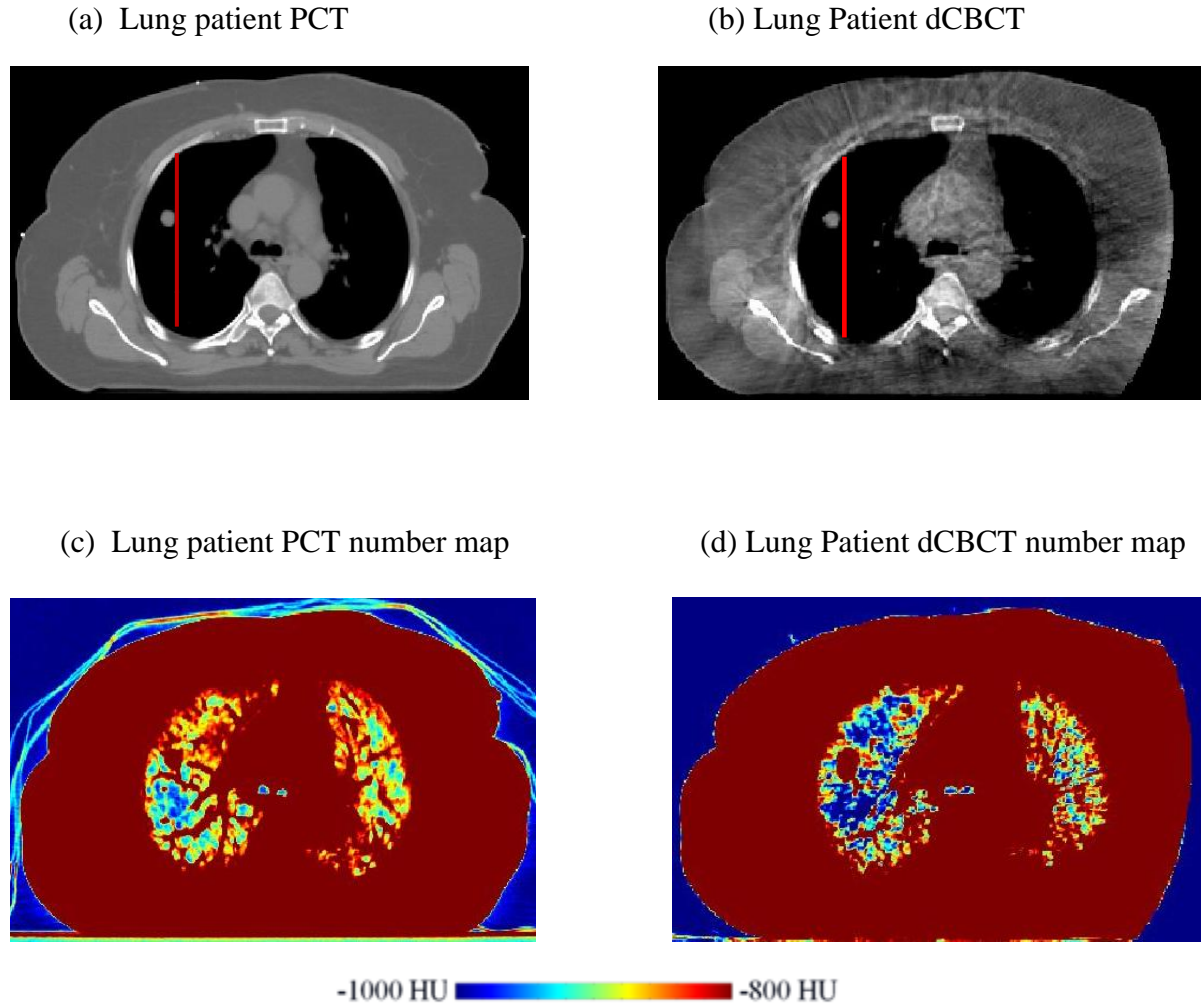


Figure 4-5 (a) Planning CT (PCT) image and (b) deformed CBCT (dCBCT) image of the lung patient. The red line indicates the image profile region where CT number comparisons were made in subsequent figures. Please note that the profile is within the lung tissue proximal to the tumor. **Figs 4-5** (c) and (d) display CT number intensity colour maps of lung tissue within the PCT and dCBCT patient images (level = -900 HU, window = +/- 100 HU). **Figure 4-5** (d) shows that dCBCT lung tissue appears much lower in density.

Figure 4-6 displays the CT number profiles acquired from the PCT and CBCT images of the RANDO phantom. In general, the CBCT profile shows values less than the PCT profile (reduction of 200 HU). Figure 4-7 displays the CT number profiles acquired for the planning CT, deformed cone-beam CT, LED-sensitive CT and bulk CT image sets of the lung patient. The BCT number profile is set to a fixed average value of -746 HU for the entire dCBCT lung volume. The LCT number of -882 HU was used to substitute

only those dCBCT lung pixels that produce LED (dCBCT number ≤ -800 HU). Note that the majority of the dCBCT numbers were less than the corresponding PCT numbers in lung. In particular, dCBCT numbers were as low as -1000 HU (0 g/cm^3), a density corresponding to vacuum. This outcome is non-physical, and resulted from CBCT artifacts. More importantly, the severity of CBCT number undervaluation is worse in the lung patient than in the RANDO phantom [compare Figs. 4-4 (b) and 4-5 (b)], implying that a static thorax phantom does not adequately model respiratory motion.

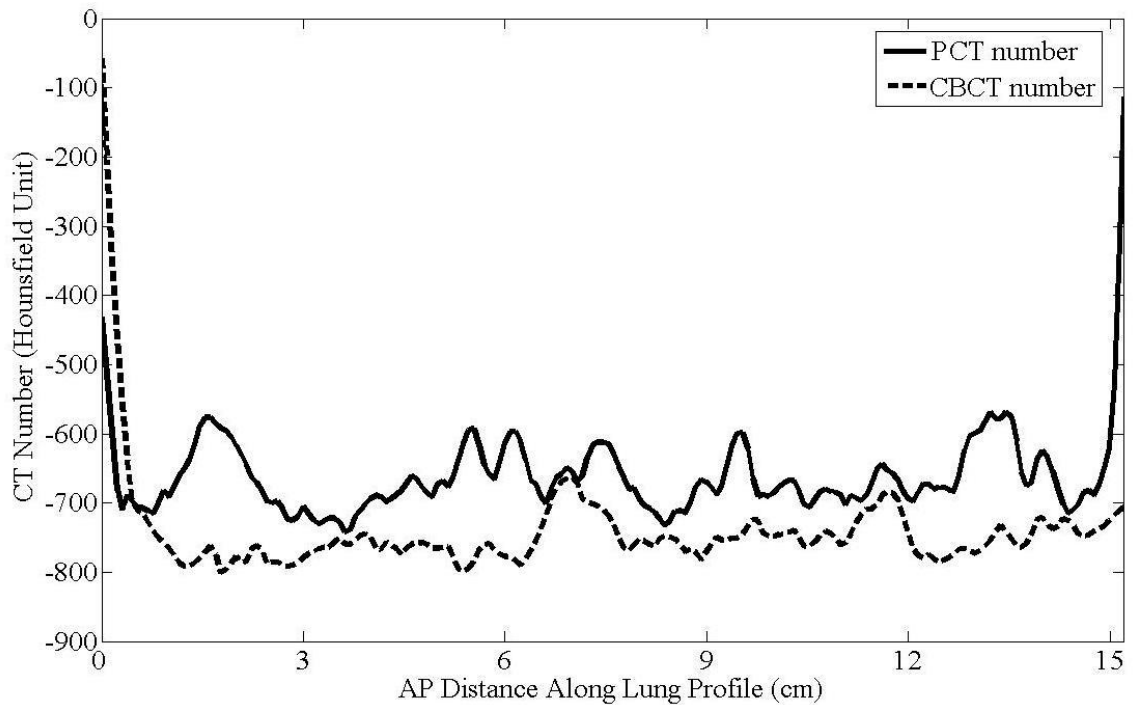


Figure 4-6 CT number profiles extracted from the PCT and CBCT images of the RANDO phantom (see Figs. 4-4 (a) and (b) for profile location). CBCT numbers are reduced by as much as 200 HU, compared with PCT data.

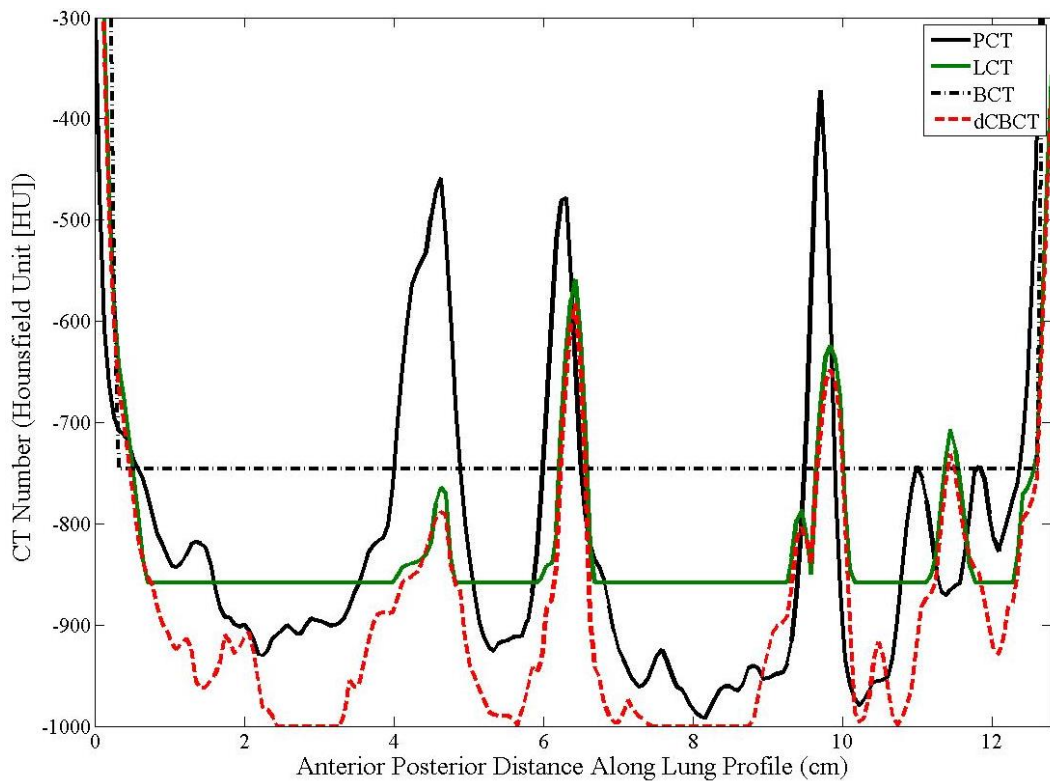


Figure 4-7 CT number profiles extracted from the PCT, LCT, dCBCT, and BCT images of the lung patient (see **Figs. 4-5 (a)** and **(b)** for profile location). An average lung BCT number of -746 HU was calculated by averaging all of the CT numbers from the entire PCT lung volume. A lung LCT number was calculated by averaging only those CT numbers that establish LED from the PCT lung volume. The dCBCT numbers undervalue the PCT numbers.

4.3.2 Dose comparison using CBCT corrective techniques

Figure 4-8 compares the VMAT calculated dose distributions using the planning CT, deformed cone-beam CT, bulk CT, or LED-sensitive CT lung images. Figure 4-8(a) shows the PCT image of the example lung patient with the calculated dose distribution overlaid on anatomy (to serve as the control case for inter-comparison). Figures 4-8(b) - (e) display the PCT image of the lung patient with overlying dose distributions calculated from the dCBCT, BCT, and LCT image sets. Figures 4-8(f) - (i) all present the PCT lung image with dose differences, Δ ($\Delta = x - \text{PCT dose}$, where x is the dose based on test cases of either dCBCT images with RED_{PCT} or RED_{CBCT} conversion, bulk CT, or substituted LED-sensitive CT numbers).

The dose distributions in Figs. **4-8(a) – (e)** have similar value and shape in the low dose and shallow dose-gradient regions. In regions where there is high dose and steep dose-gradients (in the vicinity of the PTV) there are large dose discrepancies. The dose difference distribution in Fig. **4-8(f)** shows that the dCBCT image-based plan, based on RED_{PCT} conversion, exhibits lower dose regions with $\Delta \leq -5.4$ Gy (i.e. $\leq 10\%$ of the prescription dose). Comparatively, Fig. **4-8(g)** shows that the dCBCT image-based plan using RED_{CBCT} conversion under-values the dose near the PTV to a lesser extent, and the depressed dose region encompasses a smaller region. On the contrary, Fig. **4-8(h)** shows that the BCT lung plan yielded a dose increase ($\Delta \geq 5.4$ Gy) in lung tissue. Figure **4-8(i)** shows that the LCT image-based plan produced a dose distribution that closely matched the PCT based plan, with minimal Δ in the vicinity of the tumor.

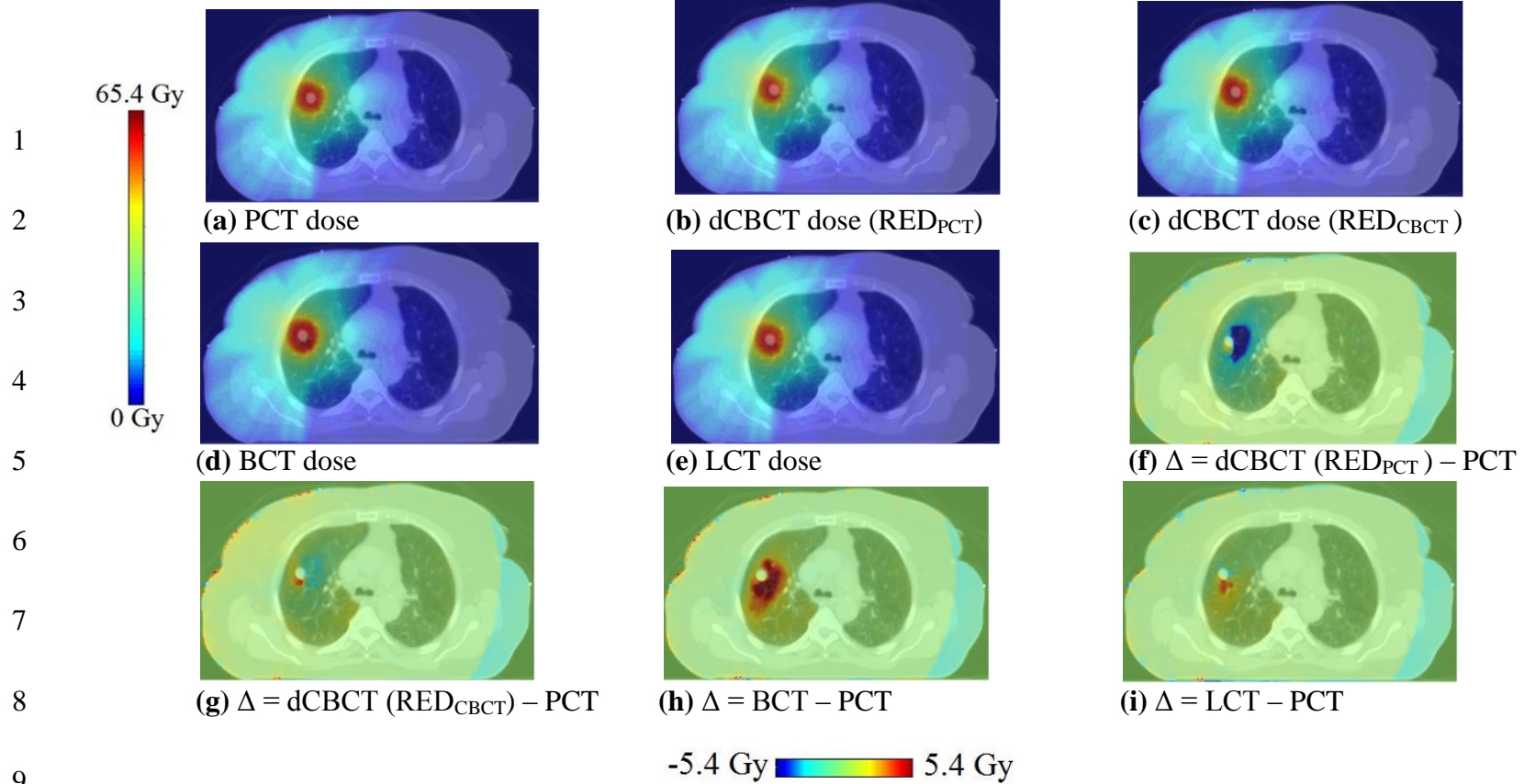


Figure 4-8 (a) - (e) shows the PCT, dCBCT, BCT, or LCT VMAT dose distributions overlaid on the PCT image. **Figs. 4-8 (f)-(i)** show the dose differences, Δ , overlaid on the PCT image. The largest differences occur in regions with steep dose gradients.

Figure 4-9 compares the dose-volume histograms (DVHs) for the PTV (note the magnified view). The D₉₅ for the PCT, LCT, BCT, dCBCT(RED_{PCT}), and dCBCT(RED_{CBCT}) image-based plans were 54Gy, 56Gy, 59Gy, 47Gy, 52Gy. Both PTV structures from the dCBCT (RED_{PCT}) and dCBCT (RED_{CBCT}) plans produced DVHs that received less dose to a smaller volume (poorer coverage) when compared to the PCT planning target volume. These results are clinically unacceptable as the D₉₅ prescription criterion (i.e. 54Gy) was not met. In contrast, the PTV from the BCT image-based plan produced a DVH that generally received more dose, while the DVH from the LCT plan matched the PCT DVH the closest.

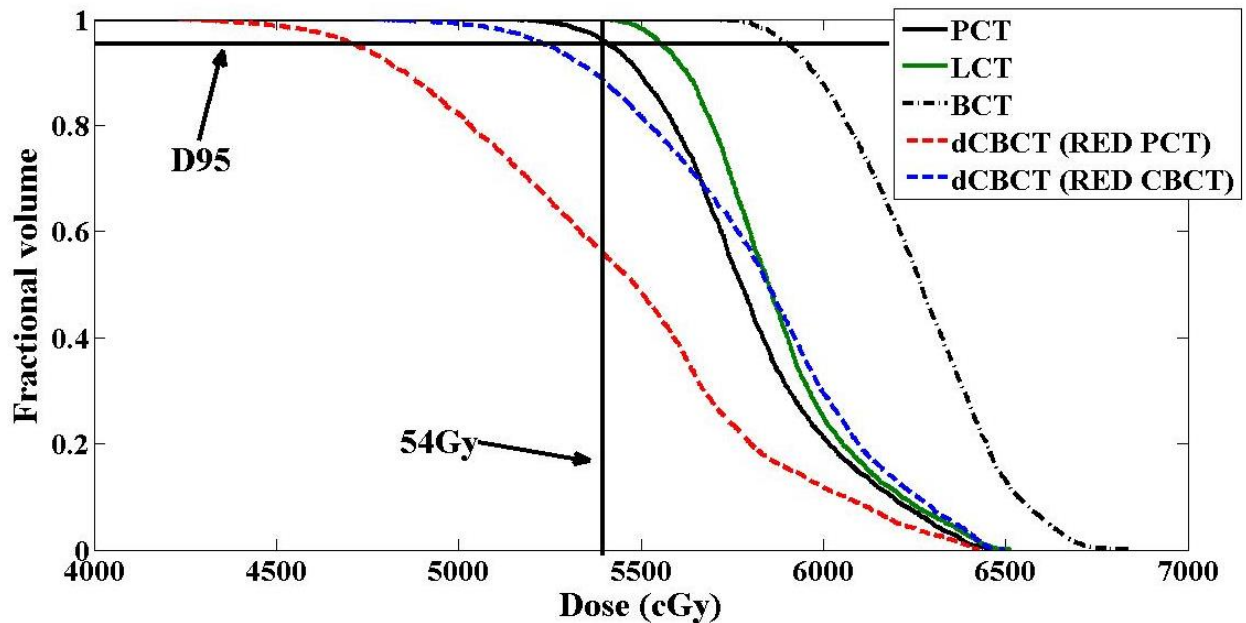


Figure 4-9 shows dose volume histograms comparing calculated VMAT dose for the planning target volume (PTV) using either the PCT, LCT, dCBCT (RED_{PCT}), dCBCT (RED_{CBCT}), or BCT image-based plans. The LCT DVH most closely matched the PCT DVH.

4.4 Discussion

4.4.1 Disequilibrium maps

Figure 4-10 displays the Relative Depth Dose Factor maps corresponding to the PCT, dCBCT, BCT, and LCT image sets (location of the each map was selected to match that shown in Fig. 4-5) for the test patient. These results can be interpreted as lateral electron disequilibrium maps, and provide a physical basis for understanding the dosimetric results (see Fig. 4-8). Under these treatment conditions, lateral electron disequilibrium is established for lung densities of 0.2 g/cm^3 or lower ($< -800\text{HU}$) [see Fig. 4-2] for a comparable field size. Figure 4-10 shows lung regions that create LED (RDDF < 1), and cause reductions in central-axis depth dose.

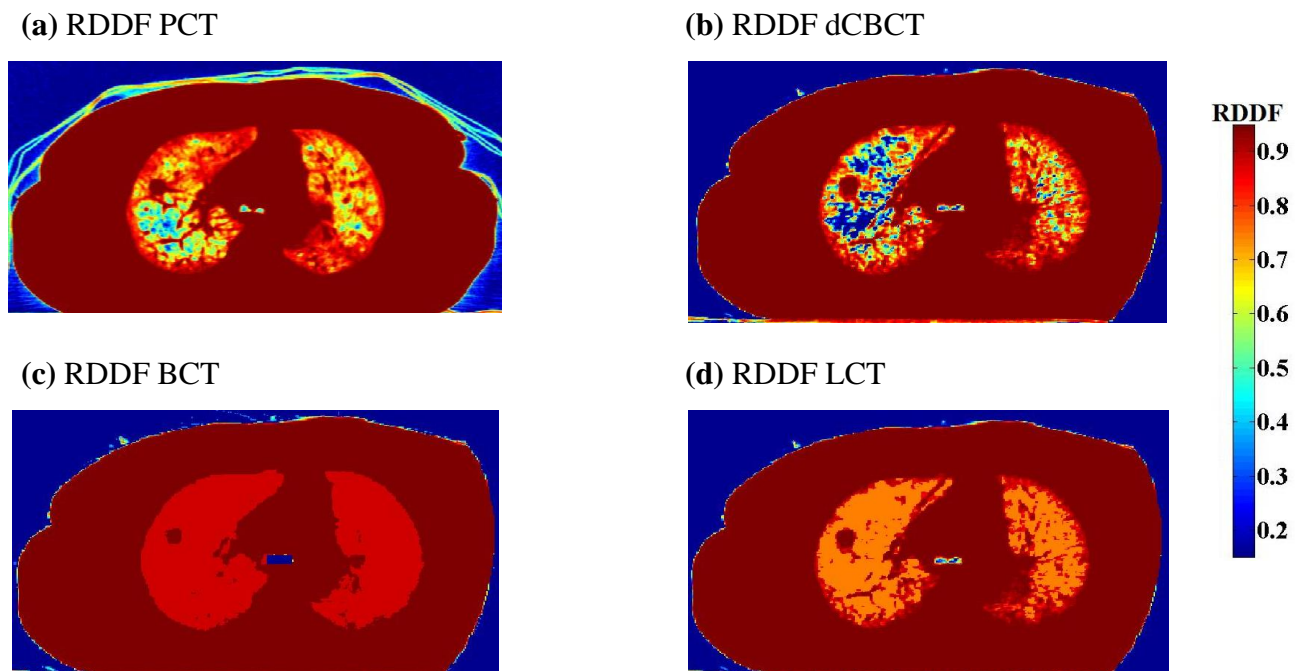


Figure 4-10 shows the Relative Depth Dose Factor (RDDF) maps acquired from the PCT, dCBCT, BCT, and LCT image sets. These maps (calculated using data from **Fig. 4-2**) provide regional information concerning the estimated magnitude of LED. The RDDF value quantifies the extent/severity of LED, and regions of lung tissue that are more apt to establish LED are easily identified.

For example, the planning CT image contains many contiguous lung densities that produce LED [see Figs. 4-5 (c) and 4-10 (a)], and we expect a true decrease in dose in these regions. The deformed cone-beam CT lung image contains many erroneous ultra-low pixel values (< -900 HU) [see Fig. 4-5 (d)], which produced an under-valued RDDF map causing severe artificial LED [see Fig. 4-10 (b)]. As a result, the dose is drastically reduced in these regions due to the effects of exaggerated LED. Conversely, using the BCT lung image for dose calculation over-estimated the dose in lung tissue. By setting the entire lung to an average PCT number equal to -746 HU or 0.254 g/cm³ (a lung density > 0.2 g/cm³), electron equilibrium is artificially maintained [RDDF ~ 1 ; see Fig 4-10 (c)], and dose in lung tissue is enhanced due to preserved photon fluence, as predicted by simpler dose calculation algorithms [46]. Substituting only those dCBCT lung pixels that cause artificial LED with an appropriate CT number (-882 HU), produced an LCT RDDF [see Fig 4-10 (d)], which is similar, but not identical to the RDDF PCT map. Thus, the VMAT LCT image-based dose distribution was more representative of the reference PCT dose. Note these results are only relevant for a 6 MV (3×3 cm²) photon source. The RDDF varies for different combinations of beam energy, field size, and lung density. A unique RDDF should be produced to match the clinical treatment conditions [30].

It should be noted that the results described above are specific to the example test patient. The dose distribution within the tumour and lung tissues are affected by tumour location, size, and patient lung density. For example, a similar analysis was performed on two additional patients with tumours located within lung tissue at the chest wall interface. Dosimetric comparison of the correction techniques (i.e. D95 analysis) revealed similar trends as described above, but with dose differences of a smaller magnitude. For RT conditions involving electronic equilibrium (e.g. large lung tumours adjacent to soft tissues) differences between corrective techniques maybe marginal. However, for circumstances that enhance LED (e.g. small tumours entirely embedded within lung tissue), substantial dose variations with the corrective methods maybe observed.

4.4.2 Recommendations

4.4.2.1 Dose calculations with uncorrected CBCT thorax images

The direct use of CBCT lung patient data in a TPS is not recommended. This will produce artificially low dose results in lung tissue and tumour and lead to incorrect decisions in DART. Clinically, an unsafe over-dosage would be prescribed to the patient to counter the artificial under-dosage. For example, considering results from all three patients, an increase in the prescription dose of 2 to 7Gy (or 4 to 13%) was required to counter the artificially low dose results produced by the dCBCT (RED_{PCT}) image-based VMAT plan.

4.4.2.2 Thorax specific HU-to-RED conversion curve

The use of a static phantom for conversion of lung CBCT numbers to tissue electron density is also not recommended. We scanned both the electron density and RANDO phantoms using the same CBCT parameters (OBI V1.4) used to scan thorax patients. The CBCT artifacts in images of the phantoms were not as severe as those artifacts seen within CBCT images of lung patients. The CBCT numbers of plastic lung tissue within the RANDO or electron density phantom were not as low as -1000 HU; and hence an accurate HU-to-RED conversion curve (i.e. RED_{CBCT}) could not be derived using the static electron density phantom. Consequently, the dCBCT image-based plan using the RED_{CBCT} produced an artificially low calculated dose to lung tissue and tumour for the case study. Considering results for all three patients, the D95 ranged from 51.5 Gy up to 57.5 Gy, which represents dose variations with respect to the prescription dose of -5% and 6%, respectively.

Guan & Dong, 2009 and Hatton et al., 2009 have shown that the CBCT HU-to-RED conversion curve is highly dependent on the phantom's plastic composition, pin size, radial and longitudinal dimensions, and x-ray scatter volume [21, 20]. These studies did not account for the additional effects of lung patient breathing motion. We expect that additional CBCT lung image artifacts found in patient data (not seen in static phantoms)

are due to patient respiratory motion [8, 9, 11, 47, 13]. A more accurate HU-to-RED curve may be derived from a deformable “breathing” lung phantom containing tissue equivalent plastics. For example, Serban et al., 2008 and Court et al., 2010 have developed such a phantom, and a future study focused on CBCT HU-to-RED stability under breathing conditions may be useful [48, 49].

4.4.2.3 Bulk CT Substitution

Replacement of the entire CBCT lung volume with one average CT number is not recommended. Pixel replacement of patient lung CBCT numbers with a fixed average PCT number may enforce electron equilibrium in regions where true LED has occurred, and this will result in artificially high dose values. In order to compensate clinically, as observed in all three patients, an under-dosage ranging from 0.5 Gy up to 5 Gy (1% to 9%) would be prescribed to the patient.

4.4.2.4 LED-sensitive CT number substitution

Partial volume substitution of the CBCT lung volume is recommended. We observed marked improvements in dose distributions when a threshold setting was used to selectively replace dCBCT lung CT numbers that cause artificial lateral electron disequilibrium. Therefore, given a specific plan and knowledge of treatment parameters that establish LED, and a trustworthy dose algorithm, one can use the local RDDF parameter to guide the selective replacement of CBCT lung density. In terms of dose calculation accuracy, the results shown here-in suggest that the LCT image-based dose distribution is comparable to the PCT-based reference for SBRT of three lung cancer patients. However, a future study involving a greater number of patients, tumour sizes and locations is required to fully assess the accuracy and limitations of the LCT substitution technique.

Currently, efficient DART may be possible using the LCT substitution technique as this method could save considerable time while the patient is on the treatment table. A five step process is required to carry out the LCT method:

1. Determine the $RDDF(\rho_{lung})$ function for the desired RT parameters (see Fig. 4-2) using a lookup table or database [30].
2. From the $RDDF(\rho_{lung})$ curve, decide on the threshold lung density, ρ_{thr} , that establishes lateral electron disequilibrium ($RDDF(\rho_{lung}) < 1$).
3. Apply ρ_{thr} to the originally acquired PCT lung data (selecting only pixels with $PCT_{lung} < \rho_{thr}$) and calculate an average CT number (i.e. LCT) for this subset of low-density pixels.
4. Upon acquisition of the up-to-date CBCT image, replace only those CBCT lung pixels with densities less than the threshold ($CBCT_{lung} < \rho_{thr}$) with the average LCT number, forming the new LCT image set, avoiding artificially low densities caused by CBCT artifacts.
5. Calculate “dose distribution of the day” using the LCT image set.

Steps 1-3 could be conducted off-line before delivery of the first fraction of radiation. Step 4 could be performed on-line and easily automated so that completion time was seconds or less. Step 5 is also performed online, and limited by the calculation speed of the TPS.

4.5 Conclusion

Our study demonstrates that CBCT artifacts can cause severe undervaluation of CBCT numbers in patient lung tissue, and erroneous perception of electron disequilibrium. This has the potential for misleading increases in delivered dose for adaptive radiotherapy in SBRT. Furthermore, such density-driven dose errors generally impair the decisions on dose re-optimization based on inaccurate cumulative dose distributions. We therefore

cannot recommend using CBCT lung images “as is” for solitary lung tumours treated by small-field radiation therapy. CBCT number correction techniques must be invoked for the thorax until suitable strategies are developed to overcome artifacts due to photon scattering and respiratory motion. Selective LED-sensitive substitution of pixel values considerably improves dose computation accuracy.

4.6 Acknowledgements

The authors would like to thank: Professor Jake Van Dyk, Dr. Jeff Chen, Dr. Eugene Wong, Dr. David Turnbull, Dr. David Holdsworth, Dr. Terry Peters, and Mr. Jeff Kempe for helpful conversation and advice in development of this work. Financial support from the Natural Sciences and Engineering Research Council of Canada (NSERC), and the Canadian Institutes of Health Research (CIHR) are also gratefully acknowledged.

4.7 References

- [1] T. G. Purdie, J.P. Bissonnette, K. Franks, A. Bezjak, D. Payne, F. Sie, M. B. Sharpe and D. A. Jaffray, "Cone-beam computed tomography for on-line image guidance of lung stereotactic radiotherapy: localization, verification, and intrafraction tumor position.," *Int J Radiat Oncol Biol Phys*, vol. 68, no. 1, pp. 243-252, May 2007.
- [2] D. Yan, "Adaptive radiotherapy: merging principle into clinical practice.," *Semin Radiat Oncol*, vol. 20, no. 2, pp. 79-83, Apr 2010.
- [3] J. H. Siewerdsen and D. A. Jaffray, "Cone-beam computed tomography with a flat-panel imager: magnitude and effects of x-ray scatter.," *Med Phys*, vol. 28, no. 2, pp. 220-231, Feb 2001.
- [4] G. Jarry, S. A. Graham, D. J. Moseley, D. J. Jaffray, J. H. Siewerdsen and F. Verhaegen, "Characterization of scattered radiation in kV CBCT images using

- Monte Carlo simulations.," *Med Phys*, vol. 33, no. 11, pp. 4320-4329, Nov 2006.
- [5] G. X. Ding, D. M. Duggan and C. W. Coffey, "Characteristics of kilovoltage x-ray beams used for cone-beam computed tomography in radiation therapy.," *Phys Med Biol*, vol. 52, no. 6, pp. 1595-1615, Mar 2007.
- [6] W. Giles, J. Bowsher, H. Li and F.-F. Yin, "Crescent artifacts in cone-beam CT.," *Med Phys*, vol. 38, no. 4, pp. 2116-2121, Apr 2011.
- [7] J. H. Siewerdsen and D. A. Jaffray, "Cone-beam computed tomography with a flat-panel imager: effects of image lag.," *Med Phys*, vol. 26, no. 12, pp. 2635-2647, Dec 1999.
- [8] T. Li, E. Schreibmann, Y. Yang and L. Xing, "Motion correction for improved target localization with on-board cone-beam computed tomography.," *Phys Med Biol*, vol. 51, no. 2, pp. 253-267, Jan 2006.
- [9] T. Li, A. Koong and L. Xing, "Enhanced 4D cone-beam CT with inter-phase motion model.," *Med Phys*, vol. 34, no. 9, pp. 3688-3695, Sep 2007.
- [10] S. Leng, J. Tang, J. Zambelli, B. Nett, R. Tolakanahalli and G.H. Chen, "High temporal resolution and streak-free four-dimensional cone-beam computed tomography.," *Phys Med Biol*, vol. 53, no. 20, pp. 5653-5673, Oct 2008.
- [11] T. Li, L. Xing, P. Munro, C. McGuinness, M. Chao, Y. Yang, B. Loo and A. Koong, "Four-dimensional cone-beam computed tomography using an on-board imager.," *Med Phys*, vol. 33, no. 10, pp. 3825-3833, Oct 2006.
- [12] Y. Rong, J. Smilowitz, D. Tewatia, W. A. Tomé and B. Paliwal, "Dose calculation on kV cone beam CT images: an investigation of the Hu-density conversion stability and dose accuracy using the site-specific calibration.," *Med Dosim*, vol. 35, no. 3, pp. 195-207, 2010.

- [13] Y. Yang, E. Schreibmann, T. Li, C. Wang and L. Xing, "Evaluation of on-board kV cone beam CT (CBCT)-based dose calculation.," *Phys Med Biol*, vol. 52, no. 3, pp. 685-705, Feb 2007.
- [14] S. Yoo and F.F. Yin, "Dosimetric feasibility of cone-beam CT-based treatment planning compared to CT-based treatment planning.," *Int J Radiat Oncol Biol Phys*, vol. 66, no. 5, pp. 1553-1561, Dec 2006.
- [15] A. Richter, Q. Hu, D. Steglich, K. Baier, J. Wilbert, M. Guckenberger and M. Flentje, "Investigation of the usability of conebeam CT data sets for dose calculation.," *Radiat Oncol*, vol. 3, p. 42, 2008.
- [16] M. Zijtveld, M. Dirkx and B. Heijmen, "Correction of conebeam CT values using a planning CT for derivation of the "dose of the day".," *Radiother Oncol*, vol. 85, no. 2, pp. 195-200, Nov 2007.
- [17] W. Hu, J. Ye, J. Wang, X. Ma and Z. Zhang, "Use of kilovoltage X-ray volume imaging in patient dose calculation for head-and-neck and partial brain radiation therapy.," *Radiat Oncol*, vol. 5, p. 29, 2010.
- [18] U. V. Elstrøm, B. A. Wysocka, L. P. Muren, J. B. B. and C. Grau, "Daily kV cone-beam CT and deformable image registration as a method for studying dosimetric consequences of anatomic changes in adaptive IMRT of head and neck cancer.," *Acta Oncol*, vol. 49, no. 7, pp. 1101-1108, Oct 2010.
- [19] G. X. Ding, D. M. Duggan, C. W. Coffey, M. Deeley, D. E. Hallahan, A. Cmelak and A. Malcolm, "A study on adaptive IMRT treatment planning using kV cone-beam CT.," *Radiother Oncol*, vol. 85, no. 1, pp. 116-125, Oct 2007.
- [20] J. Hatton, B. McCurdy and P. B. Greer, "Cone beam computerized tomography: the effect of calibration of the Hounsfield unit number to electron density on dose calculation accuracy for adaptive radiation therapy.," *Phys Med Biol*, vol. 54, no. 15,

pp. N329--N346, Aug 2009.

- [21] H. Guan and H. Dong, "Dose calculation accuracy using cone-beam CT (CBCT) for pelvic adaptive radiotherapy.," *Phys Med Biol*, vol. 54, no. 20, pp. 6239-6250, Oct 2009.
- [22] G. G. Poludniowski, P. M. Evans and S. Webb, "Cone beam computed tomography number errors and consequences for radiotherapy planning: an investigation of correction methods.," *Int J Radiat Oncol Biol Phys*, vol. 84, no. 1, pp. e109--e114, Sep 2012.
- [23] P. Yadav, V. Ramasubramanian and B. R. Paliwal, "Feasibility study on effect and stability of adaptive radiotherapy on kilovoltage cone beam CT.," *Radiol Oncol*, vol. 45, no. 3, pp. 220-226, Sep 2011.
- [24] D. Létourneau, R. Wong, D. Moseley, M. B. Sharpe, S. Ansell, M. Gospodarowicz and D. A. Jaffray, "Online planning and delivery technique for radiotherapy of spinal metastases using cone-beam CT: image quality and system performance.," *Int J Radiat Oncol Biol Phys*, vol. 67, no. 4, pp. 1229-1237, Mar 2007.
- [25] L. J. Rosenblum, R. A. Mauceri, D. E. Wellenstein, F. D. Thomas, D. A. Bassano, B. N. Raasch, C. C. Chamberlain and E. R. Heitzman, "Density patterns in the normal lung as determined by computed tomography.," *Radiology*, vol. 137, no. 2, pp. 409-416, Nov 1980.
- [26] E. Yorke, L. Harisiadis, B. Wessels, H. Aghdam and R. Altemus, "Dosimetric considerations in radiation therapy of coin lesions of the lung.," *Int J Radiat Oncol Biol Phys*, vol. 34, no. 2, pp. 481-487, Jan 1996.
- [27] L. R. Aarup, et al., "The effect of different lung densities on the accuracy of various radiotherapy dose calculation methods: Implications for tumour coverage," *Radiotherapy and Oncology*, vol. 91, no. 3, pp. 405-414, 2009.

- [28] R. P. Parker, P. A. Hobday and K. J. Cassell, "The direct use of CT numbers in radiotherapy dosage calculations for inhomogeneous media.," *Phys Med Biol*, vol. 24, no. 4, pp. 802-809, Jul 1979.
- [29] M. R. Sontag, J. J. Battista, M. J. Bronskill and J. R. Cunningham, "Implications of computed tomography for inhomogeneity corrections in photon beam dose calculations.," *Radiology*, vol. 124, no. 1, pp. 143-149, Jul 1977.
- [30] B. Disher, G. Hajdok, S. Gaede and J. J. Battista, "An in-depth Monte Carlo study of lateral electron disequilibrium for small fields in ultra-low density lung: implications for modern radiation therapy.," *Phys Med Biol*, vol. 57, no. 6, pp. 1543-1559, Mar 2012.
- [31] D. L. Collins, C. J. Holmes, T. M. Peters and A. C. Evans, "Automatic 3-D model-based neuroanatomical segmentation," *Human Brain Mapping*, vol. 3, no. 3, pp. 190-208, 1995.
- [32] E. Heath, D. L. Collins, P. J. Keall, L. Dong and J. Seuntjens, "Quantification of accuracy of the automated nonlinear image matching and anatomical labeling (ANIMAL) nonlinear registration algorithm for 4D CT images of lung.," *Med Phys*, vol. 34, no. 11, pp. 4409-4421, Nov 2007.
- [33] G. Pierce, K. Wang, S. Gaede, J. Battista and T.Y. Lee, "The effect of an inconsistent breathing amplitude on the relationship between an external marker and internal lung deformation in a porcine model," *Medical Physics*, vol. 37, no. 11, pp. 5951-5960, 2010.
- [34] R. Castillo, E. Castillo, R. Guerra, V. E. Johnson, T. McPhail, A. K. Garg and T. Guerrero, "A framework for evaluation of deformable image registration spatial accuracy using large landmark point sets.," *Phys Med Biol*, vol. 54, no. 7, pp. 1849-1870, Apr 2009.

- [35] A. Wang, B. Disher, J. Battista and T. Peters, "Sci---Sat AM(1): Planning --- 11: Use of a Graphics Processor (GPU) for High-Performance Deformable Registration of Cone Beam (kV) and Megavoltage (MV) CT Images," 2010.
- [36] A. Wang, B. Disher, G. Carnes and T. M. Peters, "Rapid block matching based nonlinear registration on GPU for image guided radiation therapy," 2010.
- [37] Y. K. Lee, M. Bollet, G. Charles-Edwards, M. A. Flower, M. O. Leach, H. McNair, E. Moore, C. Rowbottom and S. Webb, "Radiotherapy treatment planning of prostate cancer using magnetic resonance imaging alone.," *Radiother Oncol*, vol. 66, no. 2, pp. 203-216, Feb 2003.
- [38] A. I. Saito, J. G. Li, C. Liu, K. R. Olivier and J. F. Dempsey, "Accurate heterogeneous dose calculation for lung cancer patients without high-resolution CT densities.," *J Appl Clin Med Phys*, vol. 10, no. 2, p. 2847, 2009.
- [39] C. W. Hurkmans, J. P. Cuijpers, F. J. Lagerwaard, J. Widder, U. A. {van der Heide}, D. Schuring and S. Senan, "Recommendations for implementing stereotactic radiotherapy in peripheral stage IA non-small cell lung cancer: report from the Quality Assurance Working Party of the randomised phase III ROSEL study.," *Radiat Oncol*, vol. 4, p. 1, 2009.
- [40] J. O. Deasy, A. I. Blanco and V. H. Clark, "CERR: a computational environment for radiotherapy research.," *Med Phys*, vol. 30, no. 5, pp. 979-985, May 2003.
- [41] O. I. Calvo, A. N. Gutiérrez, S. Stathakis, C. Esquivel and N. Papanikolaou, "On the quantification of the dosimetric accuracy of collapsed cone convolution superposition (CCCS) algorithm for small lung volumes using IMRT.," *J Appl Clin Med Phys*, vol. 13, no. 3, p. 3751, 2012.
- [42] P. Carrasco, N. Jornet, M. A. Duch, L. Weber, M. Ginjaume, T. Eudaldo, D. Jurado, A. Ruiz and M. Ribas, "Comparison of dose calculation algorithms in phantoms with

lung equivalent heterogeneities under conditions of lateral electronic disequilibrium.," *Med Phys*, vol. 31, no. 10, pp. 2899-2911, Oct 2004.

- [43] S. E. Davidson, G. S. Ibbott, K. L. Prado, L. Dong, Z. Liao and D. S. Followill, "Accuracy of two heterogeneity dose calculation algorithms for IMRT in treatment plans designed using an anthropomorphic thorax phantom.," *Med Phys*, vol. 34, no. 5, pp. 1850-1857, May 2007.
- [44] F. Hasenbalg, H. Neuenschwander, R. Mini and E. J. Born, "Collapsed cone convolution and analytical anisotropic algorithm dose calculations compared to VMC++ Monte Carlo simulations in clinical cases.," *Phys Med Biol*, vol. 52, no. 13, pp. 3679-3691, Jul 2007.
- [45] W. Takahashi, H. Yamashita, N. Saotome, Y. Iwai, A. Sakumi, A. Haga and K. Nakagawa, "Evaluation of heterogeneity dose distributions for Stereotactic Radiotherapy (SRT): comparison of commercially available Monte Carlo dose calculation with other algorithms.," *Radiat Oncol*, vol. 7, p. 20, 2012.
- [46] N. Papanikolaou, et al., "Tissue Inhomogeneity Corrections for Megavoltage Photon Beams, AAPM Report No 85, Task Group No 65 of the Radiation Therapy Committee of the American Association of Physicists in Medicine," *Med Phys*, 2004.
- [47] S. Leng, J. Zambelli, R. Tolakanahalli, B. Nett, P. Munro, J. Star-Lack, B. Paliwal and G.-H. Chen, "Streaking artifacts reduction in four-dimensional cone-beam computed tomography.," *Med Phys*, vol. 35, no. 10, pp. 4649-4659, Oct 2008.
- [48] L. E. Court, J. Seco, X.-Q. Lu, K. Ebe, C. Mayo, D. Ionascu, B. Winey, N. Giakoumakis, M. Aristophanous, R. Berbeco, J. Rottman, M. Bogdanov, D. Schofield and T. Lingos, "Use of a realistic breathing lung phantom to evaluate dose delivery errors.," *Med Phys*, vol. 37, no. 11, pp. 5850-5857, Nov 2010.
- [49] M. Serban, E. Heath, G. Stroian, D. L. Collins and J. Seuntjens, "A deformable

phantom for 4D radiotherapy verification: Design and image registration evaluation," *Medical Physics*, vol. 35, no. 3, pp. 1094-1102, 2008.

Chapter 5

5 Conclusion and Future Work

5.1 Summary and Conclusions

The following sections summarize each chapter, and present the overall conclusions from the thesis.

5.1.1 Radiation parameters that cause lateral electron disequilibrium (LED)

In chapter 2 of the thesis, we used Monte Carlo (MC) simulations to characterize the radiation therapy (RT) parameters that can cause LED. The analysis considered various combinations of beam energies (Co-60 up to 18 MV x-rays), field sizes ($1 \times 1 \text{ cm}^2$ up to $15 \times 15 \text{ cm}^2$), and lung densities (0.001 g cm^{-3} up to 1 g cm^{-3}) in a phantom geometry. We also examined the dosimetric effects of LED on the dose distribution within, and in the vicinity of, a simulated small lung tumour. In general, the dose within lung tissue was enhanced for decreasing lung density, as expected under conditions of charged particle equilibrium (CPE). However, at a specific ‘critical lung density’, this trend was broken, and a drastic reduction in lung dose was observed indicating the onset of LED. To determine the transition from CPE to LED conditions, we developed the relative depth dose factor (RDDF), which varied according to the extent of CPE disruption from equilibrium ($\text{RDDF} \sim \geq 1$) to disequilibrium ($\text{RDDF} < 1$) status. This metric is useful for approximating the severity of LED, and central-axis depth-dose reduction. With regard to tumour dose levels, large reductions were present at the tumour periphery under conditions of LED. At the tumour core, the level of dose depends on the tumour size, which can “re-build up” CPE to an extent. As smaller tumours lack the necessary depth to achieve full dose build-up, higher energy beams (e.g. 18 MV) may under-dose the tumour core for conditions involving LED.

In order to avoid these negative dosimetric effects, clinicians can use the RDDF metric to guide the selection of appropriate RT parameters, and/or suitable dose

calculation algorithms (superposition/convolution or MC techniques) for clinical trials involving small field treatment of lung cancer (e.g. SBRT). Further, at ultra-low lung densities ($\rho_{\text{lung}} < 0.1 \text{ g/cm}^3$), LED was shown to be unavoidable. This greatly impacts the radiation treatment planning of emphysematous lung cancer patients where large pockets of air ($\rho \sim 0.001 \text{ g/cm}^3$) remain trapped in the lung. In such cases, that are not uncommon for lung patients – careful consideration of LED is required in these circumstances [1]. Finally, under conditions of LED, it was discovered that the lung dose distribution became hyper-sensitive to small variations in density. This is of importance for adaptive SBRT planning where CT density is derived from cone-beam CT (CBCT) that is not as quantitative (yet) as diagnostic fan-beam CT. CBCT systems are more susceptible to artefacts and miscalibrations [2], and CBCT-derived density may be less accurate in lung tissue producing erroneous levels of LED and incorrect dose results. This issue was further explored in chapter 4 of the thesis.

5.1.2 Development of a novel SBRT technique to exploit LED

In chapter 3 of the thesis, we proposed a novel form of SBRT, called LED-optimized SBRT (LED-SBRT), which used specific radiotherapeutic (RT) parameters (derived from Chapter 2) to disrupt CPE purposely, with the aim of sparing healthy lung. In this work, MC simulations of a phantom and lung cancer patient were used to demonstrate the dosimetric effects of LED-SBRT. Further, we introduced a new ‘clinical tool’, i.e. LED maps, which can be used to visualize the magnitude and spatial distribution of LED for SBRT of a lung patient. To demonstrate the potential lung sparing capability of LED, we simulated SBRT arcs using 6 MV or 18 MV x-ray beam energies, collimated to various field sizes. Results from phantom simulations suggest that LED-SBRT can produce extremely steep dose gradients at the lung/tumour boundary, increased levels of tumour dose, while maintaining or reducing the normal lung dose. For example, comparing the normal lung dose at distance 2 cm away from the tumour edge, reductions of $\sim 70\%$ were observed using the LED-optimized arc (18 MV [1x1 cm²]) as opposed to the 18 MV [5x5 cm²] arc. In addition, the 18 MV [1x1 cm²] arc resulted in a central tumour hot spot $>125\%$, while still providing adequate dose coverage at the tumour edge (100%).

Similarly in the patient simulation, the LED-optimized plan [18 MV (3x1 cm²)] increased the maximal, mean, and minimal tumour dose by as much as 80Gy, 11Gy, and 3Gy when compared to a more conventional SBRT arc [6 MV (3x3 cm²)]. Also, the 18 MV (3x1 cm²) arc reduced or maintained lung dose metrics (i.e. MLD, V20, V5) at an acceptable level for the patient simulation.

We conclude that LED-SBRT has the potential to increase tumour dose levels, while at least maintaining the well-tolerated lung dose profile currently observed using traditional SBRT techniques. The hypothetical benefits of tumour dose elevation include: higher tumour control, improved radiobiological effects (tumour hypoxia), and hence better overall survival rates [3, 4, 5, 6, 7]. Further, lower values of lung dose metrics may reduce related lung toxicities such as pneumonitis and fibrosis [8, 9, 10]. With LED-SBRT, the balance between tumour dose elevation, tumour dose inhomogeneity, and lung sparing directly depends on the choice of beam parameters and patient conditions. Through manipulation of these parameters, physicists and dosimetrists can improve the tumour/lung dose distribution as desired. However, LED-SBRT treatment planning must also be in accordance with current SBRT protocols to ensure patient safety [11]. Future work will resolve remaining issues concerning tumour size and location, treatment delivery, and the controversial subject of tumour dose escalation versus dose homogeneity (see Section 1.2.3 below).

5.1.3 Cone-beam CT image-based lung dose calculations

In chapter 4 of the thesis, we assessed the suitability of using CBCT thorax images directly for adaptive dose computations. Currently, CBCT images of thorax patients are only being used for patient set-up. Ideally these images could also be used for ‘on the fly’ adaptive dose calculations to account for daily deformations in patient anatomy during the course of radiotherapy. Unfortunately, CBCT images of the thorax are subject to cupping and respiratory artefacts due to an increased CBCT scanning volume (producing an elevated scatter-to-primary x-ray ratio), and slow scan times (~ 1 min). The resultant CBCT number data (HU) are generally inaccurate, and will negatively

impact the accuracy of calculated SBRT tumour and lung dose distributions. Thus, the goal of this work was to determine the extent of CBCT number error in lung tissue, and its resultant effect on CBCT-derived lung density and computed dose accuracy. To this end, we compared planning CT (PCT) based dose calculations to CBCT-based results for three typical early-staged lung cancer patients. Comparison of CT number data within lung showed CBCT-derived lung density was severely undervalued, down to -1000 HU (or vacuum). Using the RDDF as a guide-line (from Chapter 2), we determined that erroneously low CBCT-derived lung density artificially disrupts CPE. As a result, CBCT image-based dose calculations underestimated the tumour prescription dose by as much as 13% compared to PCT based results.

In an attempt to correct inaccurate CBCT-based dose results, we proposed three CT number corrective techniques: 1) conversion of CBCT numbers to accurate tissue electron density using a ‘thorax sized’ calibration phantom, 2) ad-hoc replacement of CBCT pixels with four ‘bulk’ CT numbers (representing muscle, adipose, bone, and lung) derived from PCT images, and 3) selective replacement of CBCT lung pixels that were the most likely to cause artificial LED in dose calculations. Unfortunately, an accurate HU-to-relative electron density (HU-to-RED) conversion curve could not be obtained from CBCT scans of the phantom; CBCT number error in patient data was worse than in static phantom images. It was hypothesized that CBCT artefacts due to respiratory motion were poorly accounted for by scanning a static phantom, and resultant dose calculations could not reproduce the PCT based results. Bulk replacement of the heterogeneous lung tissue with a global average CT number also produced inaccurate dose results. By setting the entire CBCT lung to one average PCT number, real LED was not accounted for correctly in dose calculations, and resultant tumour dose was erroneously high up to 9% (relative to the prescription dose of 54 Gy). Selective replacement of CBCT lung pixels improved dose calculation accuracy considerably and represented a practical approach to localized density correction. However, it was concluded that a future study is required in order to further assess the accuracy and limitations of this technique in clinical practice (see Section 1.2.4).

5.1.4 Conclusions

The overall goal of this thesis was to determine the impact of lateral electron disequilibrium (LED) on stereotactic body radiation therapy of lung cancer. This goal motivated the following research questions:

- Q1** What combination of radiation field size, energy, and lung density, cause the LED phenomenon to occur?
- Q2** How sensitive is the dose distribution in LED regions to CT-derived lung density?
- Q3** How do we design a new SBRT technique that forces LED to occur in order to produce “spikes” of highly localized dose in small tumours, relative to surrounding lung?
- Q4** How does CBCT-derived lung density affect the lung and tumour dose distribution?
- Q5** Are lung CBCT numbers correctable for the purpose of accurate dose calculation?

Q1 and **Q2** were addressed within chapter 2 of the thesis. The incidence of the LED phenomenon is dependent on a combination of three “perfect storm” factors: beam energy, field size, and density. The phenomenon is most likely to occur when beam energy is high (> 10 MV), field size is small ($< 5 \times 5$ cm²), and density low (< 0.4 g/cm³). The combination of parameters that cause LED was quantified through the development of the relative depth dose factor [RDDF] (**Q1**). It was noted that the lung dose distribution experienced heightened sensitivity to lung density once LED was precipitated by regionally low density (**Q2**). Therefore, inaccurate CT-derived lung density, seen in CBCT scanning, can greatly affect dose calculation accuracy under these conditions. **Q3** was addressed within chapter 3 of the thesis. By choosing SBRT parameters that enhance LED, it was possible to create steep dose gradients at the lung/tumour interface. These parameters can be determined a priori using the RDDF and the radiation physics knowledge gained from Chapter 2. **Q4** and **Q5** were considered in chapter 4 of the thesis.

The combination of CBCT image artefacts (e.g. cupping, streaking and blurring) erroneously reduced CBCT-derived lung density, artificially creating LED, which inaccurately reduced the calculated tumour and lung dose distribution (**Q4**). Replacing artificially low CBCT lung pixels with a value that is more representative of true lung density (derived from the corresponding PCT image), improved dose calculation accuracy (**Q5**).

With regard to SBRT of lung cancer, the results of this thesis will provide physicians and physicists with: 1) knowledge concerning the RT parameters that can cause LED, 2) confidence in choice of LED-competent dose calculation algorithm, 3) means to avoid the potential negative dosimetric effects of LED, and 4) new techniques to gain dosimetric advantages for early-staged lung cancer patients. These contributions will help in the design of SBRT clinical trials so that lung cancer patients may experience improved SBRT treatment related outcomes (e.g. tumour control and overall survival with fewer severe complication rates).

5.2 Future Work

5.2.1 Generalize the relative depth dose factor (RDDF) to other forms of modern radiation therapy

In chapter two of the thesis, the RDDF was developed using single fields of radiation, and homogeneous phantoms. This approach was taken in order to simplify the interpretation of the radiation physics of CPE and LED for the SBRT technique. Advanced radiotherapy techniques, such as intensity-modulated radiation therapy (IMRT) and volume modulated arc therapy (VMAT), use multiple fields of radiation where heterogeneous photon fluence patterns are optimized according to treatment planning constraints. Further, patient lung tissue consists of heterogeneous density. The ability of the RDDF (or a similar metric) to predict the prevalence of LED under these instances needs to be assessed using a reliable Monte Carlo modeled VMAT/IMRT dose distribution [12]. Such an “LED alarm” tool would alert treatment planners to either avoid or exploit LED during IMRT or VMAT.

5.2.2 SBRT for lung cancer patients with emphysema

Within chapter 2 of the thesis, it was noted that LED was unavoidable (across all beam energies, and field sizes) for lung densities below 0.1 g/cm^3 . This result is relevant for conditions involving SBRT treatment of lung cancer patients who are also afflicted by emphysema. Emphysematous lung tissue contains air pockets with densities as low as 0.001 g/cm^3 [13]. When tumours are located adjacent to these regions, required SBRT protocols are much more challenging to fulfill [1]. A future study focused on the effects of emphysematous lung on SBRT dose distributions would be useful. These patients may preferentially benefit from LED-optimized SBRT (discussed in Chapter 3), where LED could be used to increase tumour dose levels.

5.2.3 LED-optimized SBRT: clinical implementation

In Chapter 3 of the thesis, we proposed a novel SBRT technique designed to cause LED for advantage. In our approach, we used a simplified arc technique involving 36 equally weighted fields, collimated into rectangular or square field sizes. This was done in order to facilitate interpretation of the underlying physics. In reality, more complicated radiation treatment methods such as VMAT are more clinically relevant. The next step in the progression of LED-SBRT should involve a Monte Carlo modeled, LED-optimized, VMAT technique (i.e. LED-VMAT) [12]. With LED-VMAT, we will assess the efficacy of this method in a real patient population exposed to today's popular forms of arc therapy.

Future work should be organized into a three phase study. The first phase would be a retrospective study, where dose distributions derived from standard SBRT techniques could be compared against results using LED-VMAT (i.e. greater use of small field segments and isolated beamlets). The study should focus on patients with various tumour sizes (0.25 cm up to 5 cm in diameter) and locations (e.g. central vs. peripheral lung). Further, to assess the benefits of gated treatment, LED-VMAT dose distributions

should be calculated using 4D-CT data from different phases of the respiratory cycle (e.g. inspiration vs. expiration). Using gated beams at inspiration phases of respiration would create new opportunities for forcing LED. From this analysis, we could determine the limitations of LED-VMAT, and identify a sub-set of patients that could most likely benefit from this technique.

The second phase of the study should resolve questions concerning practical treatment planning and delivery. The ability of various algorithms (e.g. collapsed-cone convolution) to accurately calculate dose distributions under conditions of extreme LED will be assessed against Monte Carlo results using LED-VMAT. As noted above, in Chapter 3 we hypothesized that dosimetric effects of LED-VMAT could be further accentuated if treatment were delivered during the inhale phase of the respiratory cycle (i.e. gating radiation treatment). Unfortunately, gating LED-VMAT will result in longer treatment session times; an issue that could be overcome using a Truebeam LINAC, where dose rates are up to 4 times higher compared to traditional LINAC technology[14]. In addition, the inhale phase of the breathing cycle is less stable in comparison to the exhale conditions more often used.

In the final phase, patients would be enrolled into a longitudinal pilot clinical study to test the ability of LED-VMAT to improve outcomes for early-staged lung cancer patients. LED-VMAT can produce very steep dose gradients to enhance tumour dose levels, while maintaining and/or reducing normal lung dose. This may be perceived as controversial by the community, as some authors may prefer the use of lower, more homogeneous dose distributions instead [15]. We could resolve this controversy by tracking improvements in tumour control, and overall patient survival for homogeneous versus inhomogeneous tumour dose patterns. Further, we will also assess the ability of LED-VMAT to avoid healthy structures, typically subject to high grade toxicities from standard SBRT treatment (e.g. ribs, esophagus, trachea, and bronchi).

5.2.4 Cone-beam CT image-guided Adaptive SBRT

In the fourth chapter of thesis, we proposed CT number corrective techniques to improve the accuracy of CBCT numbers by selective substitution. We recommended the use of a LED-sensitive CT number (LCT) substitute to replace CBCT lung pixels that artificially create LED. In this analysis, we tested the LCT method to correct CBCT images of only three patients, and found that dose calculations became comparable to PCT based results. Further, we suggested an expedited five step process to implement the correction technique clinically, to allow for ‘on the fly’ adaptive dose calculations. However, the accuracy and limitations of the LCT correction method should be tested in a larger population of patients with various tumour sizes and locations. Further, the efficiency of the envisioned five step process could be tested in a time-tracking study.

An alternative solution to this problem could be to scan a tissue equivalent, deformable lung calibration phantom [16] using CBCT thorax scan settings. With such a dynamic phantom, CBCT image artefacts observed in phantom scans may become more comparable to those seen in patient images, and a more accurate HU-to-RED curve may be obtained. 4D-CT imaging could also be used to determine dynamic changes in density as a function of time during gated or un-gated beam delivery.

5.2.5 Assessing the prevalence of LED susceptibility in a population of lung cancer patients treated by SBRT

Throughout the chapters of this thesis we have emphasized that LED can potentially reduce or enhance the dose within tumour tissues for SBRT treatment of early-staged lung cancer. Further, as this phenomenon may be poorly accounted for by clinical dose calculation algorithms, treatment prescriptions and clinical trials outcomes could be misleading or ambiguous. To further assess the validity of this statement, we must first determine the prevalence of LED for a group of SBRT lung patients. This could be done by retrospectively analyzing CT data from previously irradiated lung patients. In this analysis, patient lung density will be acquired from 4D-CT data. Using the physics knowledge learned from chapter 2, we will determine the specific lung densities that

create LED for commonly used SBRT beam parameters [e.g. 6 MV ($3 \times 3 \text{ cm}^2$)]. From this investigation, we will be able to approximate the number of SBRT lung cancer patients who are likely to be affected by LED considerations.

Future patients can be triaged for improved treatment planning that accounts for regional dose reductions due to LED. The ultimate goal remains to deliver tumour-controlling doses with minimal side effects for patients otherwise facing invasive surgery and a very poor prognosis. It is hoped that the publications from this thesis will raise community awareness to a new positive facet of LED - offering a new degree of freedom that might yield a better chance at a cure while maintaining good quality of life for lung cancer patients.

5.3 References

- [1] W. Yang, M. Lobo, N. Dunlap, P. Read, S. Benedict, K. Sheng and J. Lerner, "SU-E-T-790: The Effect of Pulmonary Emphysema on Lung SBRT Dosimetry," vol. 38, no. 6, pp. 3673-3673, 2011.
- [2] J. H. Siewerdsen and D. A. Jaffray, "Cone-beam computed tomography with a flat-panel imager: magnitude and effects of x-ray scatter.," *Med Phys*, vol. 28, no. 2, pp. 220-231, Feb 2001.
- [3] X. Qiao, O. Tullgren, I. Lax, F. Sirzén and R. Lewensohn, "The role of radiotherapy in treatment of stage I non-small cell lung cancer.," *Lung Cancer*, vol. 41, no. 1, pp. 1-11, Jul 2003.
- [4] N. Ohri, M. Werner-Wasik, I. Grills, J. Belderbos, A. Hope, D. Yan, L. Kestin, M. Guckenberger, J. Sonke, J. Bissonnette and others, "Modeling Local Control After Hypofractionated Stereotactic Body Radiation Therapy for Stage I Non-Small Cell Lung Cancer: A Report From the Elekta Collaborative Lung Research Group," *International Journal of Radiation Oncology* Biology* Physics*, vol. 84, no. 3, pp.

e379--e384, 2012.

- [5] R. Onimaru, M. Fujino, K. Yamazaki, Y. Onodera, H. Taguchi, N. Katoh, F. Hommura, S. Oizumi, M. Nishimura and H. Shirato, "Steep dose-response relationship for stage I non-small-cell lung cancer using hypofractionated high-dose irradiation by real-time tumor-tracking radiotherapy.," *Int J Radiat Oncol Biol Phys*, vol. 70, no. 2, pp. 374-381, Feb 2008.
- [6] H. Onishi, T. Araki, H. Shirato, Y. Nagata, M. Hiraoka, K. Gomi, T. Yamashita, Y. Niibe, K. Karasawa, K. Hayakawa, Y. Takai, T. Kimura, Y. Hirokawa, A. Takeda, A. Ouchi, M. Hareyama, M. Kokubo, R. Hara, J. Itami and K. Yamada, "Stereotactic hypofractionated high-dose irradiation for stage I nonsmall cell lung carcinoma: clinical outcomes in 245 subjects in a Japanese multiinstitutional study.," *Cancer*, vol. 101, no. 7, pp. 1623-1631, Oct 2004.
- [7] P. C. Cheung, W. J. Mackillop, P. Dixon, M. D. Brundage, Y. M. Youssef and S. Zhou, "Involved-field radiotherapy alone for early-stage non-small-cell lung cancer.," *Int J Radiat Oncol Biol Phys*, vol. 48, no. 3, pp. 703-710, Oct 2000.
- [8] U. Ricardi, A. R. Filippi, A. Guarneri, F. R. Giglioli, C. Mantovani, C. Fiandra, S. Anglesio and R. Ragona, "Dosimetric predictors of radiation-induced lung injury in stereotactic body radiation therapy.," *Acta Oncol*, vol. 48, no. 4, pp. 571-577, 2009.
- [9] R. Baker, G. Han, S. Sarangkasiri, M. DeMarco, C. Turke, C. Stevens and T. Dilling, "Clinical and Dosimetric Predictors of Radiation Pneumonitis in a Large Series of Patients Treated With Stereotactic Body Radiation Therapy to the Lung," *International Journal of Radiation Oncology* Biology* Physics*, 2012.
- [10] R. B. Barriger, J. A. Forquer, J. G. Brabham, D. L. Andolino, R. H. Shapiro, M. A. Henderson, P. A. S. Johnstone and A. J. Fakiris, "A dose-volume analysis of radiation pneumonitis in non-small cell lung cancer patients treated with stereotactic body radiation therapy.," *Int J Radiat Oncol Biol Phys*, vol. 82, no. 1, pp. 457-462,

Jan 2012.

- [11] C. W. Hurkmans, J. P. Cuijpers, F. J. Lagerwaard, J. Widder, U. A. van der Heide, D. Schuring and S. Senan, "Recommendations for implementing stereotactic radiotherapy in peripheral stage IA non-small cell lung cancer: report from the Quality Assurance Working Party of the randomised phase III ROSEL study.," *Radiat Oncol*, vol. 4, p. 1, 2009.
- [12] J. Lobo and I. Popescu, "Two new DOSXYZnrc sources for 4D Monte Carlo simulations of continuously variable beam configurations, with applications to RapidArc, VMAT, TomoTherapy and CyberKnife," *Physics in medicine and biology*, vol. 55, no. 16, p. 4431, 2010.
- [13] G. R. Washko, G. M. Hunninghake, I. E. Fernandez, M. Nishino, Y. Okajima, T. Yamashiro, J. C. Ross, R. S. JosĂ©, D. A. Lynch, J. M. Brehm, K. P. Andriole, A. A. Diaz, R. Khorasani, K. D'Aco, F. C. Sciurba, E. K. Silverman, H. Hatabu and I. O. Rosas, "Lung Volumes and Emphysema in Smokers with Interstitial Lung Abnormalities," *New England Journal of Medicine*, vol. 364, no. 10, pp. 897-906, 2011.
- [14] J. Hrbacek, S. Lang and S. Klock, "Commissioning of photon beams of a flattening filter-free linear accelerator and the accuracy of beam modeling using an anisotropic analytical algorithm," *International Journal of Radiation Oncology* Biology* Physics*, vol. 80, no. 4, pp. 1228-1237, 2011.
- [15] A. van Baardwijk, W. A. Tom , W. van Elmpt, S. M. Bentzen, B. Reymen, R. Wanders, R. Houben, M. Ollers, P. Lambin and D. De Ruyscher, "Is high-dose stereotactic body radiotherapy (SBRT) for stage I non-small cell lung cancer (NSCLC) overkill? A systematic review.," *Radiother Oncol*, vol. 105, no. 2, pp. 145-149, Nov 2012.
- [16] M. Serban, E. Heath, G. Stroian, D. L. Collins and J. Seuntjens, "A deformable

phantom for 4D radiotherapy verification: Design and image registration evaluation," *Medical Physics*, vol. 35, no. 3, pp. 1094-1102, 2008.

Appendices

Appendix A: Transfer of Copy write from Physics in Medicine and Biology

7/18/13 Re: Permission to include article in PhD thesis....

From: "Brandon Disher" [REDACTED]
 To: <permissions@iop.org>,
 Date: 08/06/2013 18:08
 Subject: Permission to include article in PhD thesis....

Good Afternoon,

I am currently writing my thesis in order to complete a component of my PhD degree with the Department of Medical Biophysics, Western University, London Ontario, Canada. Recently we published an article entitled "Correction for 'artificial' electron disequilibrium due to cone-beam CT density errors: implications for on-line adaptive stereotactic body radiation therapy of lung" in the Physic in Medicine and Biology journal (<http://www.ncbi.nlm.nih.gov/pubmed/23689060>). I would like to include this article in my thesis. Could you please grant me permission to do so?

Kind regards,
 Brandon Disher

7/18/13 Re: Permission to include article in PhD thesis....

Re: Permission to include article in PhD thesis....

From: Permissions <permissions@iop.org>
 To: [REDACTED]
 Date: Monday - June 10, 2013 3:12 AM
 Subject: Re: Permission to include article in PhD thesis....
 Attachments: TEXT.htm; Mime.822

Dear Brandon Disher,

Thank you for your request to reproduce IOP Publishing material.

We are happy to grant permission for the use you request on the terms set out below.

If you have any questions, please feel free to contact our Permissions team at permissions@iop.org.

I should be grateful if you would acknowledge receipt of this email.

Kind regards,

Sarah Ryder

Publishing Administrator
 Email: permissions@iop.org

Conditions

Non-exclusive, non-transferrable, revocable, worldwide, permission to use the material in print and electronic form will be granted **subject to the following conditions:**

- Permission will be cancelled without notice if you fail to fulfil any of the conditions of this letter.
- You will make reasonable efforts to contact the author(s) to seek consent for your intended use. Contacting one author acting expressly as authorised agent for their co-authors is acceptable.
- You will reproduce the following prominently alongside the material:
 - o the source of the material, including author, article title, title of journal, volume number, issue number (if relevant), page range (or first page if this is the only information available) and date of first publication
 - o for material being published electronically, a link back to the article (via DOI)
 - o if practical and IN ALL CASES for works published under any of the Creative Commons licences the words "© Institute of Physics and Engineering in Medicine. Published on behalf of IPEM by IOP Publishing Ltd. All rights reserved."
- The material will not, without the express permission of the author(s), be used in any way which, in the opinion of IOP Publishing, could distort or alter the author(s)' original intention(s) and meaning, be prejudicial to the honour or reputation of the author(s) and/or imply endorsement by the author(s) and/or IOP Publishing.
- Payment of £0 is received in full by IOP Publishing prior to use.

Please note: IOP does not usually provide signed permission forms as a separate attachment. Please print this email and provide it to your publisher as proof of permission.

From: "Brandon Disher" <[REDACTED]>
 To: <permissions@iop.org>,
 Date: 15/04/2013 20:03

7/18/13 Re: Permission to include article in PhD thesis....
 Subject: Permission to include article in PhD thesis....

Good Afternoon,

I am currently writing my thesis in order to complete a component of my PhD degree with the Department of Medical Biophysics, Western University, London Ontario, Canada. Recently we published an article entitled "An in-depth Monte Carlo study of lateral electron disequilibrium for small fields in ultra-low density lung: implication for modern radiation therapy" in the *Physic in Medicine and Biology* journal (<http://www.ncbi.nlm.nih.gov/pubmed/22391122>). I would like to include this article in my thesis. Could you please grant me permission to do so?

Kind regards,
 Brandon Disher

7/18/13 Re: Permission to include article in PhD thesis....

Re: Permission to include article in PhD thesis....

From: Permissions <permissions@iop.org>
To: [REDACTED]
Date: Tuesday - April 16, 2013 3:59 AM
Subject: Re: Permission to include article in PhD thesis....
Attachments: TEXT.htm; Mime.822

Dear Brandon Disher,

Thank you for your request to reproduce IOP Publishing material.

We are happy to grant permission for the use you request on the terms set out below.

If you have any questions, please feel free to contact our Permissions team at permissions@iop.org.

I should be grateful if you would acknowledge receipt of this email.

Kind regards,

Sarah Ryder

Publishing Administrator
 Email: permissions@iop.org

Conditions

Non-exclusive, non-transferrable, revocable, worldwide, permission to use the material in print and electronic form will be granted **subject to the following conditions:**

- Permission will be cancelled without notice if you fail to fulfil any of the conditions of this letter.
- You will make reasonable efforts to contact the author(s) to seek consent for your intended use. Contacting one author acting expressly as authorised agent for their co-authors is acceptable.
- You will reproduce the following prominently alongside the material:
 - o the source of the material, including author, article title, title of journal, volume number, issue number (if relevant), page range (or first page if this is the only information available) and date of first publication
 - o for material being published electronically, a link back to the article (via DOI)
 - o if practical and IN ALL CASES for works published under any of the Creative Commons licences the words "© Institute of Physics and Engineering in Medicine. Published on behalf of IPEM by IOP Publishing Ltd. Reproduced by permission of IOP Publishing. All rights reserved"
- The material will not, without the express permission of the author(s), be used in any way which, in the opinion of IOP Publishing, could distort or alter the author(s)' original intention(s) and meaning, be prejudicial to the honour or reputation of the author(s) and/or imply endorsement by the author(s) and/or IOP Publishing.
- Payment of £0 is received in full by IOP Publishing prior to use.

Curriculum Vitae

Name: Brandon Disher

Post-secondary Education and Degrees: University of Windsor
Windsor, Ontario, Canada
2002-2007 B.Sc. in Physics and High Technology (Co-op)

The University of Western Ontario
London, Ontario, Canada
2007-2013 Ph.D.

Honours and Awards: National Sciences and Engineering Research Council of Canada (NSERC), PGS-D award
2008 - 2012

Canadian Institute of Health Research
Student Training Program (CIHR-STP) PhD Award
2008 – 2012

Canadian Organization of Medical Physicists (COMP)
Young Investigator Symposium (YIS) competitor
2012

Medicalphysicsweb, feature publication:
<http://medicalphysicsweb.org/cws/article/research/48922>
March 2012

Western University, Schulich's School of Medicine and Dentistry's Publication of the Month
June 2012

First place poster presentation, CIHR - The Oncology Research & Education Day
2012

Second place poster presentation, Imaging Network Ontario, Annual Scientific Meeting
2012

First place poster presentation, CIHR - The Oncology Research & Education Day
2011

Related Work Experience

Research Assistant
Tri-University Meson Facility (TRIUMF), Vancouver, BC
2005

Research Assistant
Atomic and Molecular Physics, Queens University of Belfast,
Belfast Northern Ireland, United Kingdom
2005

Research Assistant
Atomic Physics, University of Windsor, Windsor, ON
2004

Research Assistant
CIRMC, University of Windsor, Windsor, ON
2003

**Publications:
Papers**

Brandon Disher, George Hajdok, Stewart Gaede, and Jerry J. Battista “An in-depth Monte Carlo study of lateral electron disequilibrium for small fields in ultra-low density lung: implications for modern radiation therapy” *Physics in Medicine and Biology*. 2012 Mar 21;57(6):1543-59.

Brandon Disher, George Hajdok, An Wang, Jeff Craig, Stewart Gaede, and Jerry J. Battista “Correction for “artificial” electron disequilibrium due to cone-beam CT density errors: implications for on-line adaptive stereotactic body radiation therapy of lung”, *Physics in Medicine and Biology*. 2013 May 20;58(12):4157-4174.

Brandon Disher, George Hajdok, Stewart Gaede, and Jerry J. Battista “Forcing lateral electron disequilibrium to spare healthy lung tissue: A novel technique for SBRT of small lung tumours”, accepted pending revisions by *Physics in Medicine and Biology* (April, 6, 2013).

Brandon Disher, Laura Wade, George Hajdok, Stewart Gaede, David Palma, and Jerry J. Battista “Assessing the prevalence of lateral electron disequilibrium for a population of lung cancer patients receiving stereotactic body radiation therapy”, in preparation for the *International Journal of Radiation Oncology Biology Physics* (submission date ~ September 2013).

An Wang, Brandon Disher, Greg Carnes, Terry M. Peters “Rapid block matching based nonlinear registration on GPU for image guided radiation therapy” *Proceedings of SPIE*. 2010 7625, 762511.